

# **Optical AC coupling in the gravitational wave detection band**

Von der Fakultät für Mathematik und Physik  
der Gottfried Wilhelm Leibniz Universität Hannover  
zur Erlangung des Grades

**Doktor der Naturwissenschaften  
Dr. rer. nat.**

genehmigte Dissertation  
von

**M.Sc. Phys. Steffen Kaufer**

geboren am 25. Juli 1986 in Lehrte

2018

Referent: apl. Prof. Dr. Benno Willke  
Korreferent: Prof. Dr. Karsten Danzmann  
Tag der Promotion: 29. März 2018





## Abstract

Active laser power stabilization is essential to meet the high laser power stability demands of second generation gravitational wave detectors. To achieve a sufficient shot noise limited performance high optical power needs to be detected in traditional stabilization schemes. This leads to technical complications, for example, those caused by the thermal loads induced in the sensors. Therefore, novel detection schemes for laser power noise become desirable.

One of these is Optical AC coupling, which reduces the amount of optical power that needs to be detected in order to reach a certain shot noise limited sensitivity by placing the photodetector in reflection of an optical resonator. To investigate the potential for implementing Optical AC coupling in gravitational wave detectors, different experiments were performed in the 0.3 Hz to 60 kHz frequency range, thereby covering the gravitational wave detection band.

A dedicated laboratory experiment was designed and set up, allowing for an Optical AC coupling based power stabilization at previously unattained sensitivity. At the core of this experiment is a 1 m long, high Finesse optical resonator with a corner frequency of 2 kHz. Detailed noise investigations including effects due to non perfect mode matching were crucial in obtaining the final performance.

Furthermore, the potential to increase the power stability of light injected into full scale gravitational wave detectors via Optical AC coupling was explored. For the first time, measurements of the so called Optical AC coupling transfer function of the coupled cavities, formed by the power recycling mirror and the main interferometer, of the Advanced LIGO Livingston and the GEO 600 detectors are presented. Experiments towards an implementation of the Optical AC coupling technique into the power stabilization feedback control scheme of GEO 600 provided valuable insight into the specific challenges that arise with such an implementation at gravitational wave detectors.

**Keywords:** active laser power stabilization, shot noise, Optical AC coupling, gravitational waves



## Kurzfassung

Aktive Laserleistungsstabilisierung ist unerlässlich, um die hohen Anforderungen an die Leistungsstabilität der zweiten Generation von Gravitationswellendetektoren zu erfüllen. In traditionellen Stabilisierungsmethoden müssen hohe optische Leistungen detektiert werden, um eine ausreichende Schrotrausch begrenzte Leistungsstabilität zu erreichen. Dies führt zu technischen Komplikationen, verursacht z.B. durch die thermische Leistung, die in den Sensor eingebracht wird. Dadurch werden neue Verfahren zur Laserleistungsstabilisierung zunehmend interessanter.

Eines dieser neuen Verfahren ist das sogenannte Optical AC coupling. Bei diesem Verfahren wird die optische Leistung, die detektiert werden muss, um eine bestimmte Schrotrausch begrenzte Sensitivität zu erreichen, reduziert, indem der Photodetektor in Reflektion eines optischen Resonators platziert wird. Um die Möglichkeit zu untersuchen, Optical AC coupling in einem Gravitationswellendetektor zu implementieren, wurden unterschiedliche Experimente in einem Frequenzbereich zwischen 0.3 Hz und 60 kHz durchgeführt und damit das Gravitationswellendetektionsband abgedeckt.

Ein spezielles Laborexperiment wurde geplant und installiert. Eine Optical AC coupling basierte Leistungsstabilisierung mit bisher unerreichter Sensitivität wurde erzielt. Das Herzstück des Experiments ist ein 1 m langer optischer Resonator mit einer hohen Finesse und einer Eckfrequenz von 2 kHz. Detaillierte Rauschuntersuchungen waren essenziell, um die finale Sensitivität des Experimentes zu erreichen. Vor allem Effekte, verursacht durch nicht perfekte Modenanpassung, mussten dabei berücksichtigt werden.

Außerdem wurde die Möglichkeit untersucht, Optical AC coupling einzusetzen, um die Leistungsstabilität des Lichtes, welches in einem Gravitationswellendetektor eingekoppelt wird, zu verbessern. Erstmals wurde die sogenannte Optical AC coupling Transfer Funktion des gekoppelten Resonators, bestehend aus dem sogenannten Power Recycling Spiegel und dem Hauptinterferometer, für den Advanced LIGO Livingston Detektor und GEO 600 vermessen. Weitere Experimente auf dem Weg zu einer möglichen Integration von Optical AC coupling in die Leistungsstabilisierung von GEO 600 wurden durchgeführt und lieferten wertvolle Informationen über die möglichen Hindernisse, welche bei einer solchen Implementierung auftreten können.

**Schlagworte:** Laserleistungsstabilisierung, Schrotrauschen, Optical AC coupling, Gravitationswellen



# Contents

<b>Contents</b>	<b>IX</b>
<b>List of Figures</b>	<b>XIII</b>
<b>List of Tables</b>	<b>XV</b>
<b>List of Abbreviations</b>	<b>XVII</b>
<b>1 Introduction</b>	<b>1</b>
<b>2 Laser power stabilization</b>	<b>5</b>
2.1 Transfer functions and power spectral densities . . . . .	6
2.2 Laser beams and laser power noise . . . . .	7
2.3 Phasor representation and sideband picture . . . . .	8
2.3.1 Amplitude modulation and noise in the sideband picture . . . . .	9
2.4 Noise sources . . . . .	11
2.4.1 Shot noise . . . . .	11
2.4.2 Technical power noise . . . . .	12
2.5 Passive laser power stabilization . . . . .	13
2.5.1 Optical Resonators . . . . .	14
2.5.2 Frequency stabilization . . . . .	17
2.5.3 Filter properties of the optical resonator . . . . .	18
2.5.4 Impedance matching . . . . .	19
2.5.5 Mode matching . . . . .	20
2.6 Active laser power stabilization . . . . .	21
2.6.1 In-loop and out-of-loop measurements . . . . .	21
2.7 State of the art laser power stabilization . . . . .	24
<b>3 Optical AC coupling</b>	<b>27</b>
3.1 OAC Transfer function . . . . .	30
3.2 Imperfect mode matching . . . . .	32
3.3 OAC gain optimization . . . . .	35
3.4 Estimation of $a$ and $p$ from DC reduction and OAC gain	38

## CONTENTS

3.5	Noise couplings . . . . .	39
3.5.1	Frequency noise . . . . .	39
3.5.2	Mode fluctuations . . . . .	43
3.5.3	Resonator internal scattering . . . . .	44
3.6	Summary . . . . .	45
<b>4</b>	<b>OAC with a narrow linewidth resonator</b>	<b>47</b>
4.1	Resonator Design . . . . .	47
4.1.1	Linewidth and impedance matching . . . . .	50
4.1.2	Higher order mode suppression . . . . .	51
4.2	Experimental Setup . . . . .	54
4.2.1	Frequency stabilization . . . . .	59
4.2.2	Power stabilization . . . . .	60
4.3	Experimental challenges . . . . .	62
4.3.1	Residual amplitude modulation . . . . .	62
4.3.2	Alignment and mode matching . . . . .	64
4.4	Results . . . . .	66
4.4.1	Transfer function measurements . . . . .	66
4.4.2	Polarization effects . . . . .	68
4.4.3	Power stabilization experiment at atmospheric pressure and 0.3 mA photocurrent . . . . .	69
4.4.4	Power stabilization experiment below 10 mBar and 0.3 mA photocurrent . . . . .	72
4.4.5	Power stabilization experiment below 10 mBar and 1 mA photocurrent . . . . .	77
4.5	Discussion . . . . .	77
4.6	Chapter Outlook . . . . .	79
<b>5</b>	<b>Optical AC coupling for gravitational wave detectors</b>	<b>83</b>
5.1	Investigations of OAC at aLIGO . . . . .	84
5.1.1	Optical Layout of aLIGO . . . . .	84
5.1.2	Transfer function measurement . . . . .	86
5.1.3	Results and Simulation . . . . .	89
5.1.4	Discussion . . . . .	90
5.2	Investigations of OAC at GEO 600 . . . . .	92
5.2.1	Optical Layout of GEO 600 . . . . .	92
5.2.2	Frequency stabilization . . . . .	95
5.2.3	Transfer function measurement and calibration . . . . .	96
5.2.4	Towards an implementation into power stabilization feedback control scheme . . . . .	103
5.2.5	Discussion . . . . .	107

*CONTENTS*

5.3 Chapter Summary . . . . .	108
<b>6 Summary</b>	<b>109</b>
<b>Bibliography</b>	<b>111</b>
<b>Acknowledgements</b>	<b>123</b>
<b>Curriculum Vitae</b>	<b>125</b>



## List of Figures

2.1	Impulse response function and transfer function of a linear system . . . . .	7
2.2	Phasor representation of an electric field in fixed and rotating frame . . . . .	9
2.3	Amplitude Modulation and amplitude noise in the side-band picture . . . . .	10
2.4	Passive filtering of power modulations in time domain and frequency domain . . . . .	14
2.5	Linear optical resonator . . . . .	15
2.6	Transmitted Power through an optical Resonator . . . . .	17
2.7	Filter function of an optical resonator . . . . .	18
2.8	Active amplitude stabilization scheme . . . . .	21
2.9	Fundamental shot noise limit of a traditional active laser power stabilization feedback . . . . .	23
3.1	Optical AC Coupling illustration . . . . .	28
3.2	OAC transfer function . . . . .	33
3.3	Maximum OAC gain for varying impedance matching and mode matching . . . . .	35
3.4	Field contributions in reflection of the OAC resonator for imperfect mode matching . . . . .	37
3.5	Implementation of an Optical AC coupling detector into an active power stabilization scheme . . . . .	40
3.6	Out of loop frequency noise conversion for different parameters . . . . .	43
4.1	OAC resonator spacer assembly . . . . .	49
4.2	Motorized Iris Aperture and OAC resonator clamped into its mount . . . . .	49
4.3	Power transmission through a circular aperture for different Hermite Gaussian modes . . . . .	52
4.4	Photograph of the spare GEO 600 tank . . . . .	54
4.5	Experimental layout . . . . .	55

## LIST OF FIGURES

4.6	Photograph of the remote controlled alignment mirrors	56
4.7	Photograph of the experimental setup inside the vacuum tank . . . . .	57
4.8	Power stabilization feedback control loop Open loop gain	61
4.9	Temperature stabilized EOM . . . . .	62
4.10	Temperatures stability of the self build EOM . . . . .	63
4.11	OAC transfer function for impedance matchings . . . . .	67
4.12	OAC transfer function for different orientations of linear input polarization . . . . .	69
4.13	Performance of the 2 kHz Optical AC coupling power stabilization experiment at atmospheric pressure . . . . .	71
4.14	Performance of the 2 kHz Optical AC coupling power stabilization experiment below 10 mBar . . . . .	73
4.15	Noise investigation for the 2 kHz Optical AC coupling power stabilization experiment below 10 mBar . . . . .	76
4.16	Noise investigation for the 2 kHz Optical AC coupling power stabilization experiment below 10 mBar and 1 mA photocurrent . . . . .	78
4.17	Comparison of the new experiment to previous results	80
5.1	Reduced optical Layout of the aLIGO Livingston detector	85
5.2	Calibration . . . . .	87
5.3	aLIGO Optical AC Coupling transfer function measurement . . . . .	89
5.4	Optical Layout of GEO 600 . . . . .	93
5.5	Measurement of the coupled cavity corner frequency . . . . .	98
5.6	OAC transfer functions measured at GEO 600 for different input power level . . . . .	99
5.7	Estimated impedance matching and Optical AC coupling gain on gain curves for different mode matchings coefficients $p$ . . . . .	101
5.8	Excess relative power noise measured in reflection of the locked GEO 600 detector for different PRC-gain settings	104
5.9	Excess relative power noise measured in reflection of the locked GEO 600 detector for different MC1 gains . . . . .	106

## List of Tables

4.1	Calculated Finesse and corner frequency $f_0$ of the resonator for different resonator internal losses. . . . .	50
4.2	Frequency separation of higher order HG modes with respect to the fundamental mode . . . . .	51
5.1	Parameters . . . . .	91
5.2	Optical AC coupling parameter Estimation for GEO 600	101
5.3	Errors for mode matching estimates . . . . .	103
5.4	Errors for impedance matching estimates . . . . .	103





## List of Abbreviations

AC	alternating current
aLIGO	Advanced Laser Interferometer Gravitational-Wave Observatory
AOM	acousto optical modulator
CCD	charge-coupled device
CE	Cosmic Explorer
DC	direct current
EOAM	electro optical amplitude modulator
EOM	electro optical modulator
ET	Einstein Telescope
FI	Faraday Isolator
HG	Hermite Gauss
IL	in-loop
IMC	input mode cleaner
in	incoming
LW	linewidth
NPRO	Non-planar Ring Oscillator
OAC	Optical AC Coupling
OLG	open loop gain
OOL	out-of-loop
PBS	polarizing beam splitter

## *LIST OF TABLES*

PDH	Pound-Drever-Hall
PM	polarization maintaining
PMC	pre mode cleaner
PZT	Piezo electric transducer
RAM	residual amplitude modulation
refl	reflected
RF	radio frequency
RPN	relative power noise
TEM	transverse electromagnetic
TF	transfer function
trans	transmitted
TTFSS	Table Top Frequency Stabilization Servo

# 1

## Chapter 1

### Introduction

Continuous wave lasers with highly stable frequency and optical power are fundamental tools in metrology and experimental physics. The spectrum of applications with high demands on laser power stability ranges from atomic clocks utilizing optically trapped atoms [1, 2] over the generation of frequency combs [3, 4] to zepto-newton force sensing experiments with optically trapped nanospheres [5], absorption spectroscopy (Gas Detection) [6] and opto-mechanical experiments [7].

One of the most demanding experiments with respect to laser power stability is the detection of gravitational waves, which are disturbances in space-time produced by extremely violent cosmological phenomena such as supernovae, colliding neutron stars and merger of two black holes [8]. Traveling at the speed of light, gravitational waves stretch and compress the fabric of space-time perpendicular to their direction of propagation.

In 2015, almost exactly 100 years after their prediction through Einstein, gravitational waves created by a binary black hole merger, were detected for the first time in history [9]. Due to this major breakthrough the Nobel Prize in physics was awarded to Rainer Weiss, Kip S. Thorne and Barry C. Barish in 2017.

Modern gravitational wave detectors like Advanced LIGO (aLIGO) [10, 11], Advanced Virgo [12, 13] or GEO 600 [14, 15], are designed as Michelson-Interferometers with arm lengths up to 4 km. A gravitational wave passing through the detector induces a differential arm length change between the interferometer arms and is therefore transformed into a laser power change at the readout port of the detector. Laser power noise can couple into the interferometer readout through various mechanisms and therefore strict requirements are imposed on

## 1 Introduction

---

the relative power stability of the light injected into the interferometer. For the aLIGO detectors these requirements are set to a relative power stability of  $2.0 \cdot 10^{-9} \text{ Hz}^{-1/2}$  at a frequency of 10 Hz, which is magnitudes beyond the stability provided by even the best available laser sources[16].

The only way to reach a sufficient noise suppression, especially at a frequency of 10 Hz, is by means of active power stabilization. A fundamental limitation with respect to the detection of power noise is set by shot noise, which is caused by the quantum nature of light [17] and corresponds to a minimal uncertainty in the power measurement of a coherent state. The relative size of the shot noise can be decreased by detecting more optical power, however, the amount of power that needs to be detected in order to reach the aLIGO requirements, can not be handled by a single photodiode. Hence, a dedicated photodiode-array was developed which allowed the optical power to be split onto four photodiodes thereby reducing thermal and technical complications [18].

Since relative shot noise decreases with the square root of the optical power, any future experiment with even stricter requirements will have to put a lot of effort into the design of a better sensor for laser power noise.

A possible way to avoid complicated detector cooling schemes or a further scaling in the number of photodiodes was introduced with the Optical AC coupling technique [19]. This novel approach exploits the carrier reduction in reflection of an optical resonator to achieve a reduced optical power on the detector without losing sensitivity to power fluctuations with optical frequencies outside of the resonator linewidth.

In using Optical AC coupling a former unattained detection sensitivity for relative laser power fluctuations of  $10^{-10} \text{ Hz}^{-1/2}$  was achieved for frequencies above 10 MHz [20]. This demonstrates the significant potential of this technique for further improvements in laser power stabilization. An implementation of Optical AC coupling into an active power stabilization feedback control scheme allowed for an improvement in relative power stability by a factor of 9, compared to a classical power stabilization detecting the same amount of optical power [21]. However, the maximum improvement could be achieved only at frequencies above 100 kHz. Various excess noise sources, which were introduced by the optical resonator were characterized and had to be minimized rigorously before the final performance of the experiment

---

could be achieved. The remaining excess noise for frequencies below 4 kHz was partly attributed to mechanical resonances of the setup and partly remained unexplained [22]. Therefore the suitability of the OAC technique for laser power stabilization at lower frequencies has to be tested, especially with respect to potential noise sources, which could not be identified in earlier experiments due to the described excess noise.

This thesis presents the investigation of the Optical AC coupling technique at frequencies between 0.3 Hz and 60 kHz, performed at large scale gravitational wave detectors and in a dedicated laboratory experiment. The experiments were performed at several locations; the Albert-Einstein-Institute in Hannover, the aLIGO Livingston detector in Louisiana and the GEO 600 detector near Hannover.

### Structure of the thesis

**Chapter 2** briefly reviews the analytic description of laser beams and laser power noise, before typical laser noise sources are discussed. The phasor picture and the sideband picture for laser power modulations are introduced, before active and passive power stabilization techniques are reviewed. Limitations of state of the art laser power stabilization are presented at the end of the chapter.

In **Chapter 3** the novel Optical AC coupling technique for laser power stabilization is introduced theoretically. The optimization of the Optical AC coupling gain for imperfectly mode matched resonators is analyzed, before the most important noise couplings attributed to the OAC technique are discussed.

Design, setup, characterization and final performance of a new OAC experiment, performed at the Albert Einstein Institute in Hannover, are presented in **Chapter 4**. The core component of this experiment is an OAC resonator with a narrow linewidth below  $\nu_{LW} = 4$  kHz and a tunable impedance matching.

**Chapter 5** presents the first Optical AC coupling transfer function measurements performed at the operational gravitational wave detectors aLIGO Livingston and GEO 600. The last part of the chapter discusses noise investigations towards the implementation of OAC into the power stabilization feedback control loop at GEO 600.

The final **Chapter 6** summarizes the work presented in this thesis.



# 2

## Chapter 2

# Laser power stabilization

This chapter is a short introduction into the formalism used throughout the scope of this thesis. After the definition of transfer functions and spectral densities (Section 2.1), laser beams and especially laser power noise are introduced in Section 2.2).

With the phasor representation and the sideband picture, a graphical representation for the laser noise and amplitude modulations is developed in Section 2.3. This picture will be used throughout this thesis, especially in Chapter 3, which is devoted to the Optical AC coupling theory.

Several important laser power noise sources are discussed in Section 2.4, which explains the two major categories of laser power noise; quantum shot noise and technical laser power noise.

The foundation established within the first Sections allows to understand passive laser power stabilization schemes introduced in Section 2.5. Passive power stabilization can be achieved with different optical components. However, a key topic for this thesis is the theory of optical resonators and their filtering effect, with respect to power fluctuations.

Active power stabilization schemes and their theoretical shot noise limited performance are discussed in Section 2.6. The limits of state of the art laser power stabilization are reviewed briefly in Section 2.7, in order to emphasize the demand for advanced techniques for laser power stabilization.

### 2.1 Transfer functions and power spectral densities

If a physical system is invariant in time and any linear combination of arbitrary input signals results in the same linear combination of their respective output signal, the system is referred to as an ideal linear time invariant (LTI) system. The dynamics of such a system can be described either by its impulse response function  $h(\tau)$  (time domain) or by its frequency response function  $H(f)$  (frequency domain), which is the Fourier Transform of  $h(\tau)$  (see Figure 2.1) [23, Chapter 2].

The output  $y(t)$ , which results from the input  $x(t)$  to the system, can therefore be calculated either in the time domain with the so called convolution integral or in the frequency domain via a simple multiplication with the frequency response function.

In this thesis, the frequency domain approach and the usage of frequency response functions, referred to as transfer functions from here on<sup>1</sup>, will be of major importance.

The transfer function of a system is defined as:

$$Y(f) = H(f)X(f) = |H(f)|e^{-i\Phi(f)}X(f), \quad (2.1)$$

where  $X(f)$  and  $Y(f)$  are the finite Fourier transforms of the time series  $x(t)$  and  $y(t)$ . The transfer function  $H(f)$  is a complex function that can be divided into its magnitude  $|H(f)|$  and phase factor  $\Phi(f)$ .

$$H(f) = |H(f)|e^{-i\Phi(f)} \quad (2.2)$$

If the input of a system with transfer function  $H(f)$ , is a sinusoidal modulation with a certain amplitude  $x(t) = A \cos(2\pi ft)$ , the output of the system will be a sinusoidal modulation at the same frequency, but with a modified amplitude and phase  $y(t) = |H(f)| A \cos(2\pi ft + \Phi(f))$ .

The power spectral density  $S_x(f)$  of a signal  $x(t)$  is defined as the Fourier transform of its autocorrelation function[23]. Since the power spectral density is a symmetric function with respect to frequencies, it is convenient to use the one sided power spectral density  $G_x(f) = 2S_x(f)$ , or a one sided linear spectral density  $\sqrt{G_x(f)}$ .

The previously defined transfer function  $H(f)$  can also be used to calculate the one sided power spectral density of the output signal

---

<sup>1</sup>Note that the frequency response function is a special case of the more profound transfer function definition, see [23, Chapter 2]



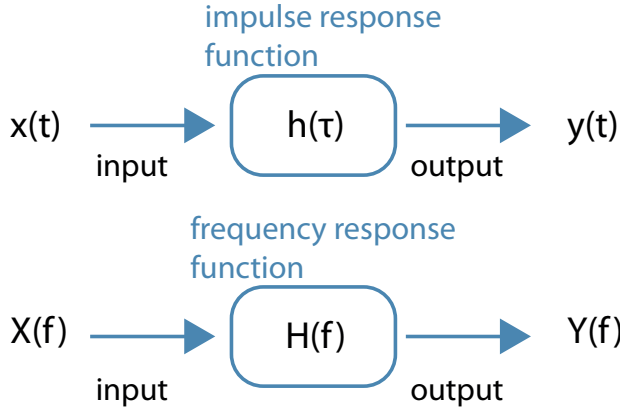


Figure 2.1: Impulse response function and transfer function of a linear system

$G_y(f)$  from the one sided power spectral density of the input signal  $G_x(f)$  according to [23, Chapter 6]:

$$G_y(f) = |H(f)|^2 G_x(f) \quad \text{in units of} \quad \left[ \frac{1}{\text{Hz}} \right] \quad (2.3)$$

And similarly the one sided linear spectral density of the output can be found as:

$$\sqrt{G_y(f)} = |H(f)| \sqrt{G_x(f)} \quad \text{in units of} \quad \left[ \frac{1}{\sqrt{\text{Hz}}} \right] \quad (2.4)$$

## 2.2 Laser beams and laser power noise

The complex field amplitude  $U(\vec{r}, t)$  of a laser beam can be described as

$$U(\vec{r}, t) = U_0(t) \cdot e^{2\pi i \nu(t)t} \cdot \sum_{l,m \geq 0} c_{lm} \Psi_{lm}(\vec{r}) \quad (2.5)$$

with the amplitude  $U_0(t)$  and the laser frequency  $\nu(t)$ . Frequency and wavelength are related by the speed of light  $c$ :  $\lambda(t) = c/\nu(t)$ .

The spatial beam profile is expressed by the sum  $\sum c_{lm} \Psi_{lm}(\vec{r})$ , with the complex amplitudes  $\Psi_{lm}(\vec{r})$  of the Hermite Gaussian modes  $HG_{lm}$  and their complex expansion coefficients  $c_{lm}$  [22, 24, 25].

The normalization of the coefficients  $c_{lm}$  and  $\Psi_{lm}$  is defined by:

$$\int dx dy |\Psi_{lm}(\vec{r})|^2 = 1 \quad \text{and} \quad \sum_{l,m \geq 0} |c_{lm}|^2 = 1 \quad (2.6)$$

## 2 Laser power stabilization

---

The absolute power  $P(t)$  is calculated from the complex field amplitude as:

$$P(t) = |\mathbf{U}(\vec{r}, t)|^2 \quad \text{in units of [W].} \quad (2.7)$$

For better comparability it is common to use the relative power noise (RPN), which is the absolute power noise  $\delta P$  normalized by the average optical power  $\bar{P}$  for a certain time span.

$$\text{RPN}(t) = \delta P(t)/\bar{P} = |\mathbf{U}(\vec{r}, t)|^2 / \overline{|\mathbf{U}(\vec{r}, t)|^2} \quad (2.8)$$

The average optical power for a certain time span  $T$  can be calculated with:

$$\bar{P} = \overline{|\mathbf{U}(\vec{r}, t)|^2} = \frac{1}{T} \int_T |\mathbf{U}(\vec{r}, t)|^2 \quad (2.9)$$

As laser power noise is usually the result of a stochastic process, it is often characterized by the one sided linear spectral density  $\text{RPN}(f)$  [23, 26, 27].

$$\text{RPN}(f) = \sqrt{\frac{G_P(f)}{\bar{P}^2}} \quad \text{in units of} \quad \left[ \frac{1}{\sqrt{\text{Hz}}} \right] \quad (2.10)$$

With  $G_P(f)$  being the one sided power spectral density of the laser noise, which can be used to calculate the amount of variation in the time series that is caused by frequencies in a narrow band around frequency  $f$  [28–30].

The contribution of frequencies in 1 Hz bandwidth around frequency  $f$  to the root mean square (RMS) relative power fluctuations  $m_{P, \text{RMS}, 1 \text{ Hz}}(f)$ , can be calculated as [31, Chapter 2.4][32, 33]:

$$m_{P, \text{RMS}, 1 \text{ Hz}}(f) = \sqrt{\int_{f-0.5 \text{ Hz}}^{f+0.5 \text{ Hz}} \text{RPN}(f)^2 df} \quad (2.11)$$

### 2.3 Phasor representation and sideband picture

Throughout this thesis a graphical illustration for modulated laser light fields will be utilized. In the phasor representation of a complex laser amplitude, the electric field  $\mathbf{U}(\vec{r}, t)$  is described as a vector in the complex plane, which rotates with the optical frequency  $\nu(t)$  [34–36]. We will assume a beam of constant amplitude  $\mathbf{U}_0(t) = \mathbf{U}_0$  and

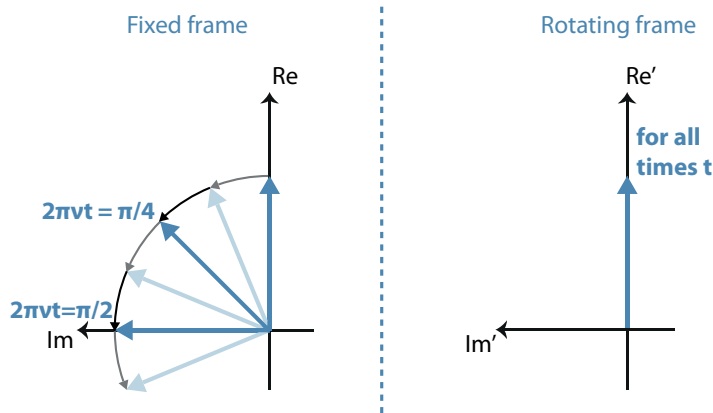


**Figure 2.2:** Left: The phasor of an electric field rotates in the fixed frame with its optical frequency  $\nu$ . Right: In the rotating frame (rotation with frequency  $\nu$ ) the phasor points up for all times  $t$ .

frequency  $\nu(t) = \nu$  and neglect the spatial components  $\sum c_{lm} \Psi_{lm}(\vec{r})$ . With these simplifications Equation 2.5 becomes:

$$\mathbf{U}(\vec{r}, t) = \mathbf{U}_0 \cdot e^{2\pi i \nu t} \quad (2.12)$$

The representation of the field at different times in the phasor diagram can be seen on the left side of Figure 2.2. Next we want to assume a rotating frame, which rotates exactly at the frequency  $\nu$  of the laser. In this frame the vector loses its time dependent component  $e^{2\pi i \nu t}$  and points always in the same direction, see Figure 2.2<sup>2</sup>.

### 2.3.1 Amplitude modulation and noise in the sideband picture

If we apply sinusoidal amplitude modulation with modulation coefficient  $m$  and modulation frequency  $f$  to this laser beam, this can be denoted as:

$$\begin{aligned} \mathbf{U} &= \mathbf{U}_0 (1 + m \cos(2\pi f t)) \\ &= \mathbf{U}_0 \left(1 + \frac{m}{2} e^{2i\pi f t} + \frac{m}{2} e^{-2i\pi f t}\right) \end{aligned} \quad (2.13)$$

The laser field consists of three components : a stationary component, which will be referred to as carrier component, and two so-called modulation sideband components.

<sup>2</sup>Extensive discussions of this topic can be found in [34, 35]

## 2 Laser power stabilization

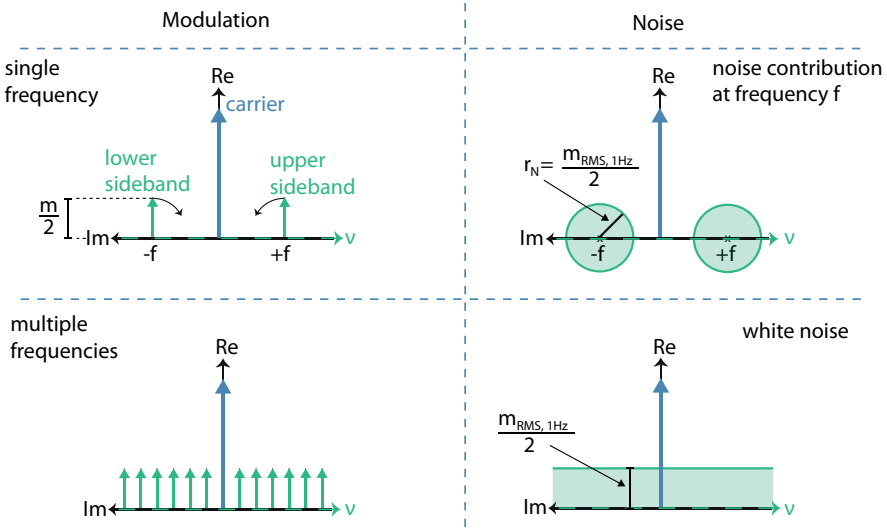


**Figure 2.3:** Left: Single and multiple amplitude modulations in the sideband picture. Right: Noise around a single frequency and white amplitude noise in the sideband picture

To be able to differentiate between the optical frequency  $\nu$  of different phasors an additional dimension is necessary. This can be done in two ways: Either a third axis is introduced, or the same axis is used for imaginary part and the optical frequency  $\nu$ . The later solution is the one chosen in the scope of this thesis. In this convention the base point of a phasor on the  $\nu$ -axis determines the frequency of the light field represented by the phasor.

In the rotating frame the carrier component always points upwards at all times  $t$  (see Figure 2.3). The sidebands are represented with a phasor at  $\nu = f$  and  $\nu = -f$ , which both point into the same direction as the carrier at  $t = 0$ . The upper sideband has a faster rotation than the carrier, hence it rotates counter-clockwise in the rotating frame, while the lower sideband rotates clockwise.

Noise, in contrast to a defined sinusoidal modulation, does not have a fixed phase or modulation coefficient and can only be described as a stochastic process using for instance a power spectral density.

We can use equation 2.11 to calculate the RMS noise contribution at a specific frequency  $f$ .

This noise contribution is then illustrated as circles with a radius

$$r_n = \frac{m_{\text{RMS},1\text{Hz}}(f)}{2} = \frac{m_{\text{P,RMS},1\text{Hz}}(f)}{4}, \quad (2.14)$$

around  $\nu = -f$  and  $\nu = f$  (see Figure 2.3)<sup>3</sup>. Noise with a constant power spectral density for all frequencies, will be referred to as white noise. It will be illustrated as a noise stripe with the height  $m_{\text{RMS},1\text{Hz}}(f)/2$ , throughout this thesis.

We now have defined an analytical way to describe laser beams and laser power noise. With this foundation, active and passive power stabilization schemes, as well as their advantages and disadvantages, are discussed next.

## 2.4 Noise sources

Fluctuations in the optical power of a laser beam can be caused by different noise sources, which will be divided into two different categories, the technical power noise and the quantum shot noise.

### 2.4.1 Shot noise

Every light beam consists of light quanta called photons. Each photon carries an energy of  $E_{\text{photon}} = h\nu$ , with  $h$  being the Planck constant,  $c$  the speed of light and  $\nu = c/\lambda$ , the frequency of the laser. Photons are statistically distributed on the laser beam following a Poisson distribution. Therefore, the number of photons arriving at a detector in a certain time interval is always fluctuating. This is typically referred to as quantum shot noise of a laser beam.

The relative shot noise of a laser beam with an optical power  $P$  can be described by its single sided linear spectral density:

$$\text{SN} = \sqrt{\frac{2hc}{P\lambda}}. \quad (2.15)$$

If the shot noise of a laser beam is detected using a photodiode, it is convenient to calculate the relative shot noise depending on the detected photocurrent  $i_D$  [22]:

$$\text{SN} = \sqrt{\frac{2e}{i_D}} = 1.8 \cdot 10^{-8} \text{ Hz}^{-1/2} \sqrt{\frac{1 \text{ mA}}{i_D}}, \quad (2.16)$$

with  $e$  being the elementary charge.

Classical laser light can not become more stable than the quantum

<sup>3</sup>This assumes both sidebands to be correlated at any point in time, such that the amplitude fluctuation can be calculated by adding up both sidebands.

## 2 Laser power stabilization

---

shot noise, therefore the shot noise is considered as a classical fundamental limit for power stability<sup>4</sup>.

### 2.4.2 Technical power noise

The stability of available laser light sources is usually limited by other noise sources, up to several MHz, which will be referred to as technical noise sources. Laser power fluctuations can be categorized into different categories:

- **Laser internal noise sources**

Power fluctuations can be produced inside the laser resonator itself by various sources. Fluctuating strength of the laser pump currents result into fluctuating output power of a laser [40, 41], other couplings can be induced by thermal fluctuations of the gain medium or mechanical disturbances in the laser resonator itself [27].

- **Laser external noise sources**

Outside the laser resonator, power fluctuations can be caused by dust particles falling through the beam, or beam pointing, which can be converted to power modulation in combination with clipping effects on optical components or due to varying throughput of an optical resonator.

Polarization fluctuations can be converted to power modulations by optical components with polarization dependent transmission, such as mirrors, polarizing beam splitter (PBS) or optical resonators [42]

If a beam is transmitted through an optical resonator, beam pointing of the beam incident to the resonator can be converted into power noise in transmission of the resonator as well. [22, 27].

- **Noise sources at the photodiode**

Laser power noise is usually measured with photodiodes, which convert the arriving photons into an electric current. Several noise sources can couple into the power noise measurement at

---

<sup>4</sup>In quantum mechanics, shot noise is a fundamental property of a coherent state, which is used to describe laser beams [37, Chapter 4]. It is possible to transfer uncertainty from the amplitude quadrature to the phase quadrature (and vice versa), by so called squeezing. The result is a squeezed state, with reduced amplitude/phase quantum noise compared to a coherent state [37–39]. However, we will use a classical approach to describe laser shot noise throughout this thesis.

## 2.5 Passive laser power stabilization

a photodiode. A frequently encountered noise source attributed to the detection process is scattered light [43, 44]. Furthermore, beam pointing fluctuations of the beam on the photodiode itself can couple either via clipping effects on the photodiode surface or due to an inhomogeneous responsivity of the photodiode surface.

- **Electronic noise**

Depending on the exact layout of the photodetector different noise sources can couple into the power noise measurement. This can be either resistor thermal noise, or input current or input voltage noise of operational amplifiers, which are regularly used in photodetectors. Photodiode dark noise or photodiode bias voltage fluctuations produce additional electronic noise in the detection process. An extensive study of these electronic noise sources can be found in [45].

## 2.5 Passive laser power stabilization

In passive power stabilization schemes the laser beam is guided through an optical component, which then leads to an attenuation of power fluctuations due to the specific properties of the component. Often optical resonators<sup>5</sup> are used to passively filter power fluctuations [46], but other optical components, such as Mach Zehnder interferometers [47] or saturated laser amplifiers [48–51], have been used for passive laser power stabilization as well.

The passive filtering of the optical component can be described by a transfer function analog to Section 2.1 with the input signal being  $P_{\text{in}}(t)$  or its finite Fourier transform  $P_{\text{in}}(f)$  respectively, and the output signal  $P_{\text{out}}(t)$  and  $P_{\text{out}}(f)$ , see Figure 2.4.

It is important to note that if we can find an analytical description, how a sinusoidal power modulations at the input of the optical component is converted to a sinusoidal modulation at its output, this transfer function can also be used for noise calculations (see Section 2.1).

Next we will analyze the fundamental properties of an optical resonator and derive a transfer function  $h(f)$ , which relates the resonator internal field amplitude to the incoming field amplitude.

This transfer function is used in the next step to describe the passive filter properties of an optical resonator with respect to transmitted

<sup>5</sup>Also referred to as optical cavities

## 2 Laser power stabilization

---

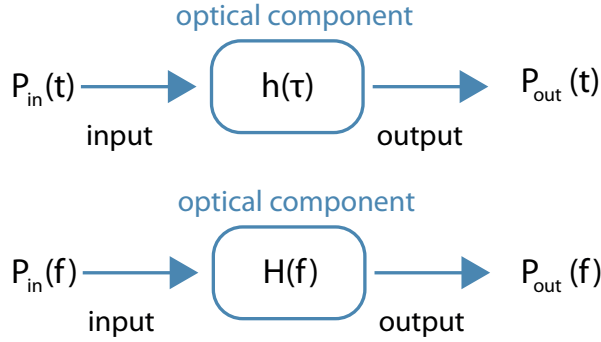


**Figure 2.4:** Passive filtering of power modulations at the input of the optical component in time domain and frequency domain

power modulations: It will also become essential for Chapter 3, in which transfer functions from incident modulations to reflected power modulations are derived.

### 2.5.1 Optical Resonators

The simplest optical resonator is a linear two mirror resonator, see Figure 2.5. If the distance between both mirrors is an integer multiple of half wavelengths of the light incident to the resonator ( $L = q\lambda/2$ ), light can start to resonate, since the field after one round trip in the resonator, interferes constructively with the field entering at the in-coupling mirror.

The difference between two successive frequencies which fulfill this requirement is called the free spectral range of the resonator  $\nu_{FSR}$  and depends solely on the distance between both mirrors  $L$ .

$$\nu_{FSR} = \nu_{q+1} - \nu_q = \frac{c}{2L} \quad \text{in units of [Hz]}. \quad (2.17)$$

The characteristic parameters of an optical resonator are the mirror amplitude reflectivities  $r_1, r_2$  and amplitude transmissivities  $t_1, t_2$ , which are connected by  $r_i^2 + t_i^2 = 1$ , and the resonator internal loss factor  $t_L$ .

To understand how an optical resonator can be used as passive filter for laser power fluctuations, it is useful to calculate the resonator internal fields  $U_1$  to  $U_4$ , the reflected field  $U_{refl}$  and the transmitted field  $U_{trans}$ , in dependence of the incoming field  $U_{in}$ , following [24, 25, 34, 52]. A phase shift of  $\pi/2$  is attributed for each transmission through a mirror to satisfy energy conservation.



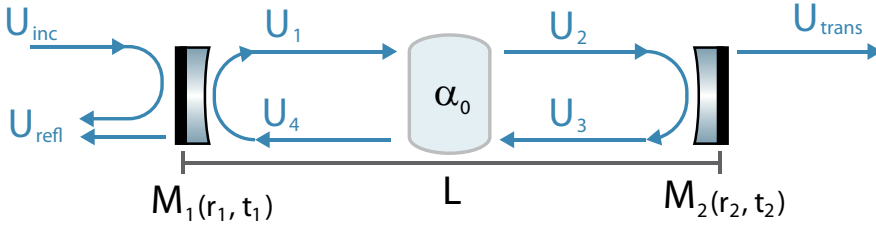


**Figure 2.5:** A linear resonator consisting of the two mirrors  $M_1$  and  $M_2$  with amplitude reflectivities  $r_i$  and transmissivities  $t_i$ , which are separated by the Length  $L$ . The incident, reflected, transmitted and circulating fields are illustrated in blue. The effect of resonator internal losses  $\alpha_0$  are indicated in the middle of the resonator

The field accumulates a phase shift of  $\exp(-i2\pi\nu L/c)$ , while it is propagating over the length  $L$  and to take account for resonator internal losses  $\alpha_0$ , the field gets attenuated by  $r_L = e^{\alpha_0 2L}$  for a complete round trip. Furthermore, it will be useful to define the round-trip gain  $g_{rt}$ :

$$g_{rt}(\nu) = r_1 r_2 r_L \exp(-i2\pi\nu \frac{2L}{c}) \quad (2.18)$$

A set of equations can be derived by following the field through one round-trip within the resonator:

$$U_1 = it_1 U_{in} + r_1 U_4, \quad (2.19)$$

$$U_2 = \sqrt{r_L} U_1 \cdot \exp(-i2\pi\nu L/c), \quad (2.20)$$

$$U_3 = r_2 U_2, \quad (2.21)$$

$$U_4 = \sqrt{r_L} U_3 \cdot \exp(-i2\pi\nu L/c), \quad (2.22)$$

$$U_{refl} = r_1 U_{in} + it_1 U_4, \quad (2.23)$$

$$U_{trans} = it_2 U_2, \quad (2.24)$$

This set of equations can be solved for  $U_4$  and  $U_2$ , which results in:

$$U_2 = U_{in} \frac{i\sqrt{r_L} r_2 t_1 e^{-i2\pi\nu \frac{L}{c}}}{1 - r_L r_1 r_2 e^{-i2\pi\nu \frac{2L}{c}}} \quad (2.25)$$

$$U_4 = U_{in} \frac{ir_L r_2 t_1 e^{-i2\pi\nu \frac{2L}{c}}}{1 - r_L r_1 r_2 e^{-i2\pi\nu \frac{2L}{c}}} \quad (2.26)$$

## 2 Laser power stabilization

---

Which can be used to find the reflected and transmitted field according to Eq. 2.23 and 2.24:

$$\mathbf{U}_{\text{trans}}(\nu) = -\frac{t_1 t_2 \sqrt{g_L}}{1 - g_{\text{rt}}} \mathbf{U}_{\text{in}}(\nu) \quad (2.27)$$

$$\mathbf{U}_{\text{refl}}(\nu) = \left( r_1 - \frac{t_1^2 g_{\text{rt}} / r_1}{1 - g_{\text{rt}}} \right) \mathbf{U}_{\text{in}}(\nu) \quad (2.28)$$

Intensity  $I_i(\nu)$  and the phase  $\Phi(\nu)$  of each field  $\mathbf{U}_i$  can be found using:

$$I_i(\nu) = |\mathbf{U}_i(\nu)|^2, \quad \Phi(\nu) = \text{Arg}(\mathbf{U}_i(\nu)) . \quad (2.29)$$

The power transmitted through the resonator is depicted in Figure 2.6, which also shows the linewidth  $\nu_{\text{LW}}$ , defined as Full-Width-Half-Maximum (FWHM) of the transmitted intensity:

$$\left| \mathbf{U}_{\text{trans}}\left(\pm \frac{\nu_{\text{LW}}}{2}\right) \right|^2 = \frac{1}{2} I_{\text{max}} \quad (2.30)$$

The linewidth  $\nu_{\text{LW}}$  can be calculated via the round trip gain  $g_{\text{rt}}$ :

$$\nu_{\text{LW}} = \nu_{\text{FSR}} \left( \frac{1 - g_{\text{rt}}}{\pi \sqrt{g_{\text{rt}}}} \right) , \quad (2.31)$$

Another important quantity used to characterize optical resonator is the Finesse  $\mathcal{F}$ , which is the ratio of free spectral range and linewidth.

$$\mathcal{F} = \frac{\nu_{\text{FSR}}}{\nu_{\text{LW}}} = \frac{\pi \sqrt{g_{\text{rt}}}}{1 - g_{\text{rt}}} . \quad (2.32)$$

It will be useful to express the optical transmission of the in-coupling mirror  $M_1$  and the out-coupling mirror  $M_2$ , as well as the resonator internal losses in the delta notation. With the power reflectivities  $R_j$ :

$$r_j^2 \equiv R_j \equiv e^{-\delta_j} \approx 1 - \delta_j , \quad (2.33)$$

and the resonator internal losses are defined as  $\delta_0 = 4\alpha_0 L$ . With the help of the delta notation, the linewidth and the Finesse can be rewritten as [24]:

$$\nu_{\text{LW}} = \nu_{\text{FSR}} \frac{\delta_2 + \delta_0 + \delta_1}{2\pi} \quad (2.34)$$

$$\mathcal{F} = \frac{2\pi}{\delta_2 + \delta_0 + \delta_1} \quad (2.35)$$

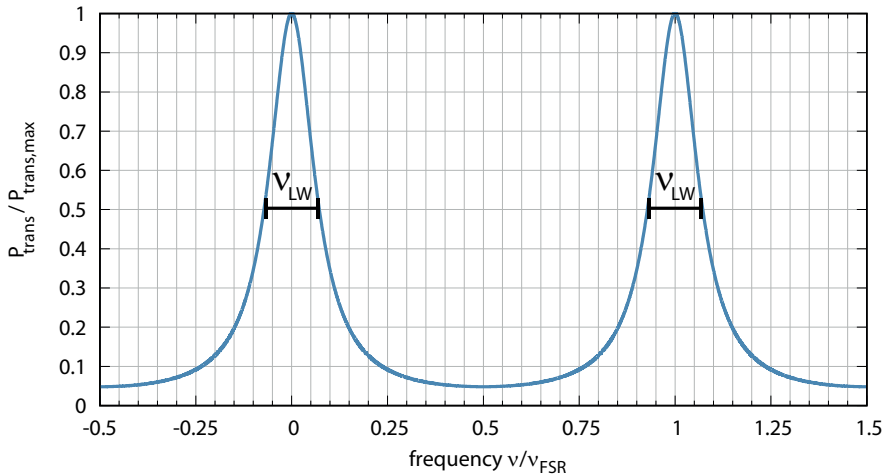


**Figure 2.6:** Normalized transmitted power of a lossless, impedance matched, optical Resonator. The FWHM of the transmitted power is defined as linewidth  $\nu_{\text{LW}}$ . The optical frequencies are normalized by the full spectral range  $\nu_{\text{FSR}}$ .

### 2.5.2 Frequency stabilization

To be able to transmit a laser beam through an optical resonator and use it as passive filter for power fluctuations, the laser frequency needs to be stabilized to the resonance frequency of the resonator.

This is usually achieved with a dedicated frequency stabilization feedback control loop actuating either on the laser frequency or the resonator length<sup>6</sup> Effectively the control loop minimizes the difference between the laser frequency  $\nu$  and the resonance frequency  $\nu_q$  of the resonator to  $|\nu - \nu_q| = 0$ .

The situation in which resonator length and laser frequency are stabilized to each other is often times referred to as the laser being locked to the resonator and vice versa.

Several different techniques have been developed to create an error signal for laser frequency stabilization between a laser and an optical

<sup>6</sup>Different parameters determine whether to actuate on the length of the resonator or the frequency of the laser. If for example a reduction of absolute laser frequency noise is desired, the laser frequency should be stabilized to a so called reference cavity with sufficient length stability.

## 2 Laser power stabilization

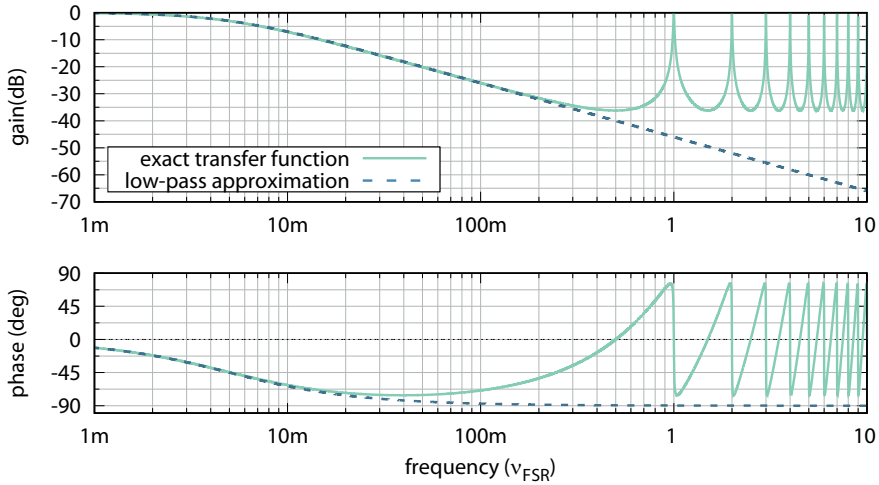


**Figure 2.7:** Bode diagram of the filter function of an optical resonator with respect to amplitude and power fluctuations showing the exact transfer function and the low-pass approximation

resonator [53–55].

A widely used technique is the so called Pound-Drever-Hall (PDH) locking method, which relies on RF-phase modulations sidebands imprinted on the light incident to the resonator [56, 57]. If the carrier is exactly resonant, the phase modulations can not be detected with a photodiode placed in reflection of the resonator. However, for a slight frequency offset between carrier and resonance frequency, a fraction of the phase modulation sidebands is converted into RF-amplitude modulation sidebands, which can be detected with a fast photodiode and, if demodulated correctly, results in the desired error signal.

### 2.5.3 Filter properties of the optical resonator

The filtering capabilities of the optical resonator become already obvious when looking at the transmitted optical power for different frequencies. To mathematically describe the filtering for power fluctuations, it is assumed that the laser frequency is locked to the resonator length.

An amplitude modulated laser beam can be described according to Eq. 2.13. The sideband components now undergo a different filtering than the carrier field, because their wavelength does not fit perfectly to the resonator length and therefore the sidebands are attenuated.

An analytical way to describe this filtering is found by calculating the resonator filter function  $h(f)$ , which is the ratio of the carrier field  $U_{\text{cav}}(0)$  inside the resonator and the sidebands inside the resonator  $U_1(f) = U_1^*(-f)$ . We will furthermore assume the lossless case with  $r_L = 1$  and equal mirror reflectivities  $r_1 = r_2 = r$ .

$$h(f) = \frac{U_1(f)}{U_1(0)} = \frac{1 - r^2}{1 - r^2 e^{-i2\pi f \frac{2L}{c}}} \quad (2.36)$$

$$\approx \frac{1}{1 + i \frac{f}{f_0}} \quad (2.37)$$

This approximation is done by expanding the exponential function for small frequencies and with the assumption that  $r \approx 1$  [58, 59]. The resonator corner frequency  $f_0$  marks the 3 dB attenuation point:

$$f_0 = \nu_{\text{FSR}} \frac{1 - r^2}{2\pi r^2} \approx \frac{\nu_{\text{FSR}}}{2\mathcal{F}} \approx \frac{\nu_{\text{LW}}}{2}. \quad (2.38)$$

The filter effect of the cavity is depicted in Figure 2.7, which shows the exact solution (Equation 2.36) and the low pass approximations (Equation 2.37). Sending a laser through an optical resonator therefore passively reduces the amplitude fluctuations for frequencies outside the resonator linewidth. Optical resonators are therefore often used to suppress laser noise at radio frequencies. A drawback of optical resonators is the lack of noise suppression at frequencies below or comparable to the corner frequency  $f_0$ .

### 2.5.4 Impedance matching

The impedance matching is defined as the reduction of the carrier field in reflection of a stabilized resonator and can be calculated by evaluating Equation 2.28 at the resonance frequency ( $|\nu - \nu_q| = 0$ ).

$$a = \frac{U_{\text{refl}}(0)}{U_{\text{inc}}(0)} = \frac{r_1 - r_2 r_L}{1 - r_1 r_2 r_L}. \quad (2.39)$$

Equation 2.39 can be rewritten into a more intuitive formula for the impedance matching, using the delta notation.

$$a = \frac{\delta_2 + \delta_0 - \delta_1}{\delta_2 + \delta_0 + \delta_1}. \quad (2.40)$$

This equation allows for an easy understanding of the impedance matching, which can have three different states.

## 2 Laser power stabilization

---

- ( $\alpha = 0$ , **impedance matched**,  $\delta_2 + \delta_0 = \delta_1$ ):  
The directly reflected field and the leakage field from the inside of the resonator have the same amplitude and therefore the resulting field vanishes.
- ( $\alpha > 0$ , **under-coupled**,  $\delta_2 + \delta_0 > \delta_1$ ):  
The directly reflected field is larger than the leakage field from the inside of the resonator. The phase of the resulting carrier component is the same as for the incoming field.
- ( $\alpha < 0$ , **over-coupled**,  $\delta_2 + \delta_0 < \delta_1$ ):  
The directly reflected field is smaller than the leakage field from the inside of the resonator. The resulting carrier component has a  $180^\circ$  phase flip compared to the input carrier field, which is indicated by the negative sign of  $\alpha$ .

The impedance matching will become an important parameter for the Optical AC Coupling technique introduced in Chapter 3.

### 2.5.5 Mode matching

Another important parameter attributed to optical resonators is the mode matching between the incoming beam and the fundamental resonator mode. The fundamental mode of the resonator is typically defined by the radii of curvature of the mirrors and the mirror separation.

A laser beam is referred to as being mode matched to an optical resonator, a perfect spatial overlap to the fundamental Eigenmode of the resonator can be achieved, which means it can be coupled completely to the fundamental mode of the resonator[60]. For a purely fundamental Gaussian beam incident to the resonator this requires perfect alignment and perfect positioning of the beam waist with respect to the beam waist of the resonator, as well as a perfect resemblance of the waist radius<sup>7</sup>. Mode matching of a laser beam to an optical resonator mostly refers to the optimization of both, alignment and waist position/size. However, sometimes mode matching is used exclusively for the fitting of the beam waist of the laser to the resonator.

---

<sup>7</sup>If a laser beam is not a pure fundamental Gaussian beam, but consists of higher order spatial modes, it can not be coupled completely to the fundamental mode of the resonator, unless the resonator has the so called confocal configuration.

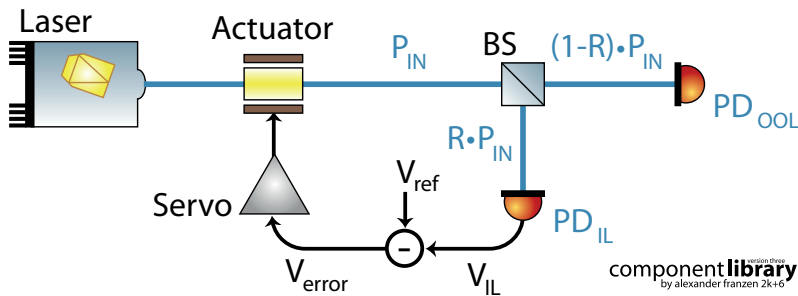


**Figure 2.8:** Active amplitude stabilization scheme, the incoming optical power  $P_{IN}$  is split up by a beam splitter with power reflectivity  $R$ . The in-loop beam is detected with  $PD_{IL}$  and converted into a voltage  $V_{IN}$ , which is compared to a stable reference voltage  $V_{ref}$  to create an error signal  $V_{error}$ . This error signal is conditioned for stable loop operation in the servo and fed back to an actuator. The out-of-loop beam is measured with  $PD_{OOL}$  for the stabilized and un-stabilized case.

## 2.6 Active laser power stabilization

A superior method to achieve power noise suppression at low frequencies is provided by active power stabilization schemes.

The principle of active power stabilization is shown in Fig.2.8. A portion of the light is separated with a beam splitter (power reflectivity  $R$ ) from the main laser beam and its power fluctuations are detected with a photo detector  $PD_{IL}$  referred to as in-loop detector. The photo detector converts the optical power into an electrical signal  $V_{IL}$ , which is compared to a very stable electrical reference voltage  $V_{ref}$ . In this way, an error signal  $V_{error}$  is created and conditioned by a so called servo, to allow for a stable loop operation [61]. Finally, the signal is fed back to an actuator which counteracts and thereby reduces the laser power noise, which is detected with the in-loop detector.

### 2.6.1 In-loop and out-of-loop measurements

In this way it is possible to achieve a very high noise suppression at low frequencies, compared to passive stabilization schemes. However, the performance of an active stabilization schemes can be degraded by sensor noise[27].

Each noise source arising in the error signal used for the feedback control loop, but which is not caused by actual power fluctuations of the laser beam, which is supposed to get stabilized, will be referred to as sensor noise.

## 2 Laser power stabilization

---

In the case of a power stabilization feedback control loop, sensor noise can arise due to several effects:

- Except the internal laser noise sources, every noise source discussed in Section 2.4.2, can produce additional power noise on the beam, which is detected with the in-loop-sensor of the feedback control loop.
- In addition to already discussed electronic noise sources, fluctuations of the reference voltage used to create the error signal can produce electronic sensor noise [27].
- Since the power of the laser beam incident to the in-loop detector, is reduced compared to the power incident to the beam-splitter  $P_{IN}$ , its relative shot noise is higher than on the original beam. Therefore, shot noise is a fundamental additional sensor noise source for every active power stabilization scheme.

Since the feedback control loop will try to counter-act the sensor noise it can, in a worst case scenario, produce an increased out-of-loop laser power noise.

It is therefore crucial to reduce any excess sensor noise such that it is not limiting the performance of the control loop. Therefore, the ultimate goal for every classical active power stabilization feedback loop is to be limited by the shot noise of the in-loop detector, which depends purely on the total amount of detected optical power. The fundamental shot noise limited stability for a classical active stabilization scheme is calculated with respect to the shot noise levels of the beam incident to the in-loop detector and the shot noise level of the out-of-loop beam. Both shot noise levels are connected by the reflectivity  $R$  of the beam splitter, which is used to separate the in-loop beam from the out-of-loop beam. The out-of-loop relative shot noise for an the un-stabilized beam (loop not closed) is given by:

$$SN_{OOL} = \sqrt{\frac{2hc}{P_{IN}\lambda(1-R)}}, \quad (2.41)$$

while the in-loop beam has a relative shot noise of  $SN_{IL}$ :

$$SN_{IL} = \sqrt{\frac{2hc}{P_{IN}\lambda R}}. \quad (2.42)$$



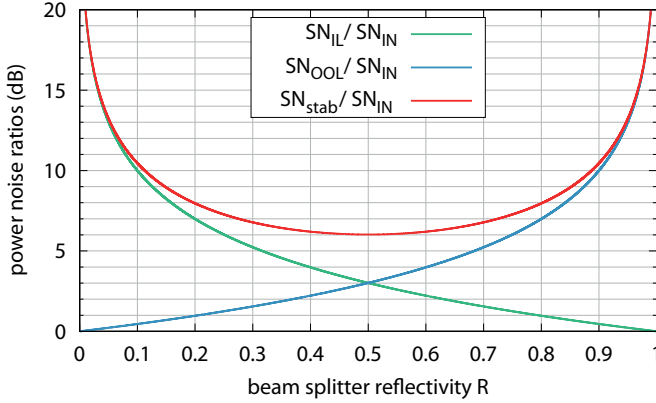


**Figure 2.9:** Fundamental shot noise limit of traditional active laser power stabilization feedback  $SN_{stab}$  and in-loop and out-of-loop relative shot noise levels  $SN_{IL}$  and  $SN_{OOL}$  normalized by the relative shot noise of the initial beam  $SN_{IN}$ .

The shot noise of the in-loop and out-of-loop beam are depicted in Figure 2.9, which shows  $SN_{IL}$ ,  $SN_{OOL}$  and the relative power noise of the stabilized out-of-loop beam for infinite loop gain, normalized with the relative shot noise level of the initial beam  $SN_{IN}$ .

The shot noise limited relative out-of-loop stability for the stabilized case  $SN_{stab}$  is calculated as the uncorrelated sum of both shot noise levels, according to<sup>8</sup>:

$$\begin{aligned}
 SN_{stab} &= \sqrt{(SN_{OOL})^2 + (SN_{IL})^2} \\
 &= \sqrt{\frac{2hc}{P_{IN}\lambda R} + \frac{2hc}{P_{IN}\lambda(1-R)}} \\
 &= \sqrt{\frac{2hc}{R(1-R)P_{IN}\lambda}}.
 \end{aligned} \tag{2.43}$$

To understand the stabilized relative power noise it is crucial to remind that the active power stabilization feedback control loop will try to counteract the relative shot noise of the in-loop beam. For small reflectivities the relative shot noise of the in-loop beam is significantly higher than the shot noise level of the out-of loop-beam. If the loop is closed, the shot noise of the in-loop beam will be imprinted on the out-of-loop beam.

<sup>8</sup>Which assumes the shot noise of the in-loop beam and the out-of-loop beam to be uncorrelated

## 2 Laser power stabilization

---

In the situation where  $R \approx 1$  the relative shot noise of the in-loop beam is significantly smaller than the relative out-of-loop shot noise. Even though, the feedback control loop can now measure and suppress the technical laser noise to its own shot noise limit, the out of loop beam will be limited by its own relative shot noise in this situation. The best out-of-loop performance can be achieved by choosing  $R = 0.5$ , which results in an out-of-loop stability which is 6 dB above the relative shot noise of the incoming beam.

However, detecting 50% of the optical power of the initial beam is not desired in many cases. This can be either because it is not desired to lose so much power just for stabilization purposes, or in the case of high power laser systems the power would simply be too much to be handled by the photo detectors.

This is why in many experiments the beam splitter ratio is chosen to be significantly smaller than  $R = 0.5$  and most stabilization schemes are limited by the shot noise of the in-loop detector.

### 2.7 State of the art laser power stabilization

The second generation of gravitational wave detectors required a relative power stability of  $2.0 \cdot 10^{-9} \text{ Hz}^{-1/2}$  at 10 Hz for the light injected into the interferometer [16].

Triggered by these high demands research development of power stabilization feedback control loops became a very active field of research [42, 44, 45].

A major obstacle in reaching the required performance was the development of a sensor with sufficiently low sensor noise which was capable of detecting the photocurrent of  $i_D = 100 \text{ mA}$ , which is necessary to have sufficiently low relative shot noise. Current noise in resistor and noise of the InGaAs photodiodes used for the power detection were identified to produce low frequency excess noise, which scaled with the detected photocurrent [27].

Finally, the required stability was demonstrated for the first time in 2009 with a photodiode array, consisting of 8 photodiodes, which detected a total photocurrent of 400 mA [18]. Four photodiodes each were used for in-loop detection and an independent out-of-loop measurement, reducing the photocurrent detected with each photodiode to 50 mA.

It is still a topic of research how much more photocurrent per photodiode might be detectable due to better photodiode manufacturing,

## 2.7 State of the art laser power stabilization

---

since especially the low frequency excess noise of photodiodes is still not fully understood. However, at some point the limit for a single photodiode will be reached and a further improvement will only be possible by further scaling the number of photodiodes used for detection. This approach will rather quickly become increasingly complex, due to the scaling of the relative shot noise, which only decreases with the square root of the detected optical power.

Therefore, other novel techniques for laser power stabilization were proposed and tested, amongst them the Optical AC coupling technique, which is introduced in the next chapter.



## 3

## Chapter 3

## Optical AC coupling

As discussed in the previous section a high amount of optical power has to be detected to reduce the shot noise limit of a classical active power stabilization control loop. This will become one of the major obstacles in reaching relative power stabilities far beyond a stability of  $2.0 \cdot 10^{-9} \text{ Hz}^{-1/2}$ .

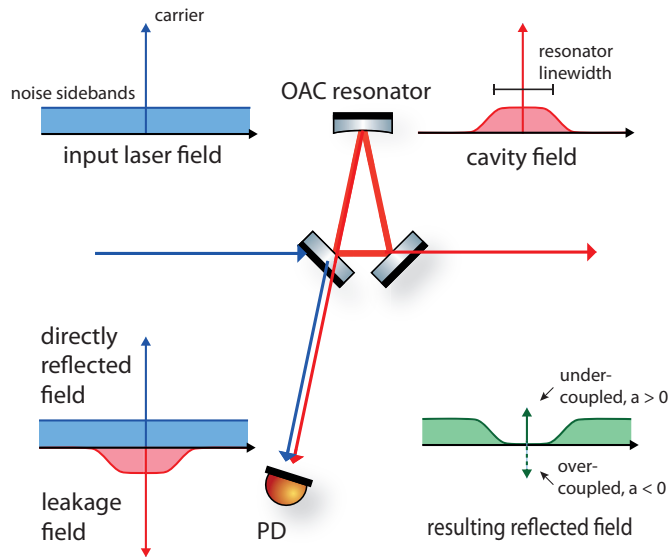
Optical AC coupling (OAC) is a novel approach for laser power stabilization, which allows to reduce the optical power on the in-loop detector of an active power stabilization scheme, without losing shot noise limited sensitivity to relative power fluctuations of the beam [19]. As introduced in Section 2.5 an optical resonator acts as a low-pass filter for transmitted laser power fluctuations. Vice versa, it acts as a high-pass filter for the light reflected from the resonator. This can be exploited to increase the ratio of relative technical noise to relative shot noise on a photodetector, placed in reflection of the resonator.

Figure 3.1 illustrates the basic idea of OAC in the sideband picture, which was introduced in Section 2.3.1. The laser, which is locked to the resonance frequency of the resonator, consists of its carrier component and a white noise floor of technical amplitude noise. Furthermore, the beam is assumed to be perfectly mode matched to the fundamental mode of the resonator.

Depending on the input mirror reflectivity a fraction of the light is directly reflected, while a small fraction of the light is transmitted into the resonator. Inside the resonator only the carrier component and the noise sidebands within the resonator linewidth are resonantly enhanced (see Section 2.5.1) and therefore the intra-cavity field looks like a low-pass filtered version of the incoming field.

A fraction of the intra-cavity field leaks out in transmission of the res-

### 3 Optical AC coupling



**Figure 3.1:** Optical AC Coupling illustration in the sideband picture. The input field of the resonator consists of the carrier and a white noise floor. The carrier and the noise sidebands within the linewidth of the resonator, are resonantly enhanced inside of the resonator. A portion of the intra-cavity field leaks into transmission and another portion into the reflection port of the resonator. The field in reflection is composed of the field directly reflected at the input mirror and the field leaking out of the cavity into the reflection port. The resulting reflected field has a reduced carrier and reduced noise sidebands within the resonator linewidth, while the noise sidebands outside the linewidth are preserved at their original height. The impedance matching determines the phase relation between carrier component and noise sidebands in reflection of the resonator (Reproduced from [62]. © IOP Publishing Ltd. CC BY 3.0).

---

onator and, for the understanding of the OAC concept more importantly, into the reflection port of the resonator. Hence, the reflected electrical field is a superposition of the directly reflected field and the leakage field coming from the inside of the optical resonator.

This superposition of the two field contributions leads to an attenuation of the carrier component and a frequency dependent attenuation of the noise sidebands. Inside the resonator linewidth the noise sidebands are attenuated in the same way as the carrier component. However, the noise sidebands outside the resonator linewidth are preserved at their original height, since they originate from the direct reflection at the input mirror of the resonator.

This is the essential trick of Optical AC coupling; the amount of DC power on the detector is reduced, but for frequencies outside the resonator linewidth the signal, containing the information for the power stabilization sensor, is preserved at its original height.

A detector in reflection of the resonator therefore can achieve a shot noise limited sensitivity equivalent to the detection of the full optical power incident to the resonator, while the actual optical power on the detector is significantly reduced. The increase in sensitivity is maximized for frequencies outside of the resonator linewidth, however, even for smaller frequencies an increased sensitivity is achieved.

It turns out that for a perfectly mode matched resonator the enhancement, which can be achieved with OAC does solely depend on the impedance matching  $\alpha$ , which was defined in Section 3.1.

Especially for the experiments performed in the scope of this thesis, the influence of imperfect mode matching could not be neglected and will therefore be discussed with respect to the achievable Optical AC coupling gain in Section 3.2. A parameter optimization, necessary to achieve the maximum gain for a certain mode matching, is presented in Section 3.3.

Optical AC coupling is a possible means by which the limitations of a classical active power stabilization scheme can be overcome. However, initial experiments demonstrated that the resonator itself can produce excess power noise in reflection of the resonator, which degrades the out of loop performance of an OAC based power stabilization feedback control loop[22].

The most important noise couplings which can be induced by the OAC resonator, are discussed in Section 3.5. Especially the conversion from incident frequency noise to power noise in reflection of the OAC resonator is extended, compared to previous estimates[22], to

### 3 Optical AC coupling

---

take account for the imperfect mode matching situation.

#### 3.1 OAC Transfer function

The resonator can be described by an analytic transfer function  $h(f)$  (see Section 2.5) which will be used to calculate a transfer function from relative power modulations incident to the resonator to relative power modulations in reflection of the resonator. This transfer function will be referred to as Optical AC coupling transfer function [21, 22, 63, 64]. The incoming laser light field  $U_{in}$  has an amplitude  $U_0$  and is amplitude modulated at frequency  $2\pi f$  with a modulation coefficient  $m$ .

$$\begin{aligned} U_{in}(f) &= U_0 (1 + m \cos(2\pi ft)) \\ &= U_0 \left(1 + \frac{m}{2} e^{2i\pi ft} + \frac{m}{2} e^{-2i\pi ft}\right) \end{aligned} \quad (3.1)$$

This is equivalent to an input power  $P_{in}(f) = U_{in}(f) \cdot U_{in}^*(f)$ ,

$$\begin{aligned} P_{in}(f) &= U_0^2 (1 + 2m \cos(2\pi ft)) \\ &= \underbrace{U_0^2}_{P_{in,DC}} + \underbrace{2m U_0^2 \cos(2\pi ft)}_{P_{in,AC}} \end{aligned} \quad (3.2)$$

and therefore the relative power noise of the incoming beam  $RP_{in}(f)$  can be denoted as:

$$RP_{in}(f) = \frac{P_{in,AC}(f)}{P_{in,DC}} = 2m \cos(2\pi ft). \quad (3.3)$$

The field inside the cavity impinging on the input mirror  $M_1$  is given by<sup>1</sup>:

$$U_{cav}(f) = \frac{r-a}{t} \cdot U_0 \left(1 + h(f) \frac{m}{2} e^{2i\pi ft} + h(-f) \frac{m}{2} e^{-2i\pi ft}\right), \quad (3.4)$$

where  $a$  is the impedance matching of the resonator and  $(r, t)$  are the amplitude reflectivity/transmissivity of the input mirror of the resonator. The field in reflection of the cavity is given as superposition

---

<sup>1</sup>A close comparison to Eq. 2.23, 2.28 and 2.39 shows that this is yet another approximation, since a small phase-difference accumulated by the sidebands in one round-trip compared to the carrier is neglected, which can be done for frequencies significantly smaller than the free spectral range  $f \ll \nu_{FSR}$



of the directly reflected field contribution and the leakage field from inside of the cavity:

$$\mathbf{U}_{\text{refl}}(f) = r \cdot \mathbf{U}_{\text{in}} - t \cdot \mathbf{U}_{\text{cav}} \quad (3.5)$$

$$\begin{aligned} &= a\mathbf{U}_0 + [r - (r - a) h(f)] \mathbf{U}_0 \frac{m}{2} e^{2i\pi ft} \\ &\quad + [r - (r - a) h(-f)] \mathbf{U}_0 \frac{m}{2} e^{-2i\pi ft} \end{aligned} \quad (3.6)$$

The reflected power  $P_{\text{refl}} = \mathbf{U}_{\text{refl}} \cdot \mathbf{U}_{\text{refl}}^*$ , for  $r \approx 1$ , can be denoted as:

$$\begin{aligned} P_{\text{refl}}(f) &= a^2 \mathbf{U}_0^2 + \underbrace{a[1 - (1 - a) h(f)]}_{K_+(f)} \mathbf{U}_0^2 m e^{2i\pi ft} \\ &\quad + \underbrace{a[1 - (1 - a) h(-f)]}_{K_-(f)} \mathbf{U}_0^2 m e^{-2i\pi ft} \end{aligned} \quad (3.7)$$

The complex coefficients  $K_+(f)$  and  $K_-(f)$  are the complex conjugate of each other. With  $K_+(f) = (K_-(f))^* = K(f)$  the power in reflection  $P_{\text{refl}}(f)$  can be rephrased as:

$$P_{\text{refl}}(f) = \underbrace{a^2 \mathbf{U}_0^2}_{P_{\text{refl,DC}}} + \underbrace{2m|K(f)|\mathbf{U}_0^2 \cos(2\pi ft + \text{Arg}[K(f)])}_{P_{\text{refl,AC}}} \quad (3.8)$$

The magnitude of  $K(f)$  given by:

$$|K(f)| = a^2 \sqrt{\frac{1 + g^2 \cdot f^2/f_0^2}{1 + f^2/f_0^2}} \quad (3.9)$$

The parameter  $g$  will be referred to as the Optical AC coupling gain factor and is inversely proportional to the impedance matching  $a$ , in the situation of perfect mode matching:

$$g = \frac{1}{a} \quad (3.10)$$

The relative power fluctuation of the reflected beam  $RP_{\text{refl}}(f)$  is defined as:

$$RP_{\text{refl}}(f) = \frac{P_{\text{refl,AC}}(f)}{P_{\text{refl,DC}}} = \frac{2m}{a^2} |K(f)| \cos(2\pi ft + \underbrace{\text{Arg}[K(f)]}_{\kappa(f)}) \quad (3.11)$$

We define the Optical AC coupling transfer function  $G_{\text{OAC}}(f)$  as:

$$G_{\text{OAC}}(f) = \frac{|RP_{\text{refl}}(f)|}{|RP_{\text{in}}(f)|} e^{i\phi_{\text{refl}}} = \sqrt{\frac{1 + g^2 \cdot f^2/f_0^2}{1 + f^2/f_0^2}} \cdot e^{i\kappa(f)} \quad (3.12)$$

### 3 Optical AC coupling

---

The OAC transfer function allows to estimate how an incoming relative power fluctuation  $RP_{in}$  is converted by the resonator into a the relative power fluctuation  $RP_{refl}$  in its reflection.

The shot noise limited sensitivity of a classical detector for relative power noise at the detector is given by Eq.2.16. For a photodetector that is placed in reflection of an optical resonator and detects a photocurrent  $i_D$ , this sensitivity depends additionally on the magnitude of the OAC transfer function  $G_{OAC}(f)$  [22]:

$$s_{OAC}(f) = \frac{1}{|G_{OAC}(f)|} \sqrt{\frac{2e}{i_D}} \quad (3.13)$$

Therefore, an power stabilization using an OAC based detector, can reach a better shot noise limited out-of-loop performance compared to a classical power stabilization setup if both setups detected the same photocurrent

A Bode diagram of the Optical AC coupling transfer function for an under-coupled and over-coupled resonator is shown in Figure 3.2. For frequencies far below the corner frequency  $f_0$  the gain factor is 1 because the sidebands and the carrier both get attenuated by the same amount. With higher frequencies the gain starts to increase until it settles at  $|g|$  for frequencies far above  $f_0$ . With respect to the magnitude, the OAC transfer functions of both impedance matchings are completely the same. However, they have a different behavior with respect to their phase. While the phase of the under-coupled transfer function goes to  $0^\circ$  for high frequencies, in the over-coupled situation the phase acquires a phase flip of  $180^\circ$ . This is because the noise sidebands outside the resonator linewidth and the resulting carrier component of the reflected field have exactly this phase flip with respect to each other.

### 3.2 Imperfect mode matching

The situation becomes more difficult if the input laser beam consists of resonant and non-resonant laser modes, such as higher order spatial modes or RF-modulation sidebands. A calculation of the transfer function has to account for these non-resonant modes. We will distinguish between the resonant part  $U_0$  and non-resonant modes  $U_1$ , which are connected by optical power  $P_0$  and the mode matching co-

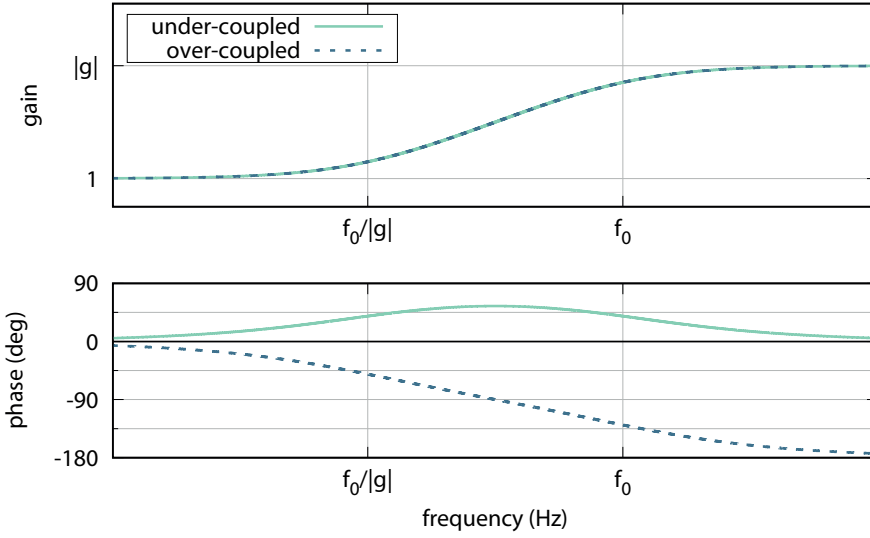


**Figure 3.2:** OAC transfer function  $G_{\text{OAC}}(f)$  from relative power modulations on the incoming beam to relative power modulations in reflection of a cavity for under- and over-coupled impedance matching.  $f_0$  is the corner frequency of the resonator and  $g$  is the Optical AC coupling gain factor

efficient  $p$ :

$$P_0 = U_0^2 + U_1^2 \quad (3.14)$$

$$U_0^2 = (1 - p)P_0 \quad (3.15)$$

$$U_1^2 = pP_0 \quad (3.16)$$

The input field is then denoted as:

$$U_{\text{in}}(f) = (U_0 + U_1) (1 + m \cos(2\pi ft)) \quad (3.17)$$

$$= (U_0 + U_1) \left(1 + \frac{m}{2}e^{i2\pi ft} + \frac{m}{2}e^{-i2\pi ft}\right) \quad (3.18)$$

and after normalization of the total optical power  $P_0 = 1$ , the power modulation  $P_{\text{in}}(f)$  can be expressed as:

$$P_{\text{in}}(f) = \underbrace{1}_{P_{\text{in,DC}}} + \underbrace{2m}_{P_{\text{in,AC}}} \cos(2\pi ft) \quad (3.19)$$

Following the analysis in Section 3.1, the reflected field  $U_{\text{refl}}$  can be expressed as the sum of the directly reflected field and the cavity

### 3 Optical AC coupling

---

leakage field:

$$\begin{aligned}
 U_{\text{refl}}(f) &= r \cdot U_{\text{in}} - t \cdot U_{\text{cav}} & (3.20) \\
 &= r \cdot (U_0 + U_1) \cdot \left(1 + \frac{m}{2}e^{2i\pi ft} + \frac{m}{2}e^{-2i\pi ft}\right) \\
 &\quad - (r - a) \cdot U_0 \cdot \left(1 + h(f)\frac{m}{2}e^{2i\pi ft} + h(-f)\frac{m}{2}e^{-2i\pi ft}\right) \\
 &= aU_0 + rU_1 \\
 &\quad + [(r - (r - a)h(f))]U_0 + rU_1 \frac{m}{2}e^{2i\pi ft} \\
 &\quad + [(r - (r - a)h(-f))U_0 + rU_1] \frac{m}{2}e^{-2i\pi ft}
 \end{aligned}$$

The reflected optical power can be calculated for  $r \approx 1$  as  $P_{\text{refl}} = U_{\text{refl}} \cdot U_{\text{refl}}^*$ :

$$\begin{aligned}
 P_{\text{refl}}(f) &= a^2 U_0^2 + U_1^2 & (3.21) \\
 &\quad + \underbrace{[a(1 - (1 - a)h(f))] U_0^2 + U_1^2}_{J_+(f)} me^{2i\pi ft} \\
 &\quad + \underbrace{[a(1 - (1 - a)h(-f))] U_0^2 + U_1^2}_{J_-(f)} me^{-2i\pi ft}
 \end{aligned}$$

Analog to the case of perfect mode matching, the complex sideband coefficients are complex conjugates of each other and therefore  $P_{\text{refl}}$  can be denoted as:

$$P_{\text{refl}}(f) = \underbrace{(a^2(1 - p) + p)}_{P_{\text{refl,DC}}} + \underbrace{2m|J(f)|}_{P_{\text{refl,AC}}} \cos(2\pi ft + \underbrace{\text{Arg}[J(f)]}_{J(f)}) \quad (3.22)$$

The resulting magnitude of  $G_{\text{OAC}}(f)$  can be reduced to exactly the same form as for the mode matched case:

$$G_{\text{OAC}}(f) = \sqrt{\frac{1 + [g(a, p)]^2 \cdot f^2/f_0^2}{1 + f^2/f_0^2}} \cdot e^{ij(f)} \quad (3.23)$$

The only difference to Eq.3.12 is the the definition of the Optical AC coupling gain factor  $g(a, p)$ , which now depends on impedance matching  $a$  and the mode matching coefficient  $p$ :

$$g(a, p) = \frac{a(1 - p) + p}{a^2(1 - p) + p} \quad (3.24)$$

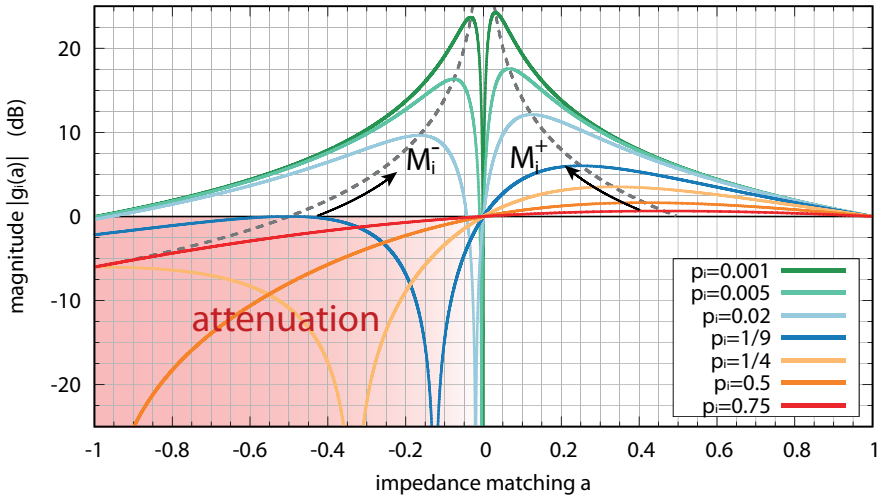


**Figure 3.3:** The OAC gain factor  $g_i(a)$ , for specific values of the mode matching coefficient  $p_i$ , in dependence of the impedance matching  $a$ . In grey you can see  $E(a)$  which is the locus of the maximum points  $M_i^+$  and  $M_i^-$ .

### 3.3 OAC gain optimization

For imperfect mode matching  $p > 0$ , the Optical AC coupling gain factor  $g(a, p)$  is a non-linear function of  $a$  and  $p$ , which can be optimized.

To develop an understanding of the influence of  $a$  and  $p$  on the magnitude of the OAC gain factor,  $|g(a, p_i)|$  is illustrated in the logarithmic dB scale for different fixed mode matching coefficients  $p_i$  in Figure 3.3.

For a fixed mode matching coefficient  $p_i$  the OAC gain factor solely depends on the impedance matching  $a$  and therefore becomes  $g_i(a) = g(a, p_i)$ .

Following the curves in Figure 3.3, starting at the under-coupled right side ( $a = 1$ ), the gain increases for every mode matching coefficient until it reaches a maximum  $M_i^+ = |g_i(a_i^+)|$ .

Going towards smaller impedance matching values the gain decreases to  $|g_i(0)| = 1$  (0 dB) at  $a = 0$ .

The gain decreases even further (this means it becomes an attenuation) until it becomes  $|g_i(a_i^z)| = 0$  at  $a_i^z = \frac{p_i}{p_i - 1}$ , which corresponds to a pole in the logarithmic scale. This point is not reached for  $p_i > 0.5$  since this would require  $a < -1$  and this is not allowed.

For  $p_i < 0.5$  the curves  $g_i(a)$  start to increase again for  $a < a_i^z$  and

### 3 Optical AC coupling

---

for  $p_i < 1/4$  another local maximum  $M_i^- = |g_i(\alpha_i^-)|$  is reached.

However for  $1/4 > p_i > 1/9$ , the maximum  $M_i^-$  is still an attenuation  $M_i^- < 1$  (0 dB). This means to make efficient use of the OAC technique in an over-coupled situation, the mode matching has to be better than  $p_0 = 1/9$ . Note that  $M_i^+$  stays above 0 dB for every possible mode matching coefficient  $p_i$ .

The impedance matchings  $\alpha_i^+$  and  $\alpha_i^-$  which maximize  $|g_i(\alpha)|$  for a certain mode matching coefficient are calculated as the zero crossings of the derivative of  $|g_i(\alpha)|$  with respect to  $\alpha$ .

$$\frac{d}{d\alpha}|g_i(\alpha)| \stackrel{!}{=} 0 \quad (3.25)$$

$$\Rightarrow \alpha_i^+ = \frac{p_i - \sqrt{p_i}}{p_i - 1} \quad \text{and} \quad \alpha_i^- = \frac{p_i + \sqrt{p_i}}{p_i - 1} \quad (3.26)$$

The magnitude of these two maximum values  $M_i^+$  and  $M_i^-$  is calculated as:

$$M_i^+ = |g_i(\alpha_i^+)| = \frac{1}{2} \sqrt{\frac{(\sqrt{p_i} + 1)^2}{p_i}} \quad (3.27)$$

$$M_i^- = |g_i(\alpha_i^-)| = \frac{1}{2} \sqrt{\frac{(\sqrt{p_i} - 1)^2}{p_i}} \quad (3.28)$$

Note that  $M_i^-$  is a smaller than  $M_i^+$ , which will be explained later.

Solving  $\alpha^+(p)$  and  $\alpha^-(p)$  for  $p$  delivers additional information.

$$\Rightarrow p^+(\alpha) = p^-(\alpha) = \frac{\alpha^2}{(\alpha - 1)^2} \quad (3.29)$$

The two values  $p^+$  and  $p^-$  specify which mode matching coefficients maximize the gain for a given impedance matching  $\alpha$  and therefore give the locus  $E(\alpha) = g(\alpha, \frac{\alpha^2}{(\alpha-1)^2}) = \frac{1}{2\alpha}$  of the two maximum values in Figure 3.3.

Remember two important characteristics of this figure:

- The magnitude reaches two local maximum values,  $M_i^+$  for positive impedance matching and  $M_i^-$  for negative impedance matching.
- In the over-coupled situation ( $\alpha < 0$ ) a mode matching coefficient better than  $p_0 = 1/9$  is required to make efficient use

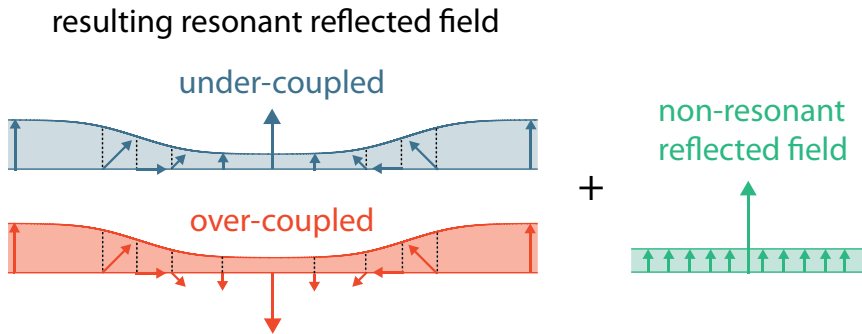


**Figure 3.4:** Field contributions in reflection of the OAC resonator for imperfect mode matching. The reflection of the optical resonator consists of the resulting resonant field contribution and non-resonant field contributions in reflections of an OAC resonator.

of the OAC technique. However, this requires an exact tuning of the impedance matching  $\alpha$  to a parameter region, in which amplification  $|g| > 0$  dB is achieved.

To understand the difference between the over-coupled and under-coupled side of Figure 3.3, it is important to have a look at the field contributions in reflection of the OAC resonator in the presence of non-resonant mode content, see Figure 3.4.

The non-resonant mode content  $p$ , is completely reflected at the incoupling mirror of the resonator and therefore contributes a carrier component, as well as attributed noise sidebands.

Since they are not affected by the resonator, the non-resonant sidebands stay at the same relative level compared to their carrier.

Conversely, the resonant contribution of the field is subject to the OAC transfer function. In addition to the attenuation, the noise sidebands acquire a frequency dependent phase shift compared to the resonant carrier.

This is illustrated by looking at defined amplitude modulations, in Figure 3.4. In the under-coupled situation, this phase-shift is only significant for frequencies in between  $f_0/|g|$  and  $f_0$ . As a result the noise sidebands above the corner frequency are in phase with the carrier.

In the over-coupled situation the phase shift at high frequencies is  $180^\circ$ , which means carrier and sidebands are exactly out of phase and a power increase incident to the OAC resonator looks like a power decrease in reflection of the resonator.

### 3 Optical AC coupling

---

The power noise in reflection of the OAC resonator is the sum of the beats between the carrier and the noise sideband of the resonant and the non-resonant contribution.

Since the resonant power noise contribution is  $180^\circ$  phase shifted to the non-resonant contribution, they can cancel each other out for certain parameter combinations of  $\mathbf{a}$  and  $\mathbf{p}$ .

Hence, as soon as the beat between the reflected resonant carrier with its noise sidebands, becomes comparable to the beat between the non-resonant carrier and its sidebands, the OAC gain factor is reduced.

Figure 3.3 shows, that also for the under-coupled situation a higher non-resonant mode content results into a reduced OAC gain factor.

However, in this situation this is simply explained with a reduced resonant mode content, which is getting smaller than the classically attenuated non-resonant mode content. Therefore, the minimum gain in the under-coupled situation is limited to of 0 dB.

#### 3.4 Estimation of $\mathbf{a}$ and $\mathbf{p}$ from DC reduction and OAC gain

It is possible to estimate  $\mathbf{a}$  and  $\mathbf{p}$  from independent measurements of the DC reduction  $\zeta(\mathbf{a}, \mathbf{p})P_{\text{in,DC}} = P_{\text{refl,DC}}$  (see Equation 3.22) and the OAC gain factor  $g(\mathbf{a}, \mathbf{p})$ .

$$\zeta = \mathbf{a}^2(1 - \mathbf{p}) + \mathbf{p} \quad (3.30)$$

$$g = \frac{\mathbf{a}(1 - \mathbf{p}) + \mathbf{p}}{\mathbf{a}^2(1 - \mathbf{p}) + \mathbf{p}} \quad (3.31)$$

To estimate  $\mathbf{a}(\zeta, g)$ , Eq. 3.30 is solved for  $\mathbf{p}$ , which is then inserted into 3.31. Now we solve this for  $\mathbf{a}$  and get the impedance matching in dependence of the carrier reduction  $\zeta$  and OAC gain factor  $g$ .

$$\mathbf{a}(\zeta, g) = \frac{\zeta - g\zeta}{g\zeta - 1} \quad (3.32)$$

In a similar fashion we can develop  $\mathbf{p}(\zeta, g)$ : Solve eq.3.30 for  $\mathbf{a}$ , insert into 3.31 and solve for  $\mathbf{p}$ .

$$\mathbf{p}(\zeta, g) = \frac{\zeta(g^2\zeta - 1)}{2g\zeta - 1 - \zeta} \quad (3.33)$$



These equations are useful to characterize a system with respect to mode matching coefficient  $p$  and  $a$  and were used for the estimates presented in Chapter 5.

## 3.5 Noise couplings

The basic implementation of Optical AC coupling in an active power stabilization is illustrated in Figure 3.5. The assembly consisting of the OAC resonator and the photodetector will be referred to as OAC detector.

To make efficient use of the enhanced shot noise limited sensitivity of the OAC detector, it is essential avoid the introduction of additional power fluctuations imposed by the OAC resonator. However different coupling mechanisms exist, which can produce excess power noise in reflection of an optical resonator. Noise, which is generated by the OAC resonator, is a new category of sensor noise, which will be referred to as OAC sensor noise throughout this thesis.

A short discussion of the major OAC sensor noise sources found in earlier experiments will be presented in the following section. The model of laser frequency noise coupling into power noise in reflection of the OAC resonator, presented in [22, 64], will be extended in section 3.5.1 to include the effects of imperfect mode matching and allow for arbitrary impedance matchings. The influence of mode fluctuations is discussed in section 3.5.2, while resonator internal scattering is shortly reviewed in Section 3.5.3

### 3.5.1 Frequency noise

The laser frequency is stabilized to the resonator resonance frequency. However, small frequency deviations will remain due to sensor noise and the limited noise suppression of a feedback control loop.

These remaining frequency fluctuations are converted by the resonator into power fluctuations, depending on the average frequency offset  $\Delta f$  with respect to the resonance frequency [22, 64]. In the rotating frame, introduced in section 2.3, a frequency modulation  $F = -m_F \sin(2\pi ft)$ , at frequency  $f$  with a modulation coefficient  $m_F$ , can be approximated as a phase modulation with modulation coefficient  $m = m_F/f$ , for small modulations  $m_F$  [34, 65]:

### 3 Optical AC coupling

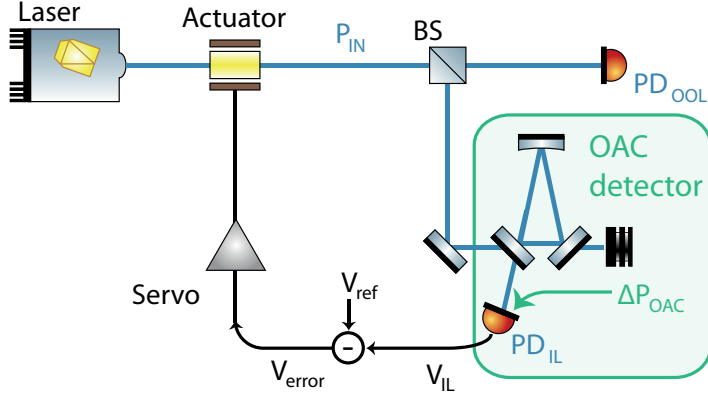


**Figure 3.5:** In an OAC based power stabilization scheme, the OAC detector, comprised by a photodetector and the OAC resonator, is used as the in-loop detector of the active control scheme. OAC sensor noise can couple into the system, whenever additional power noise is created by the OAC resonator

$$\mathbf{U}_{in}(f) = (\mathbf{U}_0 + \mathbf{U}_1) \exp(i m \cos(2\pi f t)) \quad (3.34)$$

which can be expanded with Bessel function up to first order:

$$\mathbf{U}_{in}(f) \approx (\mathbf{U}_0 + \mathbf{U}_1) \left( 1 + i \frac{m}{2} e^{i2\pi f t} + i \frac{m}{2} e^{-i2\pi f t} \right) \quad (3.35)$$

where  $\mathbf{U}_0$  and  $\mathbf{U}_1$  again represent the resonant and non-resonant mode content introduced in Section 3.2. Since the non-resonant mode content does not enter the resonator, the resonator internal field  $\mathbf{U}_{cav}$  is given by:

$$\mathbf{U}_{cav}(f) \approx \frac{r-a}{t} \mathbf{U}_0 \left( h(\Delta f) + h(f + \Delta f) i \frac{m}{2} e^{i2\pi f t} + h(-f + \Delta f) i \frac{m}{2} e^{-i2\pi f t} \right) \quad (3.36)$$

The reflected field  $\mathbf{U}_{refl}$  can be denoted as :

$$\begin{aligned} \mathbf{U}_{refl}(f) &= r \cdot \mathbf{U}_{in} - t \cdot \mathbf{U}_{cav} \\ &= r \cdot (\mathbf{U}_0 + \mathbf{U}_1) \cdot \left( 1 + i \frac{m}{2} e^{i2\pi f t} + i \frac{m}{2} e^{-i2\pi f t} \right) \\ &\quad - (r-a) \cdot \mathbf{U}_0 \left( h(\Delta f) + h(f + \Delta f) i \frac{m}{2} e^{i2\pi f t} + h(-f + \Delta f) i \frac{m}{2} e^{-i2\pi f t} \right) \end{aligned} \quad (3.37)$$

For small offset  $\Delta f \ll f_0$  the approximations

$$h(\Delta f) = \frac{1}{1 + i\Delta f/f_0} \approx 1 - i\frac{\Delta f}{f_0} \quad (3.38)$$

$$h(\Delta f + f) = h(f) - |h(f)|^2 \cdot i\frac{\Delta f}{f_0} \quad (3.39)$$

can be used to rewrite equation 3.37, for  $r \approx 1$ :

$$\begin{aligned} U_{\text{refl}}(f) = & U_1 \cdot (1 + i\frac{m}{2}e^{i2\pi ft} + i\frac{m}{2}e^{-i2\pi ft}) \quad (3.40) \\ & + U_0 \left[ \left(1 - (1 - a)\left(1 - i\frac{\Delta f}{f_0}\right)\right) \right. \\ & \quad + \left(1 - (1 - a)h(\Delta f + f)\right) i\frac{m}{2}e^{i2\pi ft} \\ & \quad \left. + \left(1 - (1 - a)h(\Delta f - f)\right) i\frac{m}{2}e^{-i2\pi ft} \right] \end{aligned}$$

To estimate the relative power fluctuations, which are produced by the conversion from frequency modulation, the power  $P_{\text{refl}}$  needs to be calculated.

$$\begin{aligned} P_{\text{refl}}(f) = & U_1^2 + U_0^2 \left( a^2 + (1 - a)^2 \left( \frac{\Delta f}{f_0} \right)^2 \right) \quad (3.41) \\ & + U_0^2 (1 - a) \frac{\Delta f}{f_0} \left[ 1 - (1 - a)h(f) - a|h(f)|^2 \right] m e^{i2\pi ft} \\ & + U_0^2 (1 - a) \frac{\Delta f}{f_0} \left[ 1 - (1 - a)h(-f) - a|h(-f)|^2 \right] m e^{-i2\pi ft} \end{aligned}$$

The complex sideband coefficients  $C_F(f)$  and  $C_F(-f)$  are defined as:

$$\begin{aligned} C_F(f, a) &= 1 - (1 - a)h(f) - a|h(f)|^2 \quad (3.42) \\ C_F(-f, a) &= 1 - (1 - a)h(-f) - a|h(-f)|^2 \end{aligned}$$

It is straightforward to show  $|C_F(f, a)| = |C_F(-f, a)|$  and  $\text{Arg}[C_F(f, a)] = -\text{Arg}[C_F(-f, a)]$ , which allows  $P_{\text{refl}}$  to be simplified:

$$\begin{aligned} P_{\text{refl}}(f) = & U_1^2 + U_0^2 \left( a^2 + (1 - a)^2 \left( \frac{\Delta f}{f_0} \right)^2 \right) \quad (3.43) \\ & + U_0^2 (1 - a) \frac{\Delta f}{f_0} 2m |C_F(f, a)| \cos(2\pi t + \text{Arg}[C_F(f, a)]) \end{aligned}$$

### 3 Optical AC coupling

---

Analogous to the derivation of the OAC transfer function the AC components,  $P_{\text{refl,AC}}$  have to be normalized with the DC components  $P_{\text{refl,DC}}$

$$|\text{RP}_{\text{refl}}(f)| = \frac{2m(1-p)(1-a)\frac{\Delta f}{f_0}|C_F(f, a)|}{p + (1-p)\left(a^2 + (1-a)^2\left(\frac{\Delta f}{f_0}\right)^2\right)} \quad (3.44)$$

$$(3.45)$$

The transfer function from frequency modulation  $F$  to relative power fluctuation in reflection of the resonator  $\text{RP}_{\text{refl}}$  is found as:

$$N_F(f) = \frac{|\text{RP}_{\text{refl}}|}{m_F} = \frac{|\text{RP}_{\text{refl}}|}{m \cdot f} \quad (3.46)$$

Conversion of frequency noise into power noise can therefore be reduced by either minimizing the offset of the frequency stabilization feedback control loop, or by reducing the remaining frequency noise between laser and resonator with a high bandwidth control loop.

#### Effect on the out of loop performance

If the OAC sensor is used in a power stabilization feedback control loop, the out of loop noise power noise  $N_{F,\text{ool}}$ , created by the frequency noise conversion has to be calculated with respect to the specific stabilization scheme and the OAC transfer function  $G_{\text{OAC}}$ <sup>2</sup> For the topology used in this thesis  $N_{F,\text{ool}}$  is given by:

$$N_{F,\text{ool}}(f) = \frac{N_F(f)}{G_{\text{OAC}}(f)} \quad (3.47)$$

The transfer function  $N_F(f, p, a, \Delta f)$  and the  $G_{\text{OAC}}(f, a, p)$  both depend on the mode matching coefficient  $p$  and the impedance matching  $a$ .

As demonstrated in Section 3.3 for every possible mode matching coefficient  $p_i$  an optimal impedance matching  $a^+$  can be found to maximize the OAC gain factor  $g$ . It turns out that this optimization is not optimal with respect to the coupling of frequency noise into out of loop power noise of the OAC based control loop  $N_{F,\text{ool}}(f, p, a, \Delta f)$ .

---

<sup>2</sup>For an overview of the different OAC power stabilization topologies, the reader is kindly referred to [21, 22].

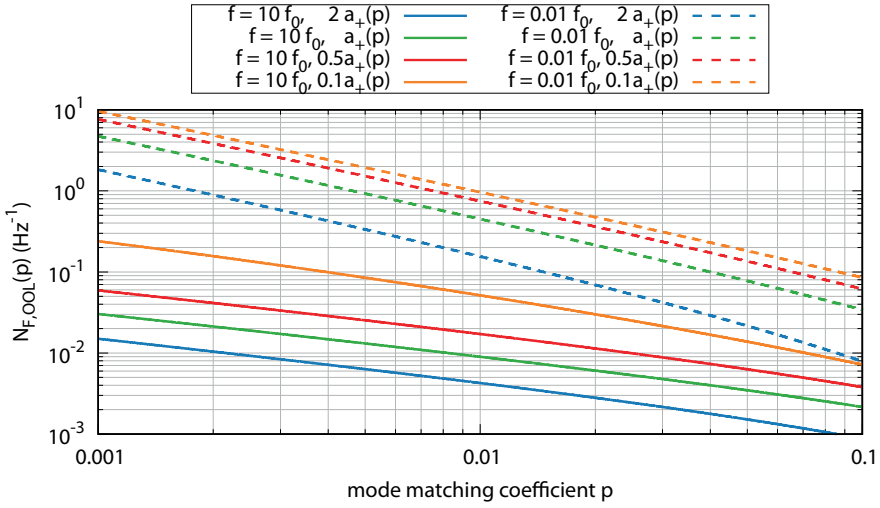


**Figure 3.6:** Out of loop frequency noise conversion for a fixed frequency offset  $\Delta f = 0.005f_0$ , at two different frequencies  $f = 10f_0$  (solid) and  $f = 0.01f_0$  (dashed).

This can be illustrated by looking at  $N_{F,ool}(f, p, a, \Delta f)$  for different sets of fixed parameters ( $f_i, a_i, \Delta f_i$ ), see Figure 3.6).

The frequency offset for each plot is chosen as  $\Delta f = 0.005f_0$ , while solid lines are for fixed frequency  $f_1 = 10f_0$ , dashed lines are for  $f_2 = 0.01f_0$ . The most important difference between the curves is found in the impedance matchings, which are chosen to be ratios of the optimized impedance matching  $a^+$ . The curve for impedance matching  $a^+$  therefore represents the OOL conversion for an optimized impedance matching, while other values indicate that the OAC gain would not be maximized for the specific mode matching coefficient  $p$ .

For both frequencies the coupling increases with smaller impedance matching values. This means operating at an impedance matching smaller than the optimized value  $a^+$  not only results in less OAC gain, but also increases the noise coupling. However, working at larger impedance matching values than  $a^+$  can be beneficial if the out of loop performance is limited by this conversion effect.

### 3.5.2 Mode fluctuations

If power from the fundamental mode is transferred to another laser mode, this is referred to as mode fluctuation. A potential candidate

### 3 Optical AC coupling

---

for mode fluctuations like this is beam pointing, which can reduce the power coupled into the resonator. Another example are polarization fluctuations of the incoming beam, which would also reduce the optical power coupled into the resonator<sup>3</sup>. Finally varying modulation strength of imprinted RF-modulations can would induce a power transfer between carrier and sidebands.

Generally these kind of coupling can be described by an input field as:

$$U_{\text{in}}(f) = U_0(1 - m \frac{|U_1|}{|U_0|} \cos(2\pi ft)) + U_1(1 + m \cos(2\pi ft)) \quad (3.48)$$

The transfer function  $N_M(f)$  of mode fluctuations to relative power noise in reflection of the resonator, was derived for small modulations  $m$  and high Finesse resonators ( $r \approx 1$ ) in [22] to:

$$N_M(f) = \frac{p}{a^2(1-p) + p} \quad [N_M(f)] = 1. \quad (3.49)$$

The relative out of loop power noise imprinted by this sensing noise source is found analog to Section 3.5.1:

$$N_{M,\text{ool}}(f) = \frac{N_M(f)}{G_{\text{OAC}}(f)} \quad [N_M(f)] = 1. \quad (3.50)$$

#### 3.5.3 Resonator internal scattering

Resonator-internal scattering processes have been found to be one of the major noise sources in previous Optical AC coupling experiments. A numerical time domain model with multiple optical modes was developed to describe the observed effects [22].

Scattering can couple only to resonant modes of the optical resonator. This can be either higher order spatial modes or, in the case of three mirror resonators, the counter-circulating fundamental mode [66]. Scattering into higher order spatial modes can be suppressed with a resonator internal aperture which introduces higher losses for these modes than for the fundamental mode, because they are spatially wider extended (see Section 4.1). However, scattering into the counter-circulating fundamental mode can not be prohibited with a resonator internal aperture.

The cause of the resonator internal scattering processes could not be

---

<sup>3</sup>providing the fundamental polarization eigenmodes of the resonator are not de-generated

clarified, but was attributed to outgassing processes inside the vessel of the OAC resonator.

## 3.6 Summary

In this chapter the basic idea of Optical AC coupling was introduced and an analytic OAC transfer function was derived for perfect and imperfect mode matching coefficients.

The dependence of the OAC gain factor  $g(\alpha, p)$  from the impedance matching  $\alpha$  and mode matching  $p$ , was investigated for imperfectly mode matched resonators. An optimal positive and negative impedance matching can be estimated for a given mode matching coefficient  $p$  with the equations derived in Section 3.3. Furthermore, it was demonstrated how to estimate the impedance matching  $\alpha$  and the mode matching coefficient  $p$  from an independent measurement of the DC-reduction  $\zeta$  and the OAC gain factor  $g$  in Section 3.4. These findings were used for the analysis of the measurements performed at aLIGO and GEO 600 (see Chapter 5).

Potential OAC sensor noise sources were discussed and the frequency noise conversion was extended for imperfect mode matchings. A closer investigation of the out of loop noise, caused by frequency noise conversion, indicates that it is possible to trade OAC gain against frequency noise conversion.

Especially the resonator internal scattering into the counter circulating resonator fundamental mode, which was observed in earlier OAC experiments, was a decisive factor for the resonator design described in the next chapter.





# 4

## Chapter 4

# OAC with a narrow linewidth resonator

This chapter describes a dedicated experiment performed at the AEI in Hannover to investigate OAC at frequencies between 300 Hz and 100 kHz, significantly lower than what has been covered previously.

Section 4.1 presents the design of the core component of the experiment: the OAC resonator with a narrow linewidth below  $\nu_{LW} = 4$  kHz and a tunable impedance matching [58].

Section 4.2 introduces the full experimental setup including the optical components, as well as the electronic feedback control loops necessary for the operation of the experiment.

Experimental challenges and the methods used to overcome these are described in Section 4.3.

In Section 4.4 the main results, consisting of OAC transfer function measurements and the power stabilization experiments are presented. The chapter closes with a discussion (Section 4.5) of the results including a comparison to the performance of earlier OAC experiments, and a brief outlook on possible next steps in Section 4.6.

## 4.1 Resonator Design

The resonator used for the OAC experiment was designed with a focus on the avoidance of noise sources found in previous OAC experiments [22, 58].

Scattering into the counter-circulating fundamental and higher order spatial modes was found to be a major limiting noise contribution, in

## 4 OAC with a narrow linewidth resonator

---

previously used ring resonators. Hence, a linear resonator design was chosen for the new experiment, because a counter-circulating mode does not exist and therefore can not be excited by scattered light.

The resonator is constructed from several aluminum parts, see Figure 4.1, which are fixed together by steel screws.

The spacer is an almost 1 m long rectangular tube, formed by an aluminum u-profile with a matched top plate.

The resonator mirrors are clamped between two aluminum plates, referred to as the outer and inner clamping plates, which are then fixed on the rectangular aluminum spacer to form the linear OAC resonator. An additional viton ring between the outer plate and the mirror substrate is used to distribute the pressure applied by the clamping plates evenly onto the mirror substrate and prevents stress induced damage to the mirrors during the clamping process.

The distance between the mirror surfaces on the inside of the resonator  $L$  is designed to be 1 m. This is the result of a trade-off between narrow linewidth and the space constraints of the experiment.

A mechanism to change the impedance matching of the OAC resonator had to be implemented, since it is a crucial tuning parameter, to achieve a maximum OAC gain factor in the experiment. This is even more important for an experiment with imperfect mode matching, as described in Section 3.3.

A motorized iris aperture (*Type: Owis IBM 65*) was mounted in a dedicated mount and clamped onto an XZ-Linear stage (*Type: Newport 9063-XZ-M-Gothic-Arch XZ translation stage*) which again was fixed on the resonator spacer (see Figure 4.2).

The assembled resonator spacer is clamped into a specially designed mount (see Figure 4.2, right) which supports the spacer over the full length of the resonator for better mechanical stability<sup>1</sup>.

The clamping plates, used to clamp the spacer onto its mount, are L-shaped and provide the possibility to attach two additional alignment mirrors to the in-coupling and the out-coupling port of the resonator<sup>2</sup>.

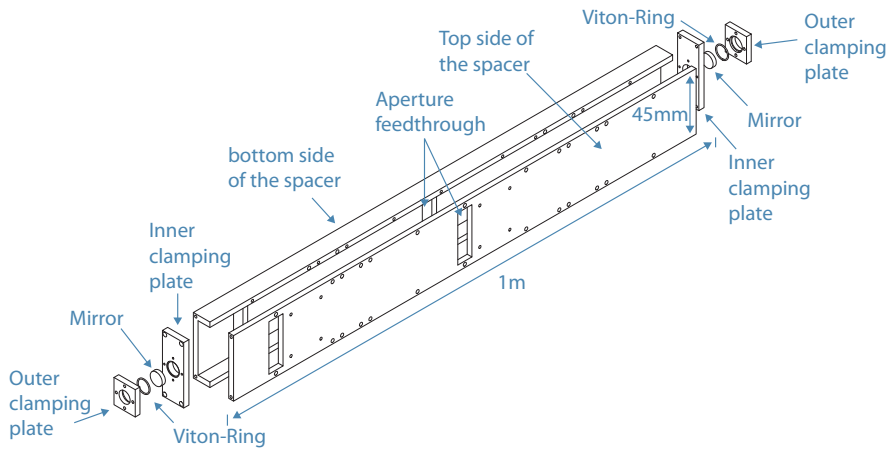


**Figure 4.1:** OAC resonator spacer assembly: The OAC resonator consists of an u-shaped aluminum bottom spacer and a top side with the same dimensions, which are screwed together with stainless steel screws. The mirrors are clamped between an inner and outer clamping plate with an additional viton ring placed between the outer clamping plate and the mirror. Stainless steel screws are used to fix the clamping plates to each other and fix them on the resonator-spacer.

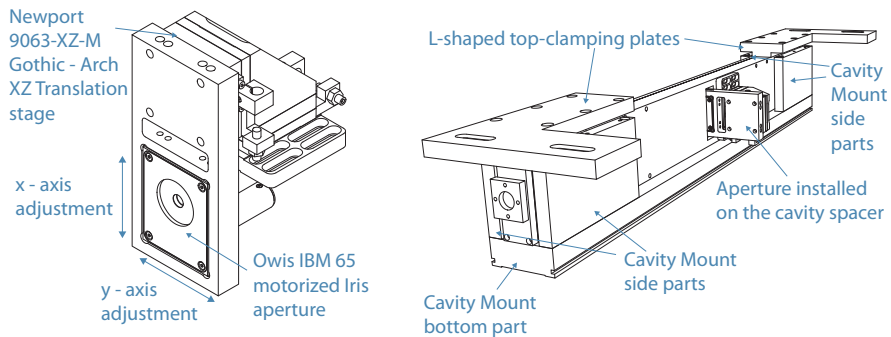


**Figure 4.2:** Left: Motorized iris aperture inside an aluminum mount, which is screwed to the Newport translation stage. The translation stage is later on used to adjust the center of the iris aperture with respect to the cavity fundamental mode's x- and y- coordinates. Right: OAC resonator in its mount: The spacer is clamped between the bottom part of the mount and the L-shaped top clamping plates. The aperture is inserted through the feed-through holes in the spacer and its alignment stage is fixed with screws on the spacer

## 4 OAC with a narrow linewidth resonator

---

**Table 4.1:** Calculated Finesse and corner frequency  $f_0$  of the resonator for different resonator internal losses. In the impedance matched condition, the corner frequency of the resonator is  $f_0 = 1623\text{Hz}$

$\delta_0$ [ppm]	$\delta_1$ [ppm]	$\delta_2$ [ppm]	Finesse $\mathcal{F}$	$f_0$ [Hz]
0	68	2	89760	835
30	68	2	62832	1193
66	68	2	46200	1623
96	68	2	37850	1980

### 4.1.1 Linewidth and impedance matching

The linewidth of the resonator depends on two parameters, the length of resonator  $L$  and the Finesse  $\mathcal{F}$ , which is a measure for the sum of the losses inside the resonator.

According to equation 2.17 and equation 2.34 the corner frequency  $f_0$  is calculated by:

$$f_0 = \frac{v_{LW}}{2} = \frac{c}{2L} \frac{\delta_2 + \delta_0 + \delta_1}{4\pi}, \quad (4.1)$$

To achieve a narrow linewidth the resonator should be as long as possible, the mirror reflectivities as high as possible and the resonator internal losses as small as possible.

Due to space constraints, the resonator length  $L$  was chosen to be 1 m and the mirror transmissivities were chosen to be  $\delta_1 = 68 \cdot 10^{-6}$  for the in-coupling mirror and  $\delta_2 = 2 \cdot 10^{-6}$  for the out-coupling mirror. This choice ensured a narrow linewidth of the resonator and provided a loss budget for resonator internal losses which can occur due to scattering, absorption in the mirror coatings or by aperture effects of the 2.54 cm diameter mirrors.

In previous experiments the initial internal losses  $\delta_{0i}$  were measured after the first assembly of the resonator and found to be  $\delta_{0i} = 22\text{ppm}$ . The initial impedance matching  $a_i$  can therefore be determined with equation 2.40 to  $a_{ini} = a(\delta_{0i}, \delta_1, \delta_2) \approx -0.432$

To provide the possibility to adjust the impedance matching of the

---

<sup>1</sup>In earlier experiments [58] the spacer was supported by two separate mounts which led to the excitation of mechanical modes of the spacer assembly.

<sup>2</sup>Due to the tight space constraints in the vacuum tank, the alignment-mirrors for the the incoming and outgoing laser beam had to be placed outside of the suspended platform (see Section 4.2).

resonator, a motorized iris aperture is used (see Section 4.1). With this aperture additional internal losses can be introduced in intervals of a few ppm. This allows the impedance matching of the resonator to be changed from the over-coupled to an under-coupled situation. [58].

Table 4.1 compares the design values of the optical resonator for different resonator internal losses [58].

### 4.1.2 Higher order mode suppression

A noise source similar to the scattering into the counter-circulating mode of the resonator described earlier is scattering into resonant higher order spatial modes, which can become a limiting noise source in OAC experiments [22].

To avoid scattering into higher order HG modes the resonator was designed in such a way as to suppress HG modes with small mode index. The resonator length  $L$  as well as the mirror curvature radii  $r_1$  and  $r_2$  define the cavity  $g$ -parameters<sup>3</sup>,  $g_1$  and  $g_2$ , a measure for the stability of an optical resonator according to:

$$g_1 = 1 - \frac{L}{r_1} \tag{4.2}$$

$$g_2 = 1 - \frac{L}{r_2} \tag{4.3}$$

The mirrors in the resonator had identical radii of curvature with  $r_1 = r_2 = 300$  cm and therefore  $g_1 = g_2 = 2/3$ . The  $g$ -parameters can be used to calculate the mode spacing  $\nu_{nm}$  of a higher order spatial mode compared to the corresponding fundamental mode resonance frequency of the optical resonator as:

$$\nu_{nm} = \nu_{qnm} - \nu_q = (n + m + 1) \frac{\arccos(g_1 g_2)}{\pi} \frac{c}{2L} \tag{4.4}$$

with  $\nu_{qnm}$  being the absolute resonance frequency of the specific HG mode and  $n, m$  being the index of the mode (see equation 2.5).

Table 4.2 shows the mode separation of the HG modes with  $n + m = 1$

<sup>3</sup>Not to be confused with the OAC gain factor  $g$ .

#### 4 OAC with a narrow linewidth resonator

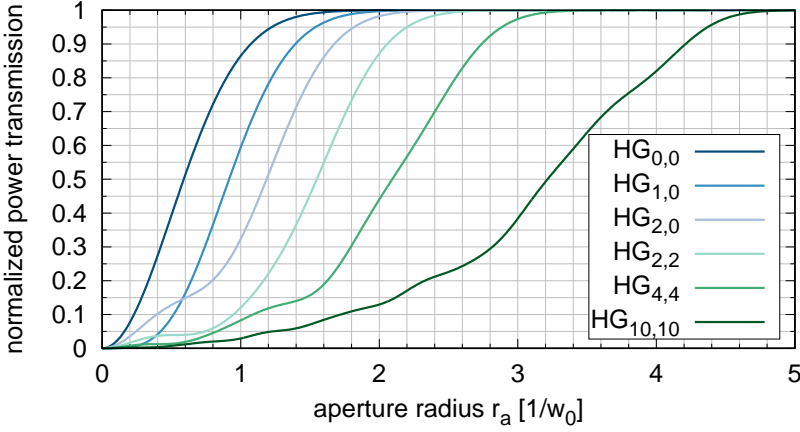


**Figure 4.3:** Power transmission through a circular aperture for different Hermite Gaussian modes. The wave-like structures of the different curves appear whenever the aperture radius reaches a local intensity maximum.

and the three modes with the closest resonance frequency to the next fundamental mode up to a mode index of  $m + n = 40$ .

The aperture, which is used to regulate the impedance matching, can simultaneously be used to suppress the excitation of these higher order modes. Since the higher order HG modes are significantly larger in their spatial extent, the losses introduced by a circular aperture are significantly higher for these modes than for the fundamental mode of the resonator.

The field of a higher order HG mode at the position of the beam waist  $w_0$  ( $z = 0$ ) can be calculated according to:

$$U_{nm}(x, y) = \sqrt{\frac{\pi}{2} \cdot \frac{1}{2^n n! w_0} \cdot \frac{1}{2^m m! w_0}} H_n \left( \frac{\sqrt{2}x}{w_0} \right) H_m \left( \frac{\sqrt{2}y}{w_0} \right) \exp\left(-\frac{x^2 + y^2}{w_0^2}\right) \quad (4.5)$$

The normalized intensity transmitted through a circular aperture with radius  $r_a$ , which is centered on the beam axis, can be calculated in Cartesian coordinates for a single quadrant and then scaled by a factor of 4:

$$I_{ap}(r_a) = 4 \int_0^{r_a} \int_0^{\sqrt{r_a^2 - x^2}} U_{nm} U_{nm}^* dx dy \quad (4.6)$$

Accordingly the losses induced by the aperture are given by:

$$\delta_{\text{aperture}}(r_a) = 1 - I_{\text{ap}}(r_a) \quad (4.7)$$

In Figure 4.3 the relative power transmission of different higher order HG modes are compared to the fundamental mode.

Note how the HG<sub>2,0</sub>, despite its higher mode index  $n + m$ , suffers less optical losses than the HG<sub>1,0</sub> for small aperture openings. This is due to its intensity maximum on the beam axis ( $r_a = 0$ ).

Using a circular aperture inside the resonator can change the beam properties of Gaussian beam which is transmitted through it due to diffraction effects [67].

If the aperture has a radius  $r_a$  with  $1.6 r_0 < r_a < 3 r_0$  the beam is weakly diffracted<sup>4</sup>. In this case the beam still looks like a Gaussian beam, but will have slightly different characteristics. However, in this experiment this effect can be neglected, since the aperture is used to imprint relative power losses of up to 150 ppm and therefore the radius of the aperture is never significantly smaller than  $3 r_0$ .

---

<sup>4</sup>Here,  $r_0$  is the  $1/e$  intensity radius which is related to the  $1/e$  field radius  $w_0$ , defined in [68] by  $r_0 = w_0/\sqrt{2}$ . The  $1/e$  field radius will be referred to as the beam waist, as it marks the  $1/e^2$  intensity radius.

### 4.2 Experimental Setup

In an initial setup the OAC resonator was placed on a vibration-isolation optical table in one of the standard optical laboratories of the AEI.

While it was possible to set up and test the high bandwidth frequency stabilization feedback control loop, see section 4.2.1, this environment turned out to be unsuited for the final power stabilization experiments since acoustic disturbances could not be shielded well enough and prevented a stable operation of the OAC resonator.

To shield the crucial components of the experiment from acoustics they needed to be migrated into a spare GEO 600 vacuum tank, which was large enough to host the 1 m long resonator, as well as optical components necessary for the OAC coupled power noise detection.

To provide seismic isolation the complete vacuum tank is mounted on a active seismic isolation platform type *Halcyonics, MOD-Sandwich 1050*. This isolation platform can provide up to 20 dB noise suppression between 2 Hz and 200 Hz [69].

An aluminum platform with 80 cm diameter is suspended within the tank on three 1 m long steel wires to additionally isolate the experiment from seismic vibrations.

To reduce the amount of optical components inside the vacuum tank the experiment was split into two locations (see Figure 4.5).

The *Innolight Mephisto* NPRO 2 W1064 nm laser was placed on the so called laser preparation breadboard outside of the vacuum tank. Downstream of the NPRO the beam propagated through a half wave and quarter wave plate before it was transmitted through a Faraday isolator. This wave plate-PBS combination is used to linearize the polarization, which is sent through the FI.

The beam was sent through a resonant EOM to imprint phase modulation sidebands at 29.02 MHz. In a next step, a half wave plate

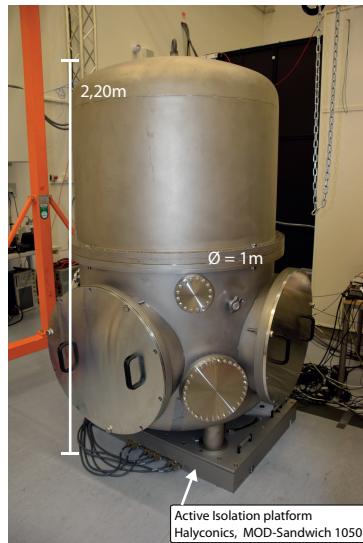


**Figure 4.4:** Photograph of the spare GEO 600 tank, which is mounted onto the Halcyonics active isolation platform



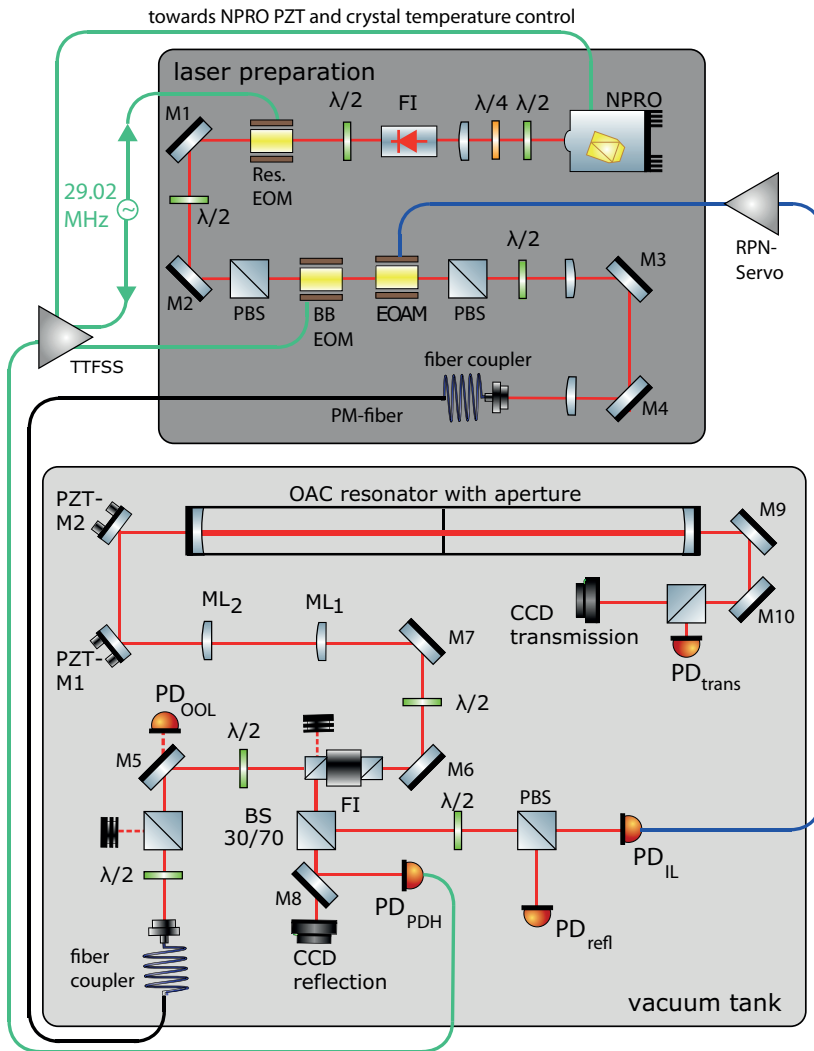


**Figure 4.5:** Sketch of the experimental setup: The full experimental setup is divided into two different locations, the laser preparation breadboard on an optical table and the detection bench inside the vacuum tank.  $PD_{PDH}$  is connected with the TTFSS servo (green trace), which in turn is connected to the different actuators used for the frequency stabilization feedback control loop. Similarly,  $PD_{IL}$  is connected to the RPN-Servo and the EOM (blue) to form the power stabilization feedback control loop.

## 4 OAC with a narrow linewidth resonator

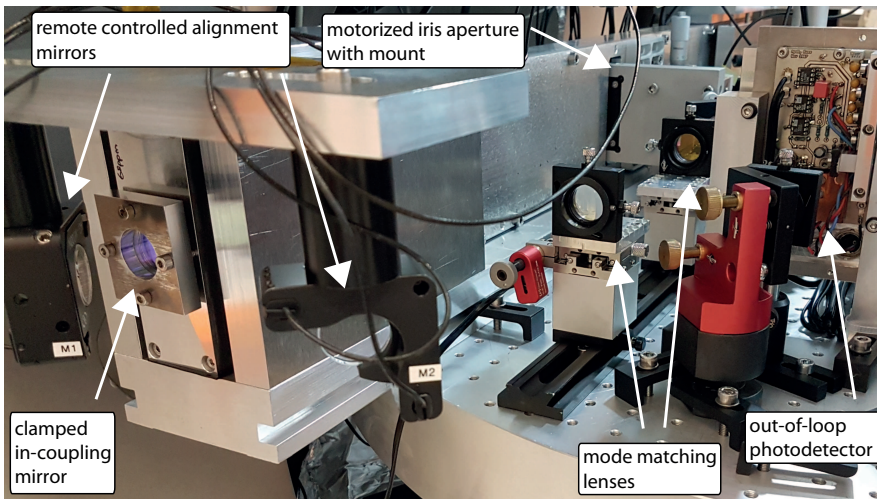


**Figure 4.6:** Photograph of the remote controlled alignment mirrors hanging down from the L-shaped clamping plates used to fix the OAC resonator spacer onto its mount. The picture also shows the mode matching lenses and  $PD_{OOL}$ .

and a PBS were used to align the polarization axis to the following broadband electro optical modulator (EOM) and minimize its residual amplitude modulation (see also Section 4.3.1).

The beam was then sent through an electro optical amplitude modulator (EOAM) followed by yet another PBS for converting the polarization shift induced by the EOAM into an actual amplitude modulation. A single mode polarization maintaining (PM) fiber with an integrated vacuum feedthrough from *Schäfter+Kirchhoff* was used to couple the light from the laser preparation breadboard to the inside of the vacuum tank, which is shown in Figure 4.2. Therefore, the polarization of the light had to be adjusted with an additional half wave plate before the beam was coupled into the fiber coupler.

A similar fiber coupler was placed on the suspended platform inside the vacuum tank and the light was additionally polarization-filtered by a combination of half wave plate and PBS.

The partly transmissive mirror M5 ( $T=10\%$ ) was used to monitor the power noise of the beam entering the vacuum tank with the out-of-loop detector  $PD_{OOL}$ .

The beam is then transmitted through a half wave plate and a Faraday isolator. The half wave plate and the first PBS of the FI were used as a power attenuation stage to control the power incident to the OAC resonator.

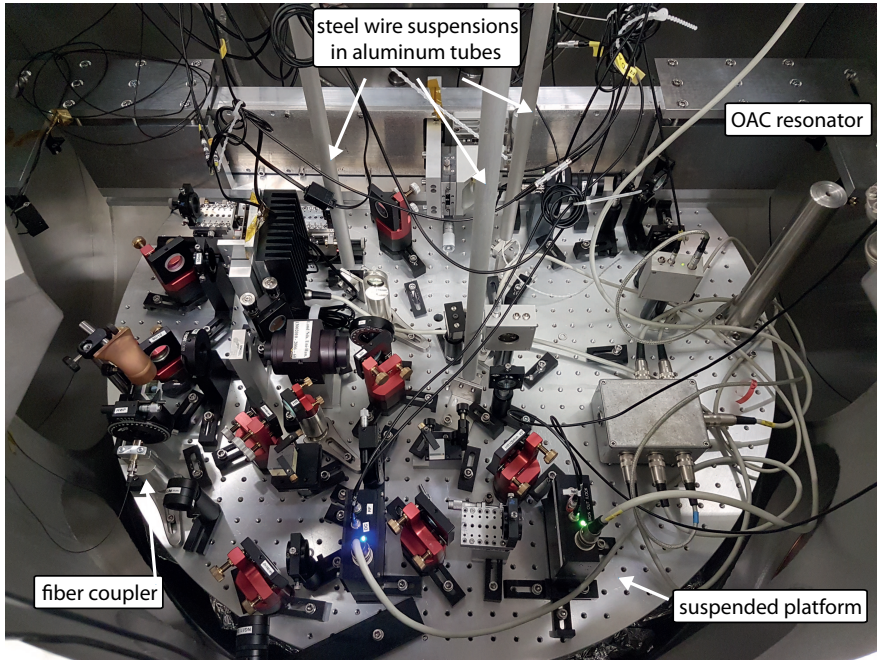


**Figure 4.7:** Photograph of the experimental setup inside the vacuum tank. The optical components are fixed on the platform which is suspended by three steel wires. The OAC resonator is larger than the platform and therefore protrudes over the edge.

## 4 OAC with a narrow linewidth resonator

---

Downstream of the FI three lenses were used to mode match the beam to the resonator fundamental mode. A set of remote controllable mirror mounts was installed for the alignment of the beam to the cavity axis.

Since the spacer had to be placed on the outer region of the platform to provide enough space for all the optical components, the mounts were fixed on the L-shaped clamping plates described in Section 4.1 hanging upside down in the free space outside of the platform, see Figure 4.2.

The beam reflected by the OAC resonator follows the beam path back towards the FI and gets reflected towards the detection beam path by the PBS of the FI.

A 30/70 beam splitter was used to direct the major portion of the reflected beam towards the Pound-Drever-Hall-PD ( $PD_{PDH}$ ), which was used for the frequency stabilization between laser and OAC resonator length.

With a CCD camera behind mirror M8 the beam profile in reflection could be monitored directly.

The beam reflected by the 30/70 beam splitter was used for the in-loop detector  $PD_{IL}$  of the power stabilization experiments.

The power level in reflection of the OAC resonator depends on various parameters:

- The mode matching coefficient  $p$
- The impedance matching  $\alpha$
- The power coupled through the fiber
- Locked or unlocked OAC resonator

Therefore, an additional half wave plate PBS combination was used to adjust the power level on the in-loop sensor for the various parameter combinations of the experiment.

The second port of the PBS could then be used to measure the power reduction  $\zeta$  in reflection of the resonator (see Section 3.4).

In transmission of the OAC resonator the light was directed back to the suspended platform with two mirrors, again installed upside down from the clamping plate.

The power noise of the beam transmitted by the resonator was then measured with the transmission PD (TPD), while another CCD camera placed in transmission of mirror M12 was used to monitor the

transmitted beam profile.

### 4.2.1 Frequency stabilization

To use the OAC technique the frequency of the laser light has to be stabilized to the length of the OAC resonator. Therefore, a feedback control loop with a unity gain frequency of 600 kHz was installed.

The core of the feedback control loop is an aLIGO style servo, referred to as the table top frequency stabilization servo (TTFSS)[70], which is used at the aLIGO detectors[11], the aLIGO PSL reference system [71] and the 10m prototype experiment [72, 73] in Hannover. In contrast to these experiments, which control the TTFSS via a digital interface, the TTFSS is controlled with an analog interface.

Three different actuators are used to achieve a high unity gain frequency with sufficient dynamical range (see Figure 4.5). The NPRO includes two actuators, a peltier element to control the laser crystal temperature and a piezo electric transducer (PZT), which is attached to the laser crystal and can be used to change the optical path length in the crystal. Both of the NPRO actuators are used for low frequency feedback up to 10 kHz. The peltier, with a modulation coefficient of  $2.8 \frac{\text{GHz}}{\text{V}}$ , has enough range to compensate long term drifts of the laser frequency, while the PZT is fast enough to control frequency noise in the audio band. Due to mechanical resonances of the PZT, the feedback at high frequencies is provided by an additional broadband EOM placed at the laser preparation breadboard.

The error signal, necessary for locking the laser frequency to the resonator length, is created using the Pound-Drever-Hall method [56, 74]. Phase modulation sidebands at 29 MHz are imprinted with a resonant EOM on the laser preparation breadboard and the light is detected in reflection of the OAC resonator with a dedicated resonant photodetector, called  $\text{PD}_{\text{PDH}}$ . The signal detected by  $\text{PD}_{\text{PDH}}$  is then demodulated with the correctly phase shifted local oscillator which is used to imprint the phase modulation sidebands, to create the error signal.

The strength of the phase modulation has to be chosen carefully since the low linewidth resonator strongly converts incoming phase modulation into power modulation in its reflection. This can cause slew-rate [75] related problems in the fast photodetector used for the power stabilization feedback control loop. This effect was observed to limit the out-of-loop performance of the OAC power stabilization experiment.

## 4 OAC with a narrow linewidth resonator

---

The strong RF-amplitude modulation, which originated in the conversion from the RF-phase modulation, could not be handled by the transimpedance amplifier of the power stabilization feedback control loop sensor, which then resulted in a white noise floor of the stabilized out-of-loop performance. After a significant reduction of the phase modulation, this effect vanished.

To achieve enough optical gain for the frequency stabilization while having small phase modulation sidebands, the  $PD_{PDH}$  needed to detect a high amount of DC power. For this reason this photodiode was saturated in the unlocked case. When the laser frequency becomes resonant the DC power drops until the photodiode is not saturated anymore and can be used for stabilization. Hence, optical frequency range for which lock acquisition is possible depends on the total optical power on the photodiode and the DC reduction  $\zeta$ .

The lock was achieved by using the NPRO crystal temperature to manually adjust the laser frequency to the resonance of the resonator while the feedback control loop was closed.

### 4.2.2 Power stabilization

The power stabilization feedback control loop is comprised of the EOAM-PBS combination on the laser preparation breadboard, the in-loop photodiode  $PD_{in}$ , which is placed in reflection of the OAC resonator and an analog servo placed outside the vacuum tank.

The sufficient longterm stability of the DC laser power allowed to use an AC coupled control loop design. Therefore, a bootstrapped photodiode design with a sufficient dark noise clearance at low frequencies and a detected photocurrent of  $i_D = 0.3 \text{ mA}$ , similar to the design described in [76] was chosen.

An open loop gain transfer function measurement of the power stabilization feedback control loop is shown in Figure 4.8.

The bandwidth of the loop was limited by servo internal offsets, causing saturation effects. When operated with OAC the loop was therefore capable of reaching a higher unity gain frequency, since the OAC transfer function becomes part of the open loop transfer function and increases the overall gain for high frequencies.

The bandwidth of the control loop allows for enough gain to suppress the free running noise to the desired noise levels. For the classical power stabilization a gain of up 36 dB was reached. For OAC based power stabilization feedback control loop, the open loop gain was fur-

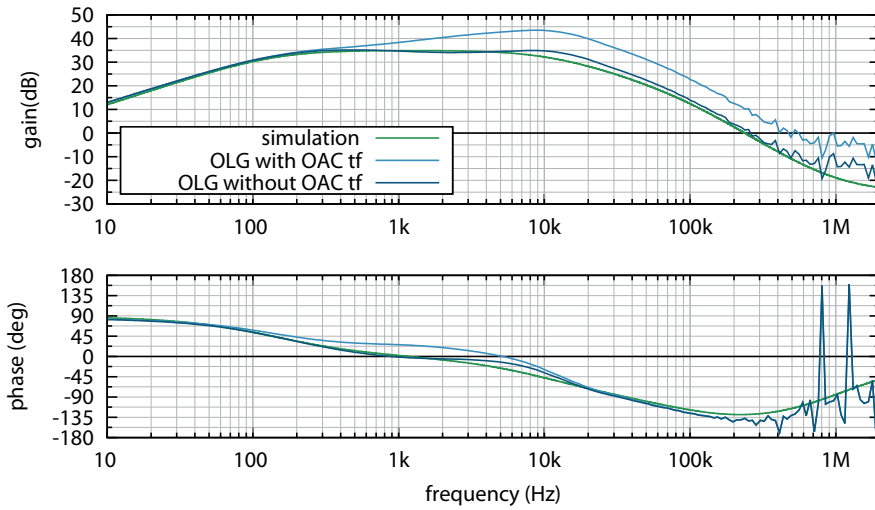


**Figure 4.8:** Power stabilization feedback control loop gain: The OLG of the power stabilization feedback control loop is altered by the Optical AC coupling transfer function, allowing for more gain and a higher unity gain frequency than the classical feedback control loop. For comparison, a simulation of the classical OLG, consisting of the transfer function of the servo, the EOAM and the photodiode, is shown together with the measured OLG. Both curves match each other if the OAC transfer function is folded out of the measurement.

ther amplified, according to the OAC transfer function.

### 4.3 Experimental challenges

This section will discuss two major problems connected to the experimental setup of the new OAC experiment and their solutions.

Residual amplitude modulation (RAM) measured on the beam transmitted through the optical fiber was observed to increase the RPN of the laser by up to two orders of magnitude. To avoid a saturation of the power stabilization feedback control loop this RAM had to be eliminated.

A second challenge was imposed by the long storage time of the OAC resonator, which prohibited the use of standard mode matching procedures and therefore limited the achievable OAC gain factor.

#### 4.3.1 Residual amplitude modulation

Residual amplitude modulation (RAM) is an unwanted side effect of EOM usage in optical experiments and has been investigated since the 1980s [77]. RAM produced by EOMs is still not understood in all its various aspects, but some insight has already been gained. EOMs can produce polarization changes if not aligned perfectly but also cavity effects between the end surfaces of the EOM crystal can lead to strongly temperature dependent RAM in transmission of the EOM [78]. Since RAM behind an EOM is temperature and intensity dependent it is also associated with the so called photorefractive effect within the crystal [79].

The broadband EOM (*Newport, Type 4004, MgO : LiNbO<sub>3</sub>*), used as actuator for the frequency stabilization feedback control loop in the original TTFSS setup, was observed to create RAM, which was detected on PD<sub>OOL</sub> inside the vacuum tank at RPN levels of  $1.0 \cdot 10^{-5} \text{ Hz}^{-1/2}$  for frequencies between 1 – 20 kHz.

The strength of the coupling between EOM drive and RAM could be

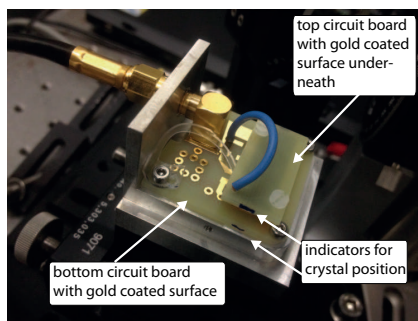


**Figure 4.9:** Temperature stabilized EOM. The crystal (not visible) is clamped between two circuit boards which are gold coated to provide the electrical surfaces necessary to apply a voltage difference between opposite sides of the crystal. The crystal position is indicated by the black markers



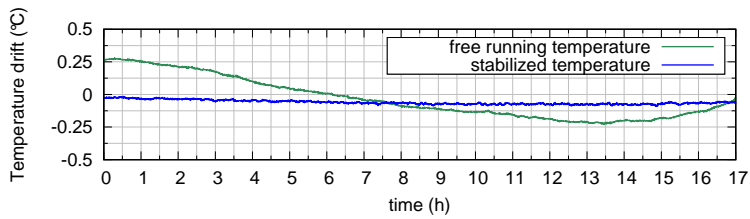


**Figure 4.10:** Out of loop temperature stability at the surface of the self build EOM crystal over a time span of 17 hours with and without enabled temperature stabilization

measured and observed over time with a simple transfer function measurement and showed a flat behavior up to frequencies of 1 MHz. The coupling could then be minimized by adjusting the alignment of the laser beam through the EOM crystal, the polarization of the incoming beam, the alignment of the laser beam to the fiber input coupler and finally, by the offset voltage applied to the EOM.

However, the optimization of these parameters usually lasted for several seconds before the coupling increased again by up to 20 dB.

To avoid saturation in the electronics of the power noise feedback control loop this noise required significant suppression.

A significant coupling strength reduction was finally achieved using a custom built temperature stabilized EOM with wedged end surfaces. The wedged end surfaces allow cavity effects to be avoided, while the temperature stabilization reduces temperature induced changes in the index of reflection of the EOM crystal. To enhance the stability of the input polarization a PBS was placed directly in front of the custom build EOM. The temperature stabilization feedback control loop was comprised by a *PT-100* sensor fixed to the inside of the EOM's aluminium housing, a dedicated temperature controller and a peltier element which was used to heat up both, the crystal and the housing of the EOM. A *PT-1000* was clamped against the EOM crystal to provide an out of loop measurement of the achieved temperature stability.

The performance of the temperature stabilization was monitored with the out-of-loop sensor *PT-1000* (see Figure 4.10), showing an improvement of at least one order of magnitude in total temperature drift at the EOM crystal over a time span of 17 hours.

### 4.3.2 Alignment and mode matching

Due to the variable impedance matching  $\alpha$  of the resonator design described in Section 4.1, the mode matching coefficient becomes the crucial parameter with respect to achieving the maximum OAC gain factor  $g$  accessible in our experiment (see Section 3.3).

The standard procedure to align a laser beam to an optical resonator is straight forward. The laser frequency or the resonator length is scanned with a frequency of approximately  $f_{\text{scan}} = 10$  Hz and the transmitted light of the resonator is measured with a photodetector and observed with an oscilloscope.

For length/frequency changes larger than a full resonator FSR all optical modes of the resonator can be observed as peaks in the transmitted power, with a width corresponding to the linewidth of the resonator. The alignment and the mode matching lenses are adjusted in such a way that only the fundamental mode of the resonator is transmitted. This method relies on the assumption that the resonator is scanned with a velocity such that the electric field in the resonator has enough time to reach its steady state amplitude. If the resonator is scanned too fast the electrical field inside the resonator acquires an oscillating component [36].

The storage time  $\tau_s$  defines the decay time of an electric field inside an optical resonator to a fraction of  $1/e$  and can be calculated according to

$$\tau_s = \frac{2FL}{\pi c} \quad (4.8)$$

For the resonator used in our experiments this results into  $\tau_s \approx 1.2$  ms. This decay can be precisely measured with a laser that is frequency stabilized to the length of the resonator and then suddenly blocked. The transmitted electrical field of the resonator resembles the cavity field decay and can be observed with a photodetector very precisely. This type of measurement is usually referred to as cavity ringdown [80].

A longer storage time  $\tau_s$  reduces the scanning speed which can be used for the alignment and mode matching process described above. It is possible to calculate a normalized length scan ratio  $v_L$ , which relates the scanning speed to the storage time of the resonator and can be used to estimate if a certain scanning velocity will result in oscillatory behavior of the resonator.

$$v_L = \frac{\dot{L}\tau_s}{(\Delta L_{\text{fwhm}}/2)} \quad (4.9)$$

For a saw tooth waveform, the length scanning velocity  $\dot{L} = \Delta L_{\text{scan}} \cdot f_{\text{scan}}$  is the product of the length change  $\Delta L_{\text{scan}}$  and the scanning frequency  $f_{\text{scan}}$ . To avoid oscillations in the amplitude of the cavity field, the scanning speed should be chosen in such manner that  $v_L \leq 1$ . To work with the usual procedure a full free spectral range  $\Delta L_{\text{FSR}}$  needs to be scanned, to allow comparison of the height of all transmission lines at the same time, while changing the alignment/-mode matching. It is also advantageous to have a sufficient scanning frequency of approximately  $f_{\text{scan}} = 10 \text{ Hz}$  to get a fast feedback about the effects of each change in alignment/mode matching.

In the case of this experiment, we can use the resonator parameters from section 4.1 and a scanning frequency  $f_{\text{scan}} = 10 \text{ Hz}$  to calculate the normalized scanning ratio. The result of  $v_L \approx 150$  predicts a highly oscillating resonator field.

This also means the resonator is far from reaching its steady state, with a high power buildup inside the resonator. Hence, the power change in transmission and reflection of the resonator is significantly smaller than for slow scanning velocities.

Since the ringing effects prohibited the use of the standard mode matching procedure a different approach was chosen. For the coarse mode matching with respect to the waist parameters, the beam parameters of the incident beam were estimated with a WinCam *Type: WinCamD-UCD23 (DataRay Inc.)*. Mode matching lenses were placed accordingly in order to match the incident beam to the calculated resonator fundamental mode.

For a coarse alignment the NPRO crystal temperature was scanned and a CCD in transmission of the OAC resonator was used to minimize the spatial extent of the transmitted beam.

After this coarse alignment and mode matching, the resonator could be locked to its fundamental mode. The remote controlled alignment mirrors were used to further improve the alignment of the beam with a locked resonator by maximizing the transmitted optical power, or respectively, minimizing the reflected power.

The disturbances induced by the remote controlled PZT alignment mirrors, hanging down from the L-shaped clamping plates, could be large enough to saturate the feedback control loop. This meant it was necessary to lock the resonator with significantly reduced optical power on  $\text{PD}_{\text{PDH}}$  which therefore reduced gain of the control loop. Again, a trade off had to be made between enough gain to be able to lock the resonator and the avoidance of saturations.

## 4 OAC with a narrow linewidth resonator

---

Even though the mode matching lenses were also placed on remote controllable linear stages, a fine tuning of the mode matching lenses, while keeping the cavity resonant, was prevented by the disturbances induced by the *Newport 8321 Picomotor actuators* used to control the lens positions. This made the adjustment of the mode matching lenses even more complicated and time consuming.

The described difficulties with respect to the scanning velocity also prevented use of the standard procedure to estimate the mode matching coefficient  $p$ , which requires to scan the resonator in the same way, as for the mode matching procedure. A lower limit for the mode matching coefficient  $p$  can be estimated from the transmitted optical power in the different Hermite Gaussian modes, compared to total transmitted power.

Instead of this standard procedure, the formalism introduced in Section 3.4 was used to deduce an upper limit for the mode matching coefficient. To achieve a Optical AC coupling gain factor  $G_{a+} \approx 9$  dB, the mode matching coefficient has to be  $p \leq 0.05$ , see Eq. 3.27.

### 4.4 Results

To characterize the OAC resonator, the OAC transfer functions was measured for different aperture settings (see Section 4.4.1). An interesting outcome of these investigation was the observation a polarization depending disturbance in the OAC transfer function measurement and the transmitted optical power (see Section 4.4.2).

After the transfer function measurements, the power stabilization experiment was performed at atmospheric pressure and at low pressure for different photocurrents detected by the in-loop detector.

#### 4.4.1 Transfer function measurements

In a series of measurements the aperture was opened stepwise to change the impedance matching of the resonator. For each step the OAC transfer function was measured.

Figure 4.11 shows a set of OAC transfer functions measured within this series, together with a set of theoretical OAC transfer functions with matched OAC gains.

Note how a smaller corner frequency is necessary to match the transfer functions to the measurements. The behavior of the resonator

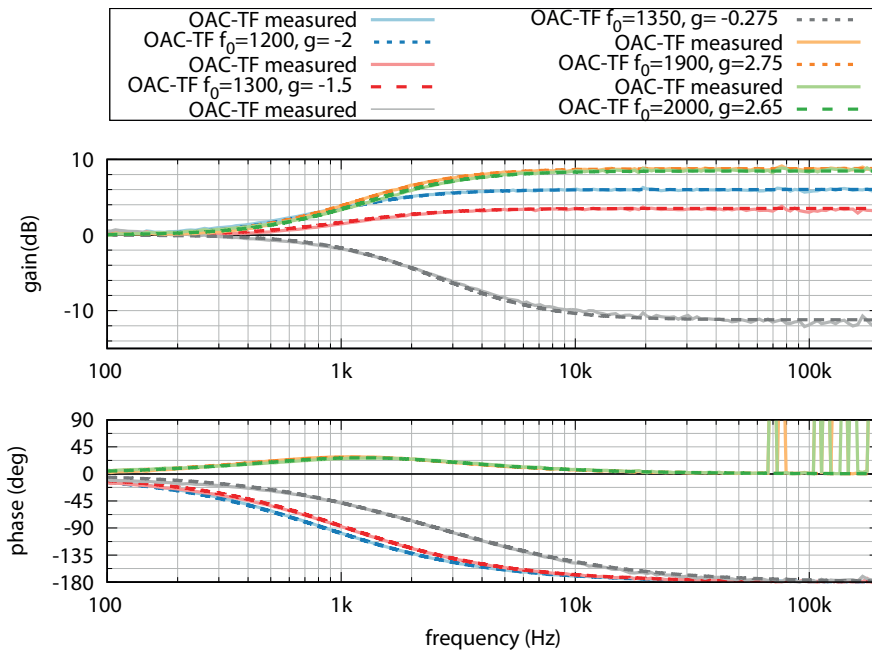


**Figure 4.11:** OAC transfer functions for different impedance matchings showing the evolution of the OAC gain factor  $g$  with decreasing corner frequency  $f_0$  from 2000 Hz down to 1200 Hz. Note how the green transfer function has less gain and a higher corner frequency compared to the orange curve. This demonstrated the decrease of OAC gain for high values of the impedance matching, see Sec.3.3

resembles what is theoretically expected from a OAC resonator with imperfect mode matching, described in Section 3.2.

For the strongest undercoupled situation ( $f_0 = 2000$  Hz) the gain is slightly decreased compared to the measurement with slightly better impedance matching ( $f_0 = 1950$  Hz). Since the OAC resonator is not perfectly mode matched, the OAC gain factor can become an attenuation ( $|g| = 0.275$ ) for slightly overcoupled impedance matching<sup>5</sup>. The gain then starts to increase ( $|g| = 1.5$  at  $f_0 = 1300$  Hz) and reaches  $|g| = 2$  at  $f_0 = 1200$  Hz.

The maximum optical AC coupling gain factor which could be achieved in the experimental setup was limited by the mode matching coefficient  $p$ , which was estimated to be  $p \leq 0.05$ .

<sup>5</sup>See Sec. 3.3. Another measurement showed an OAC gain  $|g| = 0.07$ , but is not depicted in figure 4.11 for scaling reasons.

### 4.4.2 Polarization effects

In an earlier stage of the experiment the light reflected of the OAC resonator was separated with an PBS-quarter wave plate combination. The quarter wave plate converted the light to circular polarization which then is incident to the OAC resonator.

After reflection by the OAC resonator, the light propagates through the wave plate for a second time and is converted back to linear polarization. Passing the waveplate two times converts vertically polarized light into horizontally polarized light and vice versa. The PBS therefore separates the reflected beam from the incoming beam. This configuration should work for a linear resonator, since the polarization eigenmodes of the resonator should be degenerated.

However, this configuration was found to be problematic for this experiment, which showed a polarization dependent behavior of the OAC resonator. This behavior was observed in two different ways: With a frequency stabilized resonator, the intensity pattern, observed with the CCD cameras in reflection and transmission, could switch between two different locking states, which were accompanied by a change in transmitted and reflected optical power. Furthermore, it was not possible to measure OAC transfer functions with a gain higher than  $g = 6$  dB and the transfer function measurements showed a distortion around 6 kHz.

Frequency splitting of higher order resonator eigenmodes in a Fabry-Perot cavity can be caused by birefringence [81, 82], which is usually attributed to stress in the mirror substrates or mirror coatings, induced by specific mirror mounting. A second source is found in astigmatism, which can be introduced by elliptical cavity mirrors in high Finesse resonators[83–87]. To estimate the frequency splitting of these higher order modes corrections to the paraxial theory become necessary [88, 89]. These corrections are usually assuming a cylindrical symmetry and therefore result in a degeneracy of the fundamental mode of the resonator for both polarizations. Recently, it has been shown that the fundamental resonator eigenmode can split into different polarizations due to elliptical mirrors, both experimentally as well as theoretically [90]. However, this splitting of the fundamental eigenmode does only appear if the mirrors' radii of curvature approach the wavelength of the laser and therefore is unlikely to explain the observed effect in this experiment.

In the final setup, linear polarized light was sent towards the OAC resonator and a Faraday isolator was used to separate the reflected

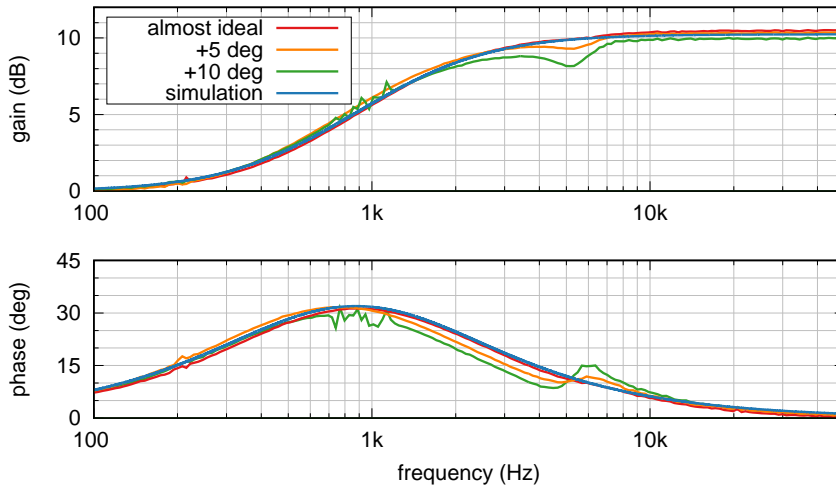


**Figure 4.12:** OAC transfer functions for different orientations of linear input polarization. A deviation from the ideal OAC transfer function appears in the gain and phase around 6 kHz, when the input polarisation is not aligned to one of the cavity polarization axis

beam from the incoming beam. The polarization orientation of the linear polarized beam was adjusted with a half wave plate to minimize the features in the OAC transfer function. This optimization process is shown in Figure 4.12, which shows the OAC transfer function for different positions of the half wave plate.

#### 4.4.3 Power stabilization experiment at atmospheric pressure and 0.3 mA photocurrent

The power stabilization experiment was initially performed at atmospheric pressure and with a detected photocurrent of  $i_{IL} = 0.3 \text{ mA}$ . Important sensors for the experiment are  $PD_{OOL}$ , serving as out-of-loop sensor,  $PD_{trans}$  as sensor for the transmitted relative power noise<sup>6</sup> and  $PD_{IL}$  as in-loop sensor. Figure 4.13 shows the relative power noise on these sensors for different configurations of the experiment.

<sup>6</sup>Due to the passive filtering of the resonator, power noise in transmission of the resonator fell below the shot noise limitation of  $PD_{trans}$ . Hence, measurements performed with this sensor are only shown up to frequencies of 20 kHz

## 4 OAC with a narrow linewidth resonator

---

With an open power stabilization feedback control loop  $PD_{\text{OOL}}$  measures the free running power noise of the NPRO, which is transmitted through the fiber into the vacuum tank and directed towards the OAC resonator.

A first test of the power stabilization feedback control loop was performed with an unlocked OAC resonator. In this configuration the OAC resonator acts as a normal mirror and the power stabilization feedback control loop is equivalent to a classical power stabilization feedback control loop.

The performance of this classical setup was shot noise limited for frequencies above 2 kHz, showing a slightly increased noise which can be attributed to the dark noise of the in-loop photodetector.

After this initial test, the OAC resonator was locked and the optical power reaching the in-loop detector was adjusted to  $i_{\text{IL}} = 0.3 \text{ mA}$ .

The OAC based power noise stabilization feedback loop showed a superior performance compared to the classical power stabilization configuration for frequencies above 4 kHz, while the OOL relative power noise increased dramatically compared to the classical setup for frequencies below 4 kHz.

To investigate this increased power noise the relative power noise was measured in transmission of the locked OAC resonator with  $PD_{\text{trans}}$ , as well as in reflection of the stabilized OAC resonator, with and without a closed power stabilization feedback control loop.

With an open power stabilization feedback control loop, the transmitted power noise differs from the incoming power noise in two aspects. As expected, the cavity acts as a low pass filter for amplitude fluctuations and therefore filters the power noise above the resonator linewidth down to the shot noise level of the detected beam. The second deviation appears at low frequencies, which show a significantly increased relative power noise below 2 kHz. This power noise has a similar shape to the OOL power noise of the OAC power stabilization feedback control loop.

An increased relative power noise in this frequency regime, again having a similar shape, is also seen with the in-loop detector used for the power stabilization experiments whenever the resonator is locked and the power stabilization feedback control loop is open.

Therefore, the increased OOL power noise of the OAC power noise feedback control loop is a consequence of a noise source which creates power noise in reflection and transmission of the stabilized OAC resonator.



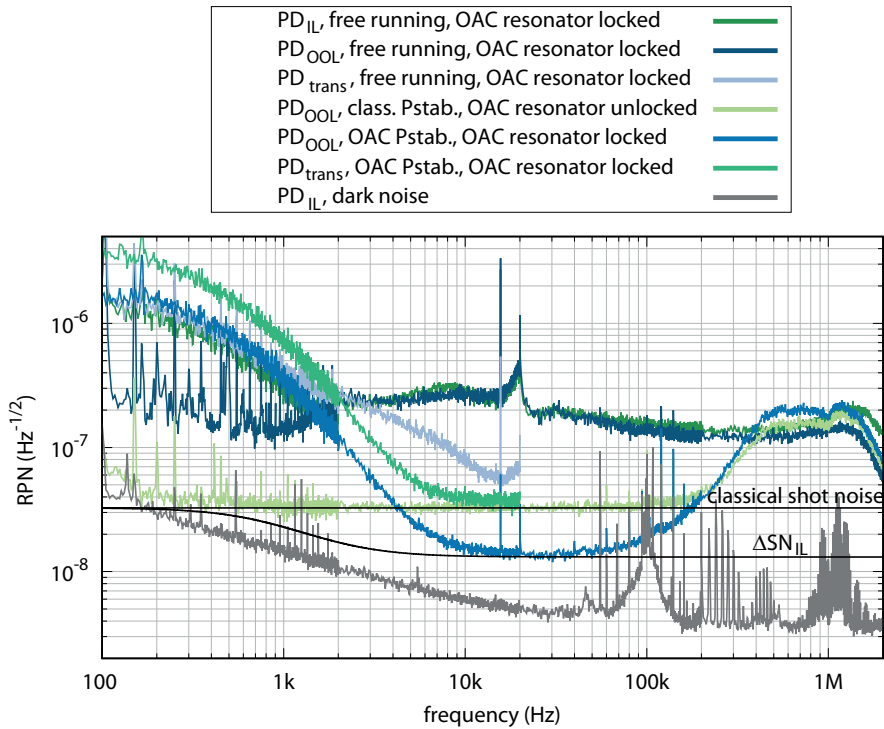


**Figure 4.13:** Performance of the 2kHz Optical AC coupling power stabilization experiment at atmospheric pressure compared to the classical power stabilization (unlocked OAC resonator) and the free running noise of the beam transmitted through the fiber. An unknown noise sources causes excess noise in transmission and reflection of the OAC resonator, when the power stabilization feedback control loop is open and the OAC resonator locked. The OOL stability of the OAC based power stabilization is superior to the classical stabilization for frequencies above 4 kHz. Below 4 kHz the OAC power stabilization is limited by the unknown noise source. Note how the transmitted power noise increases when the OAC power stabilization feedback loop is closed.

## 4 OAC with a narrow linewidth resonator

---

Several tests were performed to find the origin of this noise source. Coherence measurements between beam pointing in reflection of the stabilized OAC resonator to the OOL power noise were performed with a temporarily installed quadrant photodiode. These measurements showed no indication of a connection between beam pointing and the source of the power noise.

The conversion of frequency noise between laser and OAC resonator to additional power noise in reflection of the resonator was ruled out with coherence measurements between the error signal of the frequency stabilization feedback control loop and the OOL power noise as well.

An interesting effect was observed in the transmitted power noise, with a closed OAC power stabilization feedback control loop: the transmitted power noise was increased compared to the free running noise, which could point towards a resonator internal noise source.

For an under-coupled OAC resonator, a noise source from the inside of the resonator would have a phase flip compared to the resulting carrier component in reflection of the resonator. This means that an increase in the resonator internal field would look like a decrease in the resulting reflected field. The control loop would then increase the incoming power noise to extinguish the power noise in reflection, which in turn would result in an increased power noise in transmission of the resonator.

### 4.4.4 Power stabilization experiment below 10 mBar and 0.3 mA photocurrent

The in air measurements did verify that an improvement in shot noise limited performance compared to a classical power stabilization feedback control loop was reachable with the OAC experiment. The next phase of the experiment was the evacuation of the vacuum tank to low pressure levels of below 10 mbar. Since the half wave plate to adjust the power on the in-loop sensor could not be used for power adjustments after the evacuation of the tank, the power was adjusted before the pump down.

The adjustment process was complicated by the evacuation process of the vacuum tank, which led to a reduction in the power transmitted through the fiber. The cause of this change in transmitted power is unknown, but might be attributed to stress in the fiber induced by the pressure differences between the inside and the outside of the tank. Since the reduction of power transmitted through the fiber could reach

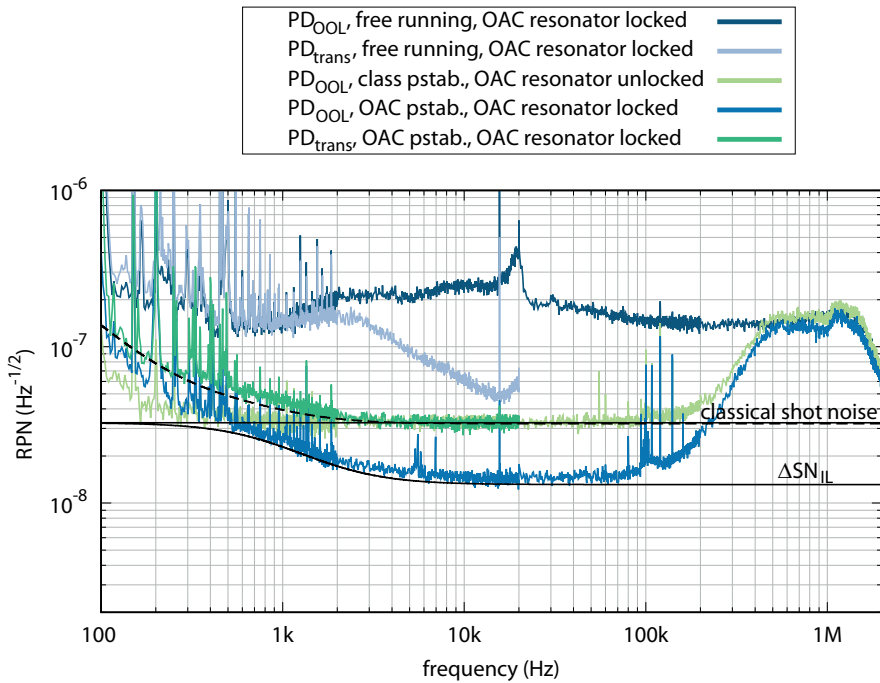


**Figure 4.14:** Performance of the 2 kHz Optical AC coupling power stabilization experiment at pressure levels below 10 mbar compared to the classical power stabilization, the free running noise measured with the OOL detector and the transmitted noise with and without OAC power stabilization. The unknown noise source, seen in Fig. 4.13, is not present any more and the transmitted free running noise is equal to the free running beam transmitted through the fiber, except for the passive filtering of the resonator. The stabilized transmitted power noise is limited by the shot noise level of the TPD and the OOL stability reached by the OAC power stabilization feedback loop (indicated by the black dashed line).

up to 20% over the timespan necessary for evacuating the tank and finishing a set of measurements, it had to be considered before starting the evacuation process. To be able to compensate for the power drop on the inside of the tank, the power coupled into the fiber was reduced with the first half wave plate after the NPRO laser, before the power on the in-loop sensor was adjusted with the stabilized OAC resonator. Then, the evacuation process was started and after reaching the final pressure level, the power was readjusted with the half wave plate behind the NPRO.

Figure 4.14 shows the results of the OAC power stabilization for pressure levels below 10 mbar.

An out-of-loop performance very close to the expected shot noise level

## 4 OAC with a narrow linewidth resonator

---

inferred from the OAC transfer function measurement, was reached by the Optical AC coupling based power stabilization.

The noise source below 2 kHz, which limited the experiment at atmospheric pressure, was not present with the evacuated vacuum tank. Furthermore, the power noise in transmission for an open loop looked exactly like the free running noise of the incoming beam, except for the low pass filter effect of the OAC resonator.

With the closed loop the noise in transmission dropped down to the shot noise limit of the photodiode in transmission of the resonator for frequencies above 2 kHz. The transmitted power noise for frequencies below 2 kHz can be estimated closely by calculating the uncorrelated sum of the out of loop power noise and the shot noise level of the transmitted beam.

### Noise discussion

Several noise sources influencing the out of loop performance of the experiment could be estimated:

- **In-loop shot noise:** The shot noise contribution  $\Delta SN_{IL}$  of the in-loop detector  $PD_{IL}$  has to be calculated taking into account the OAC transfer function  $G_{OAC}$  and the shot noise level of the in-loop detector  $\Delta RPN_{shot,IL} = 3.26 \cdot 10^{-8} \text{ Hz}^{-1/2}$ .

$$\Delta SN_{IL}(f) = \frac{RPN_{shot,IL}}{|G_{OAC}(f)|} \quad (4.10)$$

- **In-loop dark noise:** To estimate the dark noise contribution  $\Delta DN_{IL}(f)$  of the in-loop detector to the overall noise, the voltage dark noise of the in-loop detector  $\Delta V_{dark,IL}(f)$  is measured with a spectrum analyzer and normalized with the DC voltage  $V_{DC,IL}$ . In a similar fashion as for the shot noise contribution, the OAC transfer function  $G_{OAC}$  has to be taken into account as well:

$$\Delta DN_{IL}(f) = \frac{\Delta V_{dark,IL}(f)}{V_{DC,IL} \cdot |G_{OAC}(f)|} \quad (4.11)$$

- **Out-of-loop shot noise:** The shot noise  $\Delta SN_{OOL}$  of the out-of-loop detector  $PD_{OOL}$  can be deduced from the detected photocurrent  $i_{OOL}$ , which was estimated to be about 50 mA and therefore contributes with:

$$\Delta SN_{OOL} = RPN_{shot,OOL} \quad (4.12)$$

- **Out-of-loop dark noise:** To estimate the dark noise contribution  $\Delta\text{DN}_{\text{OOL}}$  of the out-of-loop sensor the voltage dark noise  $\Delta V_{\text{dark,OOL}}(f)$  is measured directly with a spectrum analyzer and has to be normalized with the DC voltage of the OOL sensor  $V_{\text{DC,OOL}}$ :

$$\Delta\text{DN}_{\text{OOL}}(f) = \frac{\Delta V_{\text{dark,OOL}}(f)}{V_{\text{DC,OOL}}} \quad (4.13)$$

- **Conversion of frequency noise to relative power noise:** Frequency noise between the laser frequency and the resonator resonance frequency is converted into relative power noise in reflection of the OAC resonator according to Eq. 3.47. However, calculating the exact conversion is difficult, as it strongly depends on the remaining frequency offset  $\Delta\nu$ , the impedance matching  $\alpha$  and the remaining frequency noise between laser and OAC resonator.

The coupling however, can be projected using a transfer function measurement between the error point of the frequency feedback control loop and the OOL power noise. The contribution of the frequency noise conversion  $\Delta\text{NF}(f)$  was then projected as the product of the error point voltage noise spectrum and the measured transfer function. In the process of measuring the transfer function the optimization of the error point offset voltage adjusted such that the magnitude of the transfer function was minimized.

To estimate the overall expected out-of-loop power noise the uncorrelated sum of these noise contributions has to be calculated. A graphical illustration of the different noise contributions and the overall sum can be found in Figure 4.15. The dark noise contributions  $\Delta\text{DN}_{\text{ool}}(f)$  and  $\Delta\text{DN}_{\text{IL}}(f)$  were approximated with analytical functions  $\Delta\text{DN}_{\text{sim,OOL}}(f)$  and  $\Delta\text{DN}_{\text{sim,IL}}(f)$  (shown as dashed lines) to get a clean projection for the overall noise.

A typical projection for the out-of-loop power noise created by frequency noise conversion  $\Delta\text{NF}(f)$  is shown in Figure 4.15. Due to its complex frequency dependency it is approximated by a constant value of  $1.7 \cdot 10^{-9} \text{ Hz}^{-1/2}$ . The underestimation at low frequencies caused by this approximation is not relevant, since the noise is dominated by the dark noise contribution of the in-loop detector. At frequencies above 20 kHz the coupling is slightly overestimated, again is not relevant in the overall noise projection. The total noise is then calculated

## 4 OAC with a narrow linewidth resonator

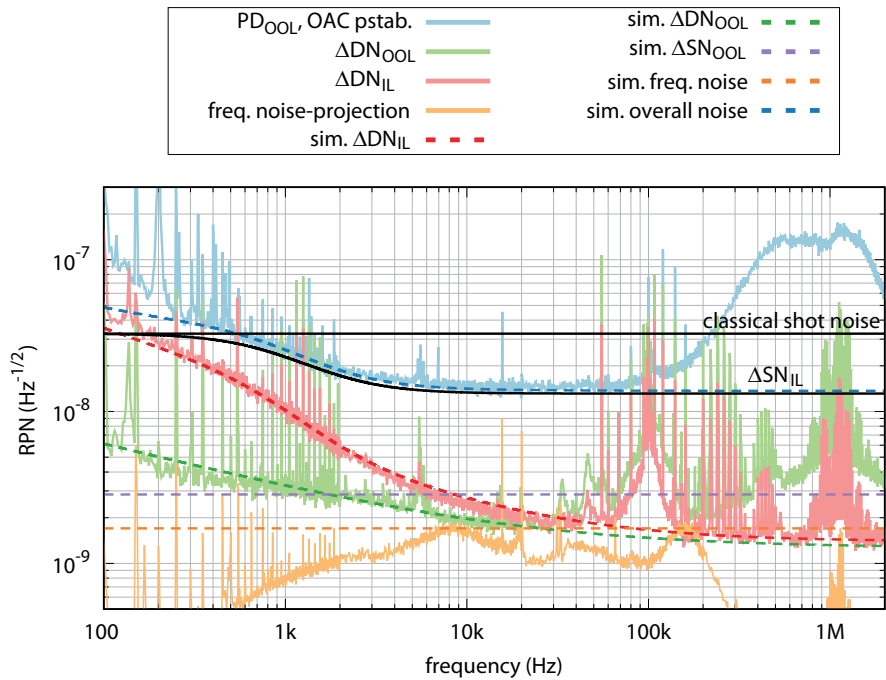


**Figure 4.15:** Noise investigation for the 2 kHz Optical AC coupling power stabilization experiment below 10 mBar and a detected photocurrent  $i_D = 0.3 \text{ mA}$ . The dark noise contributions of the  $\Delta\text{DN}_{\text{IL}}(f)$  and  $\Delta\text{DN}_{\text{OOL}}$  were measured and then approximated (shown as dashed lines). The shot noise contribution  $\Delta\text{SN}_{\text{IL}}$  is shown as black line, while  $\Delta\text{SN}_{\text{OOL}}$  is calculated and shown as red dashed line. A projection of the frequency noise to power noise conversion is shown in light orange.

as uncorrelated sum:

$$\Delta\text{RPN}_{\text{sum}} = \left( (\Delta\text{NF}(f))^2 + (\Delta\text{SN}_{\text{IL}})^2 + (\Delta\text{SN}_{\text{OOL}})^2 \right) \quad (4.14)$$

$$+ \left( (\Delta\text{DN}_{\text{sim,OOL}}(f))^2 + (\Delta\text{DN}_{\text{sim,IL}}(f))^2 \right)^{\frac{1}{2}} \quad (4.15)$$

The sum of the known noise contributions discussed above does almost resemble the measured OOL power noise, except for frequencies below 400 Hz, where an unknown noise sources causes a remaining discrepancy.

#### 4.4.5 Power stabilization experiment below 10 mBar and 1 mA photocurrent

To shift the OOL performance of the system to lower RPN levels and have a closer look at potential noise sources, like the noise source at low frequencies, observed in Section 4.4.4, the photocurrent detected with the in-loop detector was increased to  $i_{\text{D}} = 1 \text{ mA}$ . The resulting OOL power noise performance of the OAC power stabilization feedback control loop is shown in Figure 4.16.

For this stabilization experiment the OAC gain factor was measured to be  $g = 9 \text{ dB}$ . The known noise contributions were estimated as in Section 4.4.4 and are plotted together with their uncorrelated sum in Fig. 4.16. For almost all frequencies, the expected noise completely explains the deviation of the out-of-loop performance from the expected OAC shot noise level. However, at low frequencies the OOL performance was again limited by an unknown noise source, having similar magnitude and shape as in the 0.3 mA experiment. Its is worth mentioning, that the experiment was not optimized for a photocurrent of  $i_{\text{D}} = 1 \text{ mA}$  and a better performance for frequencies above 3 kHz was prevented by the significant contribution of the out-of-loop shot noise  $\Delta\text{SN}_{\text{OOL}}$ .

Nevertheless, an out-of-loop stability of  $8 \cdot 10^{-9} \text{ Hz}^{-1/2}$  was reached for frequencies around 20 kHz.

## 4.5 Discussion

The goal to improve the power stability achievable with the OAC technique at lower frequencies, has been achieved. To demonstrate this

## 4 OAC with a narrow linewidth resonator

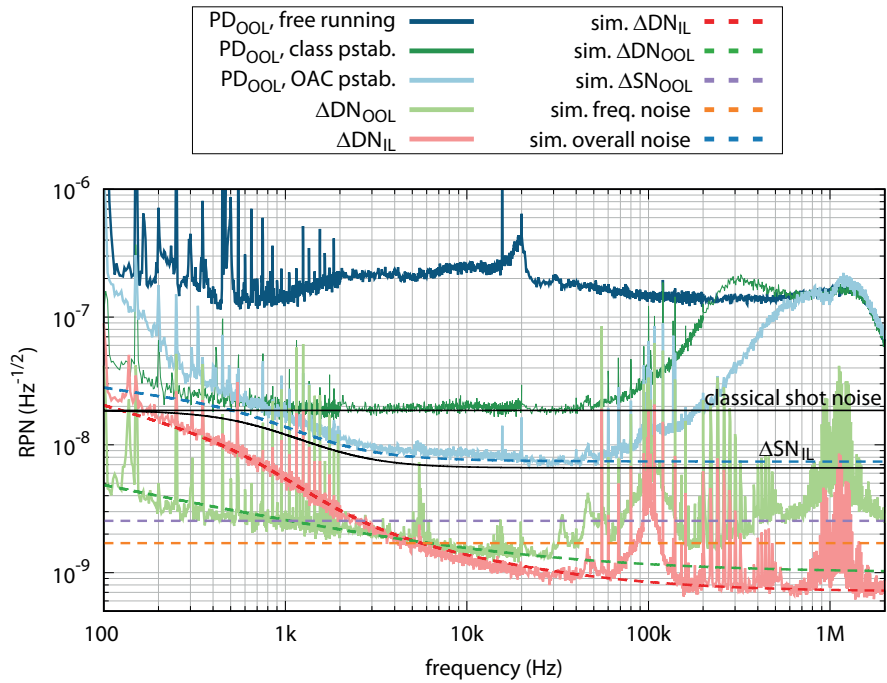


**Figure 4.16:** Noise investigation for the 2 kHz Optical AC coupling power stabilization experiment below 10 mBar and 1 mA photocurrent. The dark noise contributions of the  $\Delta\text{DN}_{\text{IL}}(f)$  and  $\Delta\text{DN}_{\text{OOL}}$  were measured and then approximated (shown as dashed lines). The shot noise contribution  $\Delta\text{SN}_{\text{IL}}$  is shown as black line, while  $\Delta\text{SN}_{\text{OOL}}$  is calculated and shown as red dashed line.



improvement, the results of this thesis are compared to the results obtained by Kwee in 2010 in Figure 4.17.

The out-of-loop performance of the new experiment surpasses the experiment by Kwee for frequencies below 30 kHz and reaches a four times (12 dB) lower relative power noise, for frequencies below 3 kHz. An even better performance was prevented by several known noise sources and an unknown noise source below 2 kHz.

At 10 kHz the OOL performance is still a factor 2 (6 dB) better than previous experiments. For frequencies above 40 kHz the experiment could not reach the performance of earlier experiments, which is due to the imperfect mode matching and therefore smaller OAC coupling gain.

Up to this point it is not clear if the excess power noise at low frequencies is OAC sensor noise produced by the OAC resonator (see Section 3.5) or conventional sensor noise (as discussed in Section 2.4.2), which could be caused by beam pointing or stray light effects.

The new setup is the first OAC coupling power stabilization experiment using the Pound-Drever-Hall technique for the frequency stabilization of the OAC resonator. Therefore, the compatibility of OAC with PDH was experimentally confirmed in a power stabilization feedback control loop, which will be key for a possible implementation of OAC at a gravitational wave detector (see Chapter 5).

## 4.6 Chapter Outlook

Since an investigation of the excess low power noise at low frequencies is the logical next step for this experiment, the possibilities to decrease the known noise contributions of the experiment are discussed in this section.

The in loop shot noise contribution  $\Delta SN_{IL}(f)$  can be lowered by an increase of the OAC gain factor, or simply by increasing the detected photocurrent. With a significant increase of the optical power detected by the OAC detector an automatic shutter might become necessary to shield the detector from the higher power levels occurring at a loss lock of the OAC resonator.

An increase of the OAC gain factor demands an improved mode matching factor  $p$ . To estimate an upper limit for the best possible mode matching, a complete characterization of the beam purity inside the vacuum tank needs to be performed.

However, measuring the distance between the mode matching lenses

## 4 OAC with a narrow linewidth resonator

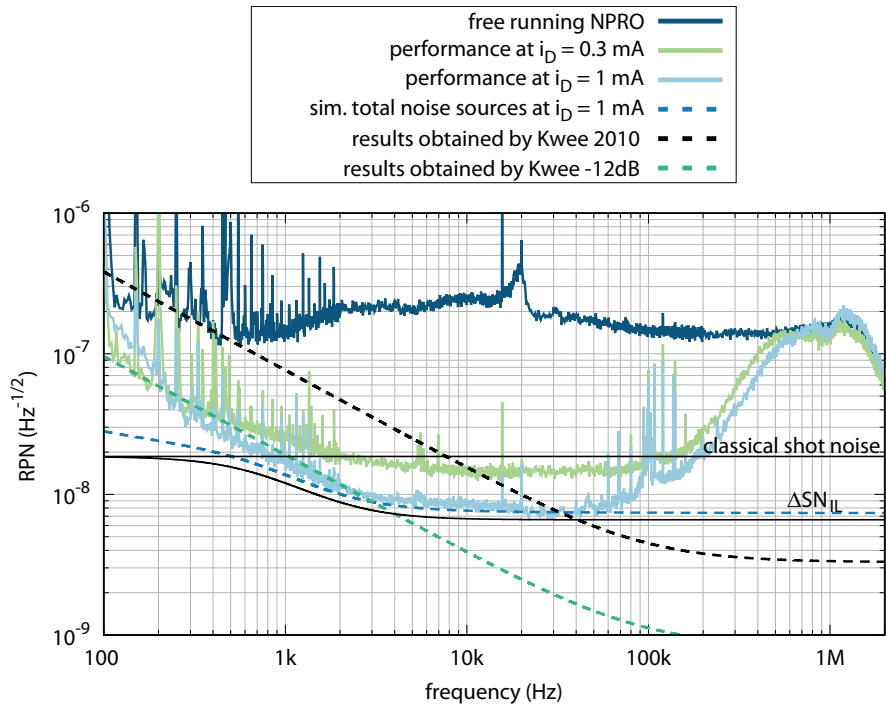


**Figure 4.17:** The performance of the new experiment is compared to the results achieved by Kwee (black dashed line). The performance of the new experiment improves the OOL performance achieved with an OAC power stabilization by a factor of 4 for frequencies below 3 kHz (indicated by the green dashed line). The sum of known noise contributions (blue dashed line) can not fully explain noise for low frequencies.

and the input coupling mirror of the OAC resonator will remain difficult with the current setup, due to the protruding resonator spacer. A better solution might be a spatial extension of the platform to allow for a positioning of the alignment mirrors on the plane of the platform. A different approach is the use of an additional mode cleaner resonator in front of the OAC detector, which is matched to the fundamental mode of the OAC resonator and therefore suppresses the non resonant mode contributions.

The electronic dark noise of the OAC detector  $\Delta DN_{IL}(f)$  seems to be sufficiently low, even with increased OAC gain, since the voltage noise contributions has to be scaled with  $g$ .

Coupling of frequency noise to power noise in reflection of the OAC resonator was not a major noise contribution yet. With a reduction of the other noise sources, further suppression of frequency noise might become important. As demonstrated in Section 3.3, a better mode matching, requires a better impedance matching to achieve the maximum OAC gain factor  $g$ . However, it might be considered to trade some of the OAC gain against lower out-of-loop power noise produced by frequency conversion (see Sec.3.5.1). The bandwidth of the frequency noise feedback control loop was limited by the mechanical resonance frequencies of the custom built EOM. Therefore, the bandwidth could either be increased with additional notch filters to suppress the mechanical resonances of the custom build EOM or by using a new EOM with better suited resonance frequencies. If an increased bandwidth is not sufficient the loop shape can be further optimized.

The shot noise of the out-of-loop detector was found to be a major noise contribution at high frequencies. The photocurrent detected with this sensor was about 50 mA and can be increased to about 60 mA using the same detector. A further increase of the optical power on the out-of-loop detector will be limited in a similar manner to the one discussed in Section 2.7.

Due to its tunable impedance matching, the new OAC experiment will allow the first over-coupled OAC power stabilization feedback control loop to be set up. An over-coupled OAC power stabilization would be a necessary proof-of-principle experiment on the track towards an implementation of OAC at a gravitational wave detector (see chapter 5). Because of the  $180^\circ$  phase flip between carrier and sidebands, which is inherent to the overcoupled OAC transfer function, additional electronic filtering might be necessary to achieve a stable control loop.

## 4 OAC with a narrow linewidth resonator

---

# 5

## Chapter 5

# Optical AC coupling for gravitational wave detectors

The first direct detection of gravitational waves from binary black hole mergers [9, 91, 92] and the detection of gravitational waves from a neutron star collision [93], which allows for multi messenger astronomy [94], creates a rapid growth in the interest to have even more precise gravitational wave detectors.

A variety of future detector concepts have been proposed already. The A+ Design [95] will focus on upgrading the existing aLIGO facilities to the best performance possible with the current infrastructure. The upgrade will include heavier mirrors and an implementation of frequency dependent squeezing to allow for a reduction of shot noise and radiation pressure noise at the same time[35, 96, 97].

More advanced designs for future detectors, such as the Einstein Telescope [98] (ET, 10 km arm length) or the Cosmic Explorer (CE, 50 km arm length), will require completely new infrastructure instead. ET and CE aim to increase the sensitivity by one order of magnitude for the whole measurement band.

There is no definite laser power stability requirement specified for these next generation gravitational wave observatories yet. Due to the increased laser power and the higher sensitivities required, the new stability requirements are likely to be even more strict than the aLIGO requirements.

Optical AC coupling could provide a way of satisfying future power stability requirements and, furthermore, seems to be tailor made for use in gravitational wave detectors, as they inherently provide resonators with extremely narrow linewidths. This is due to the fact

## 5 Optical AC coupling for gravitational wave detectors

---

that all of current (2nd) generation and next generation GWDs have an important similarity: They rely on the power recycling technique [99–101] to increase the circulating laser power. This is true also for the newly proposed speed meter topologies [102].

Depending on the specific interferometric layout a coupled cavity, with a corner frequency  $f_0$  of about 0.6 Hz (aLIGO) or 20 Hz (GEO 600), is formed by the power recycling resonator and the interferometer.

While OAC was already successfully demonstrated in laboratory experiments, it had yet to be demonstrated in a gravitational wave detector. Within this thesis the first investigations towards a possible implementation of the OAC technique at a GWD were performed.

Section 5.1 describes the measurement of the OAC transfer function at the aLIGO detector in Livingston Louisiana, USA. In Section 5.2 a similar measurement at the GEO 600 detector is presented. Furthermore, this section describes the first experiments towards an actual implementation of the OAC technique in the power stabilization feedback control loop of GEO 600.

### 5.1 Investigations of OAC at aLIGO

The first step towards an implementation of the Optical AC coupling technique is the measurement of an OAC transfer function. Within this thesis the OAC transfer function was measured at the aLIGO detector in Livingston Louisiana and compared with a simulation of the interferometer. The main results of this section were already published in [62].

#### 5.1.1 Optical Layout of aLIGO

The complete optical Layout of aLIGO consists of a multitude of optical components, hence a simplified and reduced layout is presented in Figure 5.1. It only shows optical components, which are essential for the understanding of the OAC transfer function measurement.

The laser light of aLIGO is provided by the so called 200 W pre-stabilized-laser system (PSL). The PSL combines a high power laser source [103–105], with a pre-mode-cleaner, used for spatial filtering of the beam, a frequency stabilization of the laser frequency to a reference cavity and an initial power stabilization feedback control loop [43, 106]. It contains a high power acousto-optical modulator, which

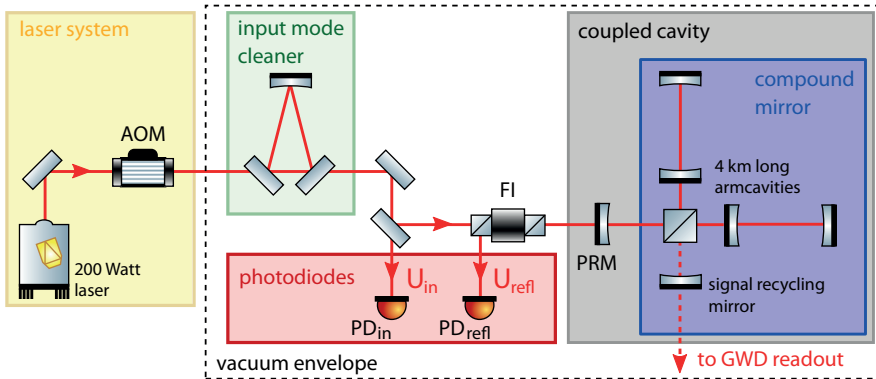


**Figure 5.1:** This is simplified optical layout of the aLIGO Livingston detector. The beam from the PSL laser system is coupled through the AOM and the input mode cleaner, before it is transmitted through the Faraday isolator and enters the coupled cavity, formed by the power recycling mirror (PRM) and the compound mirror, comprised by the interferometer and the arm cavities. The photodiodes  $PD_{in}$ , used to measure the the incoming field  $U_{in}$ , is placed in transmission of an alignment mirror, downstream of the IMC.  $PD_{refl}$ , which measures the reflected field  $U_{refl}$ , is placed in the reflection path of the coupled cavity, which is separated from the incoming beam at the Faraday isolator (Reproduced from [62] © IOP Publishing Ltd. CC BY 3.0.)

is usually used as the actuator for the power stabilization feedback control loop. The AOM is the only component of the PSL depicted in Figure 5.1, since it was used to imprint the power fluctuations necessary for the OAC transfer function measurement.

After transmission through the AOM, the beam enters the vacuum envelope and is coupled through the input mode cleaner (IMC), which is a suspended, 16.7 m long, three mirror resonator with a Finesse of 515 [107]. Downstream of the IMC the beam is sent through a high power Faraday isolator (FI), before it enters the coupled cavity formed by the power recycling mirror (PRM) and the 4 km arm length interferometer.

The interferometer comprised by the beam splitter and the arm cavities [108] is stabilized to the dark fringe operation point, such that almost all light is reflected back towards the input port. Hence the interferometer can be described by a compound mirror, which is interpreted as the second mirror of the coupled cavity[62].

As in the laboratory experiments power modulation incident and reflected by the coupled cavity need to be detected to measure an OAC transfer function. The incident modulations are measured with  $PD_{in}$ ,

## 5 Optical AC coupling for gravitational wave detectors

---

which is located in transmission of an alignment mirror downstream of the IMC.

The beam reflected by the coupled cavity is separated by the Faraday isolator from the incident beam. This is where the second photodiode  $\text{PD}_{\text{refl}}$ , which measures the modulations reflected from the coupled cavity, is located.

Since these photodiodes were already installed as a part of the standard aLIGO optical layout, they could be used without further modifications for the OAC transfer function measurement. The usual purpose of  $\text{PD}_{\text{refl}}$  is to create error signals for the common arm length degree of freedom (DOF) and the signal recycling cavity length DOF [109]. At the time of the experiment  $\text{PD}_{\text{in}}$ , was used as a sensor for the final power stabilization feedback control loop. Consequently this part of the feedback control loop had to be disabled to allow for our transfer function measurement, otherwise the imprinted modulation would have been suppressed.

### 5.1.2 Transfer function measurement

The measurement of the OAC transfer function at the aLIGO gravitational wave detector is performed in a similar way to the laboratory experiment described in chapter 4. The AOM is used to imprint amplitude modulations and the signal measured in reflection of coupled cavity, measured with  $\text{PD}_{\text{refl}}$  is compared to the incident power modulation, measured with  $\text{PD}_{\text{in}}$ .

Due to the corner frequency of 0.6 Hz, a transfer function measurement with a swept sine over the frequency range of interest, is very time demanding.

Another complication arises due to the presence of several mirror suspension resonance frequencies within the desired measurement band, which could be excited by incident power modulations.

Therefore, two different measurement methods were chosen. For frequencies between 5 Hz and 1 kHz the standard procedure of injecting a broadband amplitude modulation could be used to measure the transfer function.

In the range between 0.1 Hz and 100 Hz single frequency amplitude modulations, with a modulations coefficient up to  $m = 0.02$ , were imprinted and the transfer function at the specific modulation frequency was measured. The frequencies were chosen with sufficient distance to the well known mechanical resonance frequencies of the suspensions to avoid a possible excitation.



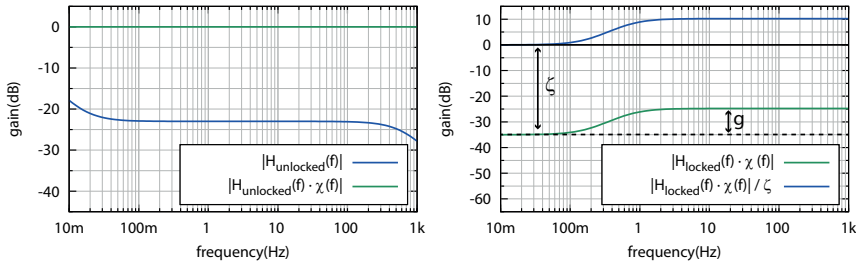


**Figure 5.2:** Left: Transfer function between photodiodes with an unlocked interferometer without calibration factor  $\chi(f)$  (blue) and the same transfer function with the calibration factor applied. Right: Calibrated transfer function  $H_{\text{locked}}(f) \cdot \chi(f)$  between both photodiodes with the locked interferometer (green). The same transfer function after normalization with the independently measured carrier reduction  $\zeta$ .

To compare the two measurement methods the single frequency modulations were also performed above 5 Hz and showed no deviations between both methods.

### Calibration

The Optical AC coupling gain factor  $g$  is the difference in the magnitude of the transfer function at frequencies  $f \ll f_0$  and  $f \gg f_0$ .

Measuring the magnitude at frequencies far above the corner frequency is usually unproblematic. However, to measure at frequencies significantly lower as the corner frequency of the coupled cavity at aLIGO, a measurement at  $f < 10$  mHz has to be performed. This is demanding due to long integration times required for a single transfer function measurement and the high excess power noise in reflection of the power recycling cavity. This excess noise not only requires a strong modulation, but also degrades the coherence between the injected and reflected signal and therefore requires a higher number of averages to achieve a significantly coherent measurement. The lower frequency magnitude of the transfer function measurement was therefore inaccessible for this experiment.

An adapted calibration method to estimate the Optical AC coupling gain factor was used instead, see Figure 5.2.

In a first step the AC signals of the photodiodes  $PD_{\text{in}}$  and  $PD_{\text{refl}}$  are calibrated relative to each other to account for different optical and electronic gains between them (see Figure 5.2). To allow for a measurement of the frequency dependent calibration factor  $\chi(f)$ , the

## 5 Optical AC coupling for gravitational wave detectors

---

central beam splitter of the interferometer is intentionally misaligned and the beam is centered on  $\text{PD}_{\text{refl}}$  by actuation on PRM. In this state the AOM is used to imprint a broadband modulation and a transfer function  $H_{\text{unlocked}}$  from the PD output signals  $V_{\text{in,AC,unlocked}}$  to  $V_{\text{refl,AC,unlocked}}$  is measured:

$$H_{\text{unlocked}}(f) = \frac{V_{\text{refl,AC,unlocked}}(f)}{V_{\text{in,AC,unlocked}}(f)} \quad (5.1)$$

Since the interferometer is unlocked, PRM acts as a simple mirror and the power modulations  $P_{\text{in}}(f)$  and  $P_{\text{refl}}(f)$  are of equal size. Therefore, the calibration factor is given by  $\chi(f) = 1/H_{\text{unlocked}}(f)$  and can be used to calibrate the photodiodes relative to each other:

$$\chi(f) \cdot \frac{V_{\text{refl,AC,unlocked}}(f)}{V_{\text{in,AC,unlocked}}(f)} = \frac{P_{\text{refl,AC}}(f)}{P_{\text{in,AC}}(f)} = 1 \quad (5.2)$$

In the locked state, the optical power on  $\text{PD}_{\text{refl}}$  is reduced with the carrier reduction  $\zeta \leq 1$ , introduced in Section 3.4, while  $\text{PD}_{\text{in}}$  still sees the same amount of optical power.

$$\zeta = \frac{P_{\text{refl,DC,locked}}}{P_{\text{in,DC}}} = a^2(1-p) + p \quad (5.3)$$

Therefore the measured calibrated transfer function  $H_{\text{locked}}(f) \cdot \chi(f)$  has to be normalized with the carrier reduction (see Figure 5.2, right), to end up with OAC transfer function measurement:

$$G_{\text{oac}}(f) = \frac{P_{\text{refl,AC}}}{P_{\text{in,AC}}} \cdot \frac{P_{\text{in,DC}}}{P_{\text{refl,DC}}} = \chi(f) \cdot H_{\text{locked}}(f) / \zeta \quad (5.4)$$

Hence the second step of the calibration procedure was an independent measurement of the carrier reduction  $\zeta$ , which was simply monitored with the DC-Voltage of  $\text{PD}_{\text{refl}}$  and therefore allowed for a fully calibrated measurement of the OAC transfer function.

The measured estimate  $\hat{H}(f)$  of a transfer function  $H(f)$  between two signals  $x(f)$  and  $y(f)$  comes with a statistical error. For an unbiased measurement the normalized rms error  $\epsilon$  in the gain estimate  $|\hat{H}(f)|$  can be calculated via the coherence  $\gamma_{xy}^2$  between the signals and the number of averages  $n_D$  [23, 62]:

$$\epsilon[|\hat{H}(f)|] = \frac{\text{s.d.}[|\hat{H}(f)|]}{|\hat{H}(f)|} = \frac{(1 - \gamma_{xy}^2)^{1/2}}{|\gamma_{xy}| \sqrt{2n_D}} \quad (5.5)$$

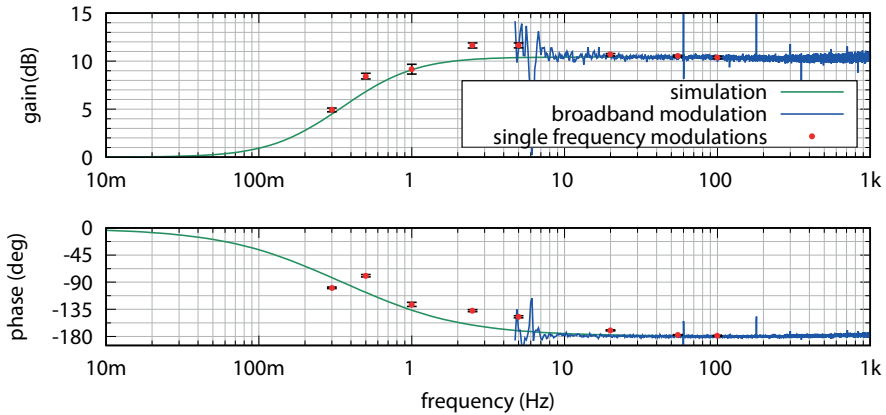


**Figure 5.3:** Measurement of the Optical AC Coupling transfer function at the aLIGO Livingston detector. The broadband modulation measurement for frequencies above 5 Hz is shown in blue. The single frequency modulation measurements are shown in red, together with their corresponding statistical errorbars in black. A theoretical Optical AC Coupling transfer function using the measured Optical AC Coupling gain and the simulated corner frequency is shown in green (Reproduced from [62] © IOP Publishing Ltd. CC BY 3.0.)

The error in the phase estimate of the transfer function  $\hat{\Phi}$  in radians is equal to the standard deviation (s.d.) when  $\epsilon$  is small :

$$\text{s.d.}[\hat{\Phi}] \approx \epsilon[|H(f)|] \quad (5.6)$$

To minimize the statistical error, the coherence between both photodiode signals was monitored in parallel to each transfer function measurement.

A strong coherence could be achieved for the broadband injection, which translated into a statistical error  $\epsilon < 0.125$  dB and  $\text{s.d.}[\hat{\Phi}_{xy}] < 0.8^\circ$ . For the single frequency modulations the modulation coefficient  $m$  as well as the number of averages  $n_D$  was adjusted to yield an error  $\epsilon < 0.1$ .

The error bars shown in Figure 5.3, were calculated with equation 5.5 and 5.6 and therefore represent the statistical error for each single frequency modulation measurement.

### 5.1.3 Results and Simulation

The transfer function measurement derived in this way is presented in Figure 5.3, showing the broadband modulation measurement in blue and the single frequency modulation measurements as red dots.

## 5 Optical AC coupling for gravitational wave detectors

---

An Optical AC coupling gain of 10.43 dB was estimated and the over-coupled design of the coupled cavity becomes evident in the phase behaviour with its characteristic phase flip of  $180^\circ$ .

For comparison results an Optickle [96] simulation of the complete interferometer was performed.

The original Optickle simulation script written by Keiko Kokeyama was adapted with respect to the internal losses of the Fabry-Perot arm resonators measured in [110].

Based on the knowledge of the interferometer the simulation could be used to estimate a corner frequency of  $f_0 = 0.6$  Hz, a DC reduction  $\zeta$ , an impedance matching  $\alpha$ , a mode matching coefficient  $p$  and a theoretical Optical AC coupling gain factor  $g$ .

The measurement of the Optical AC coupling gain factor  $g$  via the transfer function and the independent measurement of the DC reduction  $\zeta$ , allow to estimate another pair of  $\alpha$  and  $p$ , using the equations 3.32 and 3.33. The values for  $\alpha$  and  $p$ , which are calculated in this way, will be referred to as measured values.

These simulated values for  $g$  and  $\zeta$ , as well as the values of the impedance matching  $\alpha$  and mode matching coefficient  $p$  are compared to the measured values in Table 5.1.3).

The simulated values and the values inferred by our measurements are in very close agreement to each other, however, an investigation of the errors for these estimates has not been performed.

We used the corner frequency  $f_0$ , which was estimated with the simulation and the measured Optical AC coupling gain to simulate a theoretical OAC transfer function, shown in Figure 5.3.

The theoretical transfer function derived in this way agrees well with the broadband transfer function measurement for frequencies above 5 Hz. However, for frequencies below 5 Hz the measured data deviates from the predicted OAC transfer function stronger than the derived statistical errors for an unbiased measurement can explain.

### 5.1.4 Discussion

The deviations of the single frequency modulation measurements from the simulated OAC transfer function might be caused by other feedback control loops of the highly complex aLIGO detector.

An example for a control loop, which could influence the transfer function measurement is the differential arm length control loop.

aLIGO is currently operated in the DC readout scheme, therefore the

**Table 5.1:** Power reduction  $\zeta$ , impedance matching  $\alpha$ , non resonant mode content  $p$  and Optical AC Coupling gain  $g$ , derived from the measurements and predicted via simulations

	$\zeta$	$\alpha$	$p$	$g$ (dB)
simulation	0.0147	-0.068	0.01	11.16
measurement	0.01209	-0.050	0.0096	10.43

power level at the output port is used as error signal for the differential arm length degree of freedom. An injected power modulation, which is transferred through the interferometer, would be interpreted as a change of the differential arm length and would induce feedback of the control loop applied to the test masses. This actuation of the differential arm length control loop could then produce additional power modulation in reflection of the coupled cavity.

The performed simulations did not take such couplings into account, even though they have the potential to bias the results of our transfer function measurement. Hence, a closer investigation of power modulations couplings like this should be performed.

Taking into account the work towards an implementation of OAC at GEO 600, which is presented in Section 5.2, an extensive noise characterization of the noise reflected from the power recycling cavity at aLIGO should be performed. Based on the results of this characterization process, potential noise sources will have to be reduced, before further efforts of implementing an OAC based power stabilization feedback control loop should be undertaken.

Due to digital control interface of the power stabilization feedback control loop at aLIGO, an OAC based power stabilization could easily be implemented in parallel to the existing power stabilization feedback control loop and would allow for further testing at aLIGO.

As discussed in Chapter 4.6 an overcoupled OAC power stabilization feedback control loop has yet to be demonstrated and would require additional electronics to induce a phase flip between frequencies below and above the cavity's corner frequency. In a simple implementation the OAC sensor could be primarily used for frequencies above 1 Hz in an (electronically) AC coupled feedback control loop.

### 5.2 Investigations of OAC at GEO 600

GEO 600 is a 600 m long gravitational wave detector, located in Ruthe (Germany), about 20 km away from the AEI in Hannover. The arms of the Michelson Interferometer are folded once, which increases effective arm length to 1.2 km, with the additional benefit of locating the end test masses of the interferometer inside the main building.

Within the course of this thesis measurements similar to the aLIGO measurement described beforehand were performed. Furthermore, first steps towards an implementation of the OAC technique into the power stabilization feedback control loop of GEO 600 are presented.

#### 5.2.1 Optical Layout of GEO 600

A simplified sketch of the optical layout of GEO 600 is shown in Figure 5.4.

GEO 600 uses an Enhanced LIGO 35 W laser system [51, 111], which was installed in 2011 and will be referred to as the eLIGO front-end. The system consists of a 2 W NPRO *Innolight Mephisto*, which is amplified in a solid state amplifier configuration to the final output power of 35 W.

The NPRO is similar to the one described in Chapter 4 and therefore has two actuators for frequency modulation, namely a PZT and a peltier element.

The eLIGO front-end provides two additional amplifiers: an acousto optical modulator, which is used as actuator for the power stabilization feedback control loop and a broadband EOM, which is used as actuator for the frequency stabilization scheme explained in Section 5.2.2.

Directly behind the front-end the beam is transmitted through a remote controlled attenuation stage, which consists of a remote controlled half wave plate and a PBS.

The laser beam passes a resonant EOM (EOM1), which is used to imprint phase modulations required for the frequency stabilization of MC1, before it enters the vacuum envelope. It is coupled through a first suspended mode cleaner cavity called MC1 and passes two resonant EOMs (EOM2 and EOM3), which again imprint phase modulation sidebands. Downstream of the EOMs the beam is coupled through a second suspended mode cleaner, referred to as MC2. Both mode cleaner cavities filter the beam with respect to geometry, fre-

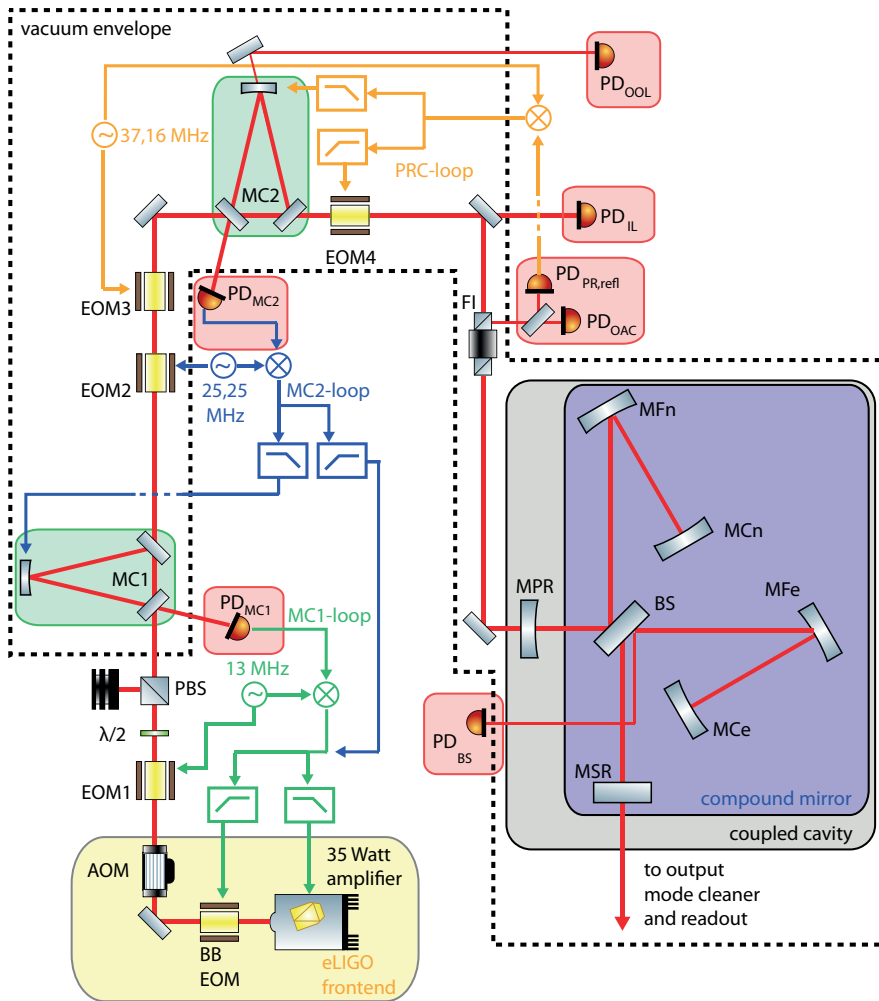


**Figure 5.4:** A simplified version of the GEO 600 optical layout. Several alignment mirrors have been neglected in this sketch, to reduce the number of optical components to a minimum required for understanding the methods described in this section. The sketch therefore includes the optical resonators of GEO 600, the photodiodes for their control, the photodiodes used for the OAC experiments and the coupled cavity formed by the power recycling mirror and the signal recycled Michelson interferometer.

## 5 Optical AC coupling for gravitational wave detectors

---

quency and power fluctuations. The initial design of these mode cleaner cavities can be found in [112], however, the mirrors of the mode cleaners were exchanged in 2012 with mirrors having higher transmissivities to reduce stray-light and radiation pressure effects with the additional benefit of a higher optical throughput[111].

In transmission of MC2 the beam is sent through a Faraday isolator (not shown), a broadband EOM (EOM4) and a Faraday isolator, before it enters the main interferometer through the power recycling mirror MPR.

The interferometric layout of GEO 600 has some differences compared to the aLIGO detectors [15]. Both interferometers use signal and power recycling, but GEO 600 does not employ additional resonators in the interferometer arms. Instead the power recycling cavity has a high Finesse of approximately 3000. To increase the effective arm length of the interferometer the arms are folded with a so called folding mirror (MFn and MFe for the folding mirrors in the north and east arm)[113].

Analog to the aLIGO detector, the Michelson interferometer can be described as a compound mirror with variable reflectivity, which creates a coupled cavity with the power recycling mirror.

The specific optical layout of GEO 600 creates some unique challenges. With the beam splitter, a large transmissive optic is placed into the high gain power recycling cavity. This can lead to strong thermal lensing in the BS and an increased conversion of light from the fundamental mode of the PRC into higher order spatial modes, which in turn can create secondary issues in operating the interferometer.

Several correction and mitigation techniques have been developed [114–116]. Currently, a ring heater is used to change the radius of curvature of the MFe to allow for high power operation.

Every transmissive component, lenses, Faraday isolators, and EOMs can be subject to thermal lensing effects as well [43, 111].

The mode matching optimization between MC2 and the power recycling cavity was intentionally chosen to be ideal for the higher input powers, which are desired in the future operation of the detector [111]. At the current laser power input levels of GEO 600 this results in a mode matching coefficient  $p \approx 0.07$ .

The photodiodes, which are essential for the understanding of the measurements describe in this chapter will shortly be introduced here.

In reflection of both mode cleaner resonators, a dedicated photodiode is used to create error signals for the frequency stabilization described



in Section 5.2.2. A photodiode placed in reflection of the power recycling cavity  $PD_{PR,refl}$  creates the error signal for the PRC. The reflected light is separated from the incoming beam with the Faraday isolator, described earlier.

The in-loop  $PD_{IL}$  and OOL sensor  $PD_{OOL}$  for the power stabilization feedback control loop are placed in transmission of MC2.

To monitor the amount of circulating power inside the power recycling cavity a photodiode  $PD_{BS}$  measures a pick-off beam, created at the beam splitter anti-reflection coating.

A dedicated photodiode  $PD_{OAC}$  was set up during the investigations described in this chapter, which would allow to implement an OAC based power stabilization since it is designed to be compatible with the existing electronic infrastructure.

### 5.2.2 Frequency stabilization

The frequency stabilization scheme of GEO 600 is summarized in this section, following the description in [117].

In first order laser frequency noise does not couple to the readout of a Michelson interferometer if the arm lengths are matched to each other. However, this is not the case at GEO 600, where a length difference referred to as the Schnupp-asymmetry<sup>1</sup> is introduced.

Therefore, the interferometer converts residual frequency noise into power noise at its output and a sufficient suppression of frequency noise becomes necessary.

We will discuss the frequency stabilization scheme with respect to the two mode cleaners and the power recycling cavity, since an understanding of the feedback control loops is required in section 5.2.4. The stabilization of the differential arm length of the Michelson interferometer and the signal recycling cavity will be neglected here due to their minor importance for the further scope of this thesis<sup>2</sup>. The frequency stabilization between laser and power recycling cavity is achieved by achieving resonance stepwise in the first and second mode cleaner and finally in the power recycling cavity:

- In a first step the laser frequency is stabilized to the length of

<sup>1</sup>The Schnupp-asymmetry refers to a mismatch in the length of the interferometer arms, which can be used to create an error signal for the Michelson interferometer [65, 118, 119]

<sup>2</sup>For further information see [117]

## 5 Optical AC coupling for gravitational wave detectors

---

MC1 via the PDH-locking technique, for. EOM1 is used to imprint the necessary phase modulation sidebands at 13 MHz and the error signal is created using the photodiode, which is placed in reflection of MC1 and the correct demodulation. The feedback is applied to the PZT of the seed NPRO for frequencies below 1 kHz and for higher frequencies to the broadband EOM, which is part of the eLIGO front-end.

This part of the frequency stabilization control scheme will be referred to as MC1-control loop and reaches a unity gain frequency of 100 kHz.

- To stabilize the laser frequency to length of the second mode cleaner, phase modulation sidebands are imprinted with EOM2 at 25.25 MHz and the signal is detected in reflection of MC2. To acquire the resonance condition feedback is applied to the length of MC1, by using coil-magnet-actuators at frequencies below 1 kHz.

For frequencies above 1 kHz the feedback signal is added to the feedback signal of the MC1-control loop. This nested control loop will be referred to as MC2-control loop and has a unity gain frequency of 20 kHz. It effectively stabilizes the laser frequency to the length of MC2, which then serves as frequency reference.

- The last step of the frequency stabilization feedback control scheme is to achieve resonance in the power recycling cavity. For this purpose EOM3 is used to imprint phase modulation sidebands at 37.16 MHz and the photodiode  $PD_{PR,refl}$  is used to create a PDH error signal. Feedback is applied to the length of MC2 for frequencies, below 1 kHz via coil-magnet-actuators. For higher frequencies the broadband EOM (EOM4), which is placed in transmission of MC2 is used to change the phase/frequency of the laser light incident to the power recycling cavity. This part of the frequency stabilization control scheme will be referred to as the PRC-control loop and reaches a unity gain frequency of 20 kHz.

### 5.2.3 Transfer function measurement and calibration

To measure the OAC transfer function at the GEO 600 detector, a swept sine amplitude modulation was injected with a FFT analyzer

(Type: *HP 35670A*) into a dedicated injection input of the amplitude stabilization feedback control loop. In contrast to the aLIGO measurements it was feasible to measure with a swept sine modulation over the full frequency range, since the frequencies of interest are significantly higher due to the linewidth of about 20 Hz of the coupled cavity, formed by the power recycling mirror and interferometer.

### Estimation of the coupled cavity corner frequency

Before the OAC transfer function measurement, the corner frequency of the coupled cavity was estimated by measuring the transfer function of the coupled cavity according to Equation 2.37, which relates the incoming modulations to the resonator internal modulations.

This measurement is analog to an OAC transfer function, however, instead of using a photodiode in reflection of the coupled cavity, a photodiode measuring the resonator internal modulations is required. The sensor for the amplitude modulations incident to the PRC was provided by the out-of-loop sensor of the power stabilization feedback control loop  $PD_{OOL}$ , which is placed in transmission of the second mode cleaner.

At GEO 600 the circulating power inside of the coupled cavity is continuously monitored with a dedicated photodiode  $PD_{BS}$ . This photodiode measures a pick-off beam, which is created at the imperfect anti-reflection coating of the interferometer beam splitter. The transfer function measurement is shown for two different input powers in Figure 5.5).

The corner frequency could then be estimated for the different input powers of the interferometer and showed only minor deviances from  $f_0 = 19.8$  Hz. To simplify the fitting of the OAC transfer function measurements later, this corner frequency was fixed to make the OAC gain parameter  $g$  the only fit parameter.

### Measurement of the OAC transfer function

Measuring an OAC transfer function always requires two photodiodes to measure incoming and reflected power modulations. The incoming light was measured again with the OOL detector  $PD_{OOL}$ , while the reflected power modulation was measured with the  $PD_{PR,refl}$ , which is the sensor used to create an error signal for the power recycling cavity frequency stabilization feedback control loop.

## 5 Optical AC coupling for gravitational wave detectors

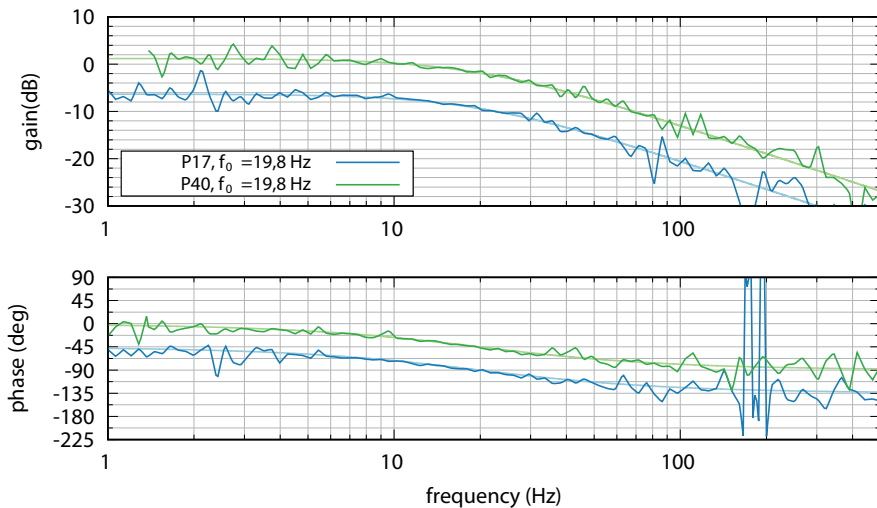


**Figure 5.5:** Measurement and fit of the coupled cavity corner frequency for two different input powers. Since both measurements yield very similar results, the curve for P40 is shifted by 6 dB and  $45^\circ$  for better visibility. The curves fitted to the measurements point to a corner frequency  $f_0 = 19.8$  Hz

To account for any optical or electronic gain differences between both photodiode a transfer function between the two photodiodes was measured with a misaligned Michelson interferometer. In this situation, the light is completely reflected by the power recycling mirror MPR and a precise measurement between both photodiodes can be performed. Since both photodiodes are placed downstream of the power attenuation stage, which is used to control the total input power of the interferometer, both photodiodes will be affected equally by different interferometer input powers. Hence, this transfer function can than be used to normalize the OAC transfer function measurements for the all input powers.

As stated earlier, the mode matching of the power recycling cavity is optimized for higher input powers than currently injected into the interferometer. Therefore, the mode matching coefficient  $p$  is expected to become smaller for higher input powers of the interferometer, which should then result in different OAC gain factors  $g$  (see Section 3.3). A higher input power, however, leads to a stronger thermal lens in the interferometer beam splitter as well, which can increase the amount of higher order TEM modes inside the interferometer[116]. The excitation of higher order modes inside the interferometer is an additional loss channel and can change the impedance matching of the power

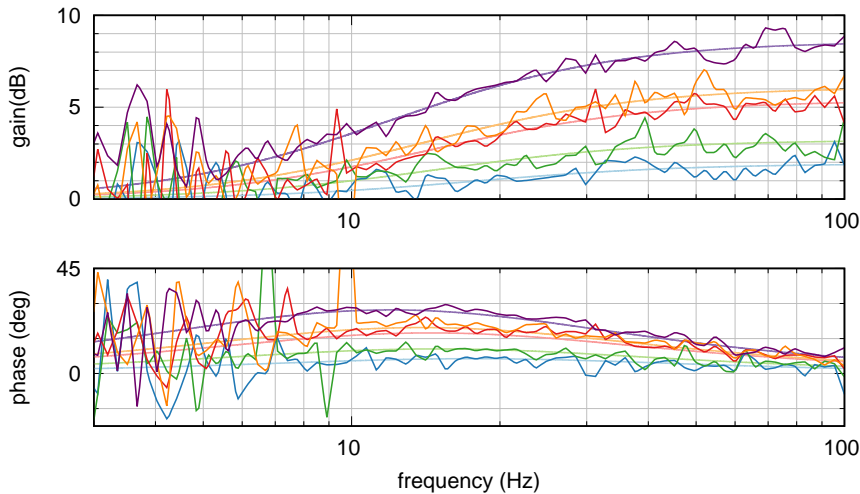


**Figure 5.6:** OAC transfer functions measured at GEO 600 for different input power level, with and without thermal compensation applied by the ring heater (indicated by the letter c). The best fit is shown together with each measurement in a lighter color. The legend gives the value for the single fit parameter  $g$

recycling cavity.

Hence the OAC transfer function was measured for different input powers. The interferometer was locked in the robust heterodyne-readout to avoid lock losses and the output mode cleaner was unlocked [111, 120, 121].

The ring heater at the folding mirror was used to compensate for the thermal lens in the beam splitter for the higher input powers P40 and P60<sup>3</sup>. The optimization process is routinely performed by minimizing the optical power leaving towards the dark port of the interferometer, which is the standard figure of merit used by GEO 600 so far.

### Results and parameter estimation

Figure 5.6 shows the optical AC coupling transfer function measurements acquired at the GEO 600 detector for different input powers and different compensation levels applied with the ring heater<sup>4</sup>. Us-

<sup>3</sup>The ring heater compensation for P60 was set to the the optimal setting for P40 as well, for technical reasons

<sup>4</sup>The transfer function measurements are noisy, compared to the transfer function measurements performed in the laboratory experiment (see Section 4.4.1),

## 5 Optical AC coupling for gravitational wave detectors

---

ing Equation 3.12 OAC transfer function were fitted to the data to estimate the Optical AC coupling gain factor  $g$ .

The Optical AC coupling gain factor increased for higher input powers of the interferometer. An additional improvement of the OAC gain factor was achieved by the ring heater compensation for the higher input powers as described above.

It is possible to estimate the mode matching parameter  $p$  and the impedance matching  $\alpha$  with the equations 3.32 and 3.33, if the DC reduction  $\zeta$  is measured in parallel for each lock stretch.

The measured values for  $\zeta$  and the OAC gain  $g$  are presented with the estimates for  $p$  and  $\alpha$  in Table 5.2.3.

As expected the estimated mode matching coefficients are smaller for higher input power. At the same time the impedance matching changes to higher values of  $\alpha$ , which indicates a stronger undercoupled situation for higher input powers.

The change in impedance matching then becomes beneficial to the achievable gain of the OAC transfer function measurement, as illustrated in Figure 5.7. This plot is equivalent to Figure 3.3, and shows the achievable OAC gain for the different mode matching values  $p$  from table 5.2.3 in dependence of the impedance matching.

Reaching the optimum OAC gain factor  $g$  for the estimated mode matching coefficients at all power levels would require stronger undercoupling of the coupled cavity. This is even more pronounced for the lower input powers.

Another interesting aspect can be found by looking at the fitted parameters for the compensated and uncompensated P40 measurements. As indicated by the estimated impedance matching values the losses inside the interferometer increased for the compensated situation, which is the opposite of what is desired for an ideal use of the thermal compensation.

This in turn would question suitability of the total optical power at the dark port as the figure of merit for the optimization of the ring heater compensation.

To judge if this indicated trend is significant the errors of these estimations have to be evaluated.

---

which might be attributed to the high excess power noise in reflection of the power recycling cavity (see Section 5.2.4)

**Table 5.2:** Power reduction  $\zeta$ , impedance matching  $\alpha$ , non resonant mode content  $p$  and Optical AC Coupling gain  $g$ , derived from the measurements and predicted via simulations

state	input power	$\zeta$	$\alpha$	$p$	$g$ (dB)
P17	1.4 W	0.072	0.02	0.072	1.93
P25	2 W	0.07	0.035	0.069	3.23
P40	3.2 W	0.057	0.053	0.054	5.35
P40c	3.2 W	0.058	0.067	0.054	6.11
P60c	4.8 W	0.07	0.145	0.050	8.58

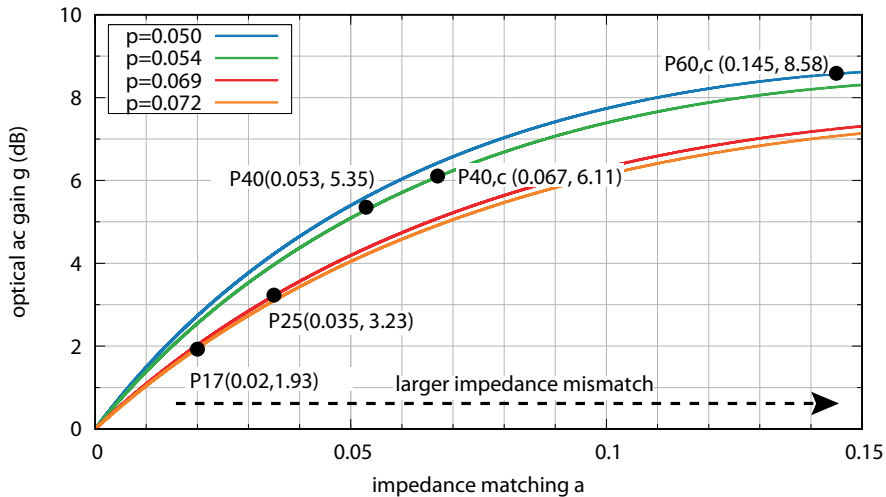


**Figure 5.7:** Estimated impedance matching and Optical AC coupling gain on gain curves for different mode matchings coefficients  $p$ . These curves are equivalent to Figure 3.3 and each curve shows the dependence of the OAC gain factor  $g$  from the impedance matching for a fixed mode matching coefficients  $p$ . For every estimated mode matching coefficient of the coupled cavity of GEO 600 the OAC gain factor  $g$  could, in principle be increased by a bigger impedance mismatch.

### Error estimates

If  $\mathbf{a}$  and  $\mathbf{p}$  are estimated using the equations 3.32 and 3.33 , it is straightforward to estimate the error in those estimations, depending on the uncertainties in measuring  $\zeta$  and  $g$ : First the partial derivatives of  $\mathbf{p}(\zeta, g)$  and  $\mathbf{a}(\zeta, g)$ , with respect to  $g$  and  $\zeta$  are determined:

$$p_\zeta = \frac{\partial}{\partial \zeta} \mathbf{p}(\zeta, g) = \frac{1 + 2g^3 \zeta^2 - g^2 \zeta (2 + \zeta)}{((2g - 1)\zeta - 1)^2} \quad (5.7)$$

$$p_g = \frac{\partial}{\partial g} \mathbf{p}(\zeta, g) = \frac{2(g - 1)\zeta^2 (g\zeta - 1)}{((2g - 1)\zeta - 1)^2} \quad (5.8)$$

$$a_\zeta = \frac{\partial}{\partial \zeta} \mathbf{a}(\zeta, g) = \frac{g - 1}{(g\zeta - 1)^2} \quad (5.9)$$

$$a_g = \frac{\partial}{\partial g} \mathbf{a}(\zeta, g) = -\frac{(\zeta - 1)\zeta}{(g\zeta - 1)^2} \quad (5.10)$$

The estimate of the error  $\Delta \mathbf{p}(\zeta, g, \Delta \zeta, \Delta g)$  and  $\Delta \mathbf{a}(\zeta, g, \Delta \zeta, \Delta g)$ , then depends on the uncertainties in the measurement of  $\zeta$  and  $g$ :

$$\Delta \mathbf{p} = \sqrt{(p_\zeta \cdot \Delta \zeta)^2 + (p_g \cdot \Delta g)^2} \quad (5.11)$$

$$\Delta \mathbf{a} = \sqrt{(a_\zeta \cdot \Delta \zeta)^2 + (a_g \cdot \Delta g)^2} \quad (5.12)$$

An exact determination of the uncertainties  $\Delta \zeta$  and  $\Delta g$  is difficult to obtain. Hence a coarse estimation for these errors is presented.

In the case of the uncertainty  $\Delta g$  we can for instance calculate the difference between each measurement point  $g_{\text{data}}(f_n)$  and the according fit value  $g_{\text{fit}}(f_n)$  to calculate a value comparable to a standart deviation.

$$\Delta g_{\text{sd}} = \sqrt{\frac{\sum_{\mathbf{N}} (g_{\text{data}}(f_n) - g_{\text{fit}}(f_n))^2}{\mathbf{N}}} \quad (5.13)$$

This procedure was performed for every transfer function measurement and a resulting error contribution was estimated.

The FFT analyzer (Type: *HP 35670A*) has a defined measurement uncertainty of  $g_{\text{meas}} = 0.4$  dB, which contributes to the measurement errors [122]. Furthermore, we assume an uncertainty  $\Delta \zeta = 0.01$  in the estimation of the DC reduction at a gravitational wave detector.

The individual contributions and the total resulting errors for the estimates of  $\mathbf{p}$  and  $\mathbf{a}$  are shown in Table 5.2.3 and 5.2.3, respectively.



**Table 5.3:** Errors for mode matching estimates. The error for the mode matching is dominated by the uncertainty in the power reduction measurement  $\zeta$

	$p_g \cdot \Delta g_{sd}$	$p_g \cdot \Delta g_{meas}$	$p_\zeta \cdot 0.01$	$p \pm \Delta p$
P17	0.00002	0.00002	0.0099	$0.072 \pm 0.099$
P25	0.00012	0.00003	0.0096	$0.069 \pm 0.096$
P40	0.00016	0.00034	0.0089	$0.054 \pm 0.09$
P40c	0.00009	0.00005	0.0084	$0.054 \pm 0.084$
P60c	0.00789	0.00083	0.0031	$0.05 \pm 0.038$

**Table 5.4:** Errors for impedance matching estimates. The error for the impedance matching is dominated by the uncertainty in the power reduction measurement  $\zeta$

	$a_g \cdot \Delta g_{sd}$	$a_g \cdot \Delta g_{meas}$	$a_\zeta \cdot 0.01$	$a \pm \Delta a$
P17	0.0005	0.0005	0.0030	$0.02 \pm 0.0031$
P25	0.0019	0.0006	0.0056	$0.035 \pm 0.006$
P40	0.0015	0.0006	0.0105	$0.053 \pm 0.011$
P40c	0.0007	0.0007	0.0130	$0.067 \pm 0.013$
P60c	0.0079	0.0012	0.0255	$0.145 \pm 0.027$

The errors are dominated by the uncertainty in the estimation of the power reduction in reflection of the coupled cavity. With the current total error estimates a final statement about the suitability of the total dark port power as figure of merit can not be fully resolved. However, a better estimate of the power reduction  $\zeta$  would allow to get more insight about this issue.

### 5.2.4 Towards an implementation into power stabilization feedback control scheme

The first experiments towards the implementation of an OAC based power stabilization feedback control loop were conducted within this thesis.

As a precursor to these experiments a dedicated new photodiode, referred to as  $PD_{OAC}$  (see Figure 5.4), compatible with the electronics of the power stabilization feedback control loop was installed in the reflection path of the power recycling cavity. The photodiode was optimized to detect a photocurrent of 0.3 mA, which is equivalent to a

## 5 Optical AC coupling for gravitational wave detectors

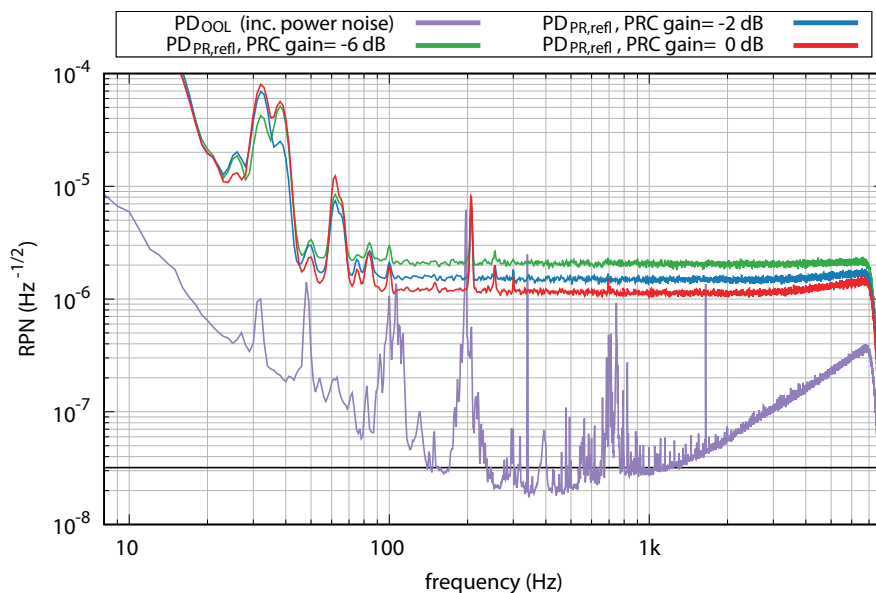


**Figure 5.8:** Excess relative power noise measured in reflection of the locked GEO 600 detector for different PRC-gain settings. Compared to the standard gain setting (0 dB) the excess noise increases for reduced gain settings.

shot noise level of  $3.2 \cdot 10^{-8} \text{ Hz}^{-1/2}$ .

It was characterized with an unlocked and misaligned interferometer by using  $\text{PD}_{\text{OAC}}$  as in-loop sensor for the power stabilization feedback control loop. The out of loop performance seen by  $\text{PD}_{\text{OOL}}$  was comparable to the normal in-loop photodiode  $\text{PD}_{\text{IL}}$  of the power stabilization feedback control loop, despite the different relative shot noise level.

The OOL power noise of an OAC based power stabilization feedback control loop using the OAC photodiode should increase in the shot noise limited regions.

However, using the OAC photodiode as an in-loop sensor with a locked interferometer resulted in a highly unstable power stabilization feedback control loop.

Further investigations revealed an increased level of relative power noise detected by  $\text{PD}_{\text{OAC}}$  with a locked interferometer. The relative excess power noise level was approximately  $1 \cdot 10^{-6} \text{ Hz}^{-1/2}$  and could also be detected with the  $\text{PD}_{\text{PR,refl}}$ . An additional coherence measurement between both photodiodes confirmed that both photodiodes were detecting exactly the same noise.

As the conversion of frequency noise to power noise has been a major noise contribution in every OAC experiment so far, a logical next step was to check for a connection between the excess noise and the remaining frequency noise.

An easy approach to observe the excess power noise for different levels of frequency noise is to change the gain of the power recycling frequency control loop (see Section 5.2.2). Since this feedback control loop already operates at its stability margin, the only possible adjustment is a gain reduction.

Reducing the PRC-gain resulted into an increased excess relative power noise, measured in reflection of the PRC with  $PD_{OAC}$  and  $PD_{PR,refl}$ , see Figure 5.8<sup>5</sup>. The relative excess power noise is shown for different settings of the PRC gain, 0 dB is the standard gain setting used at GEO 600<sup>6</sup>.

As a further reference Figure 5.8 and Figure 5.9 show the relative power noise, which is incident to the power recycling cavity and measured by  $PD_{OOL}$ . The relative shot noise level of  $PD_{OAC}$  is shown to illustrate the distance between the excess noise, and the relative power stability, which was targeted for the first OAC based power stabilization experiment.

An alternative way to influence the remaining frequency noise is to change the gain of the frequency control loop, which stabilizes the laser frequency to the length of MC2. Since the loop is nested this can be achieved by changing the MC1-gain, which affects the locking of the laser to the length of MC1, which in turn is stabilized to the length of MC2.

This loop also operated close to instability and an increase of the gain required to upgrade the electronics with faster operational amplifiers. The upgraded electronics helped to increase the loop gain by 5.1 dB for all frequencies, and reaching a unity gain frequency of about 160 kHz instead of 100 kHz.

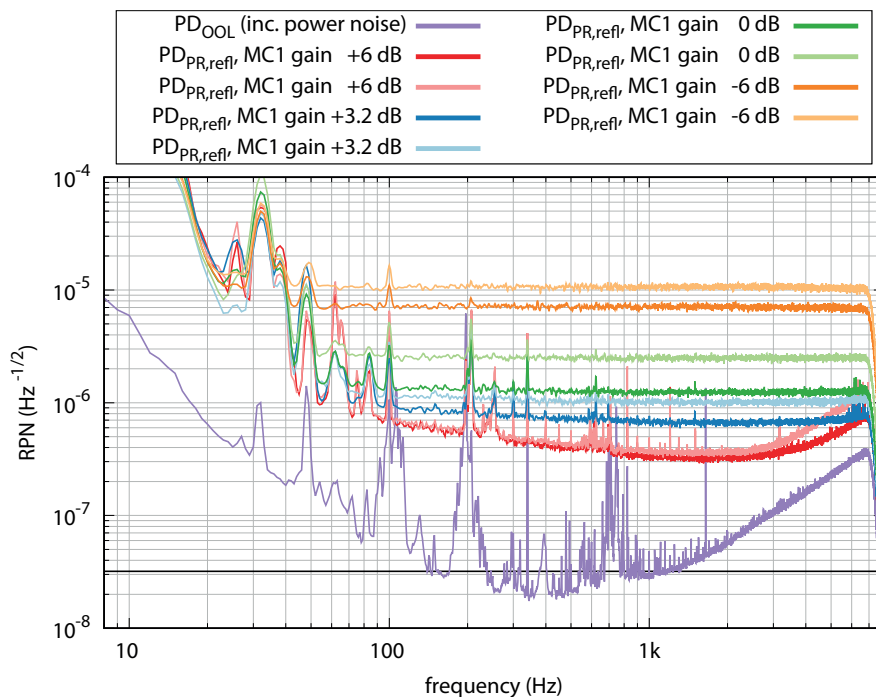
A further increase of the bandwidth would require significant changes especially to the high voltage electronics used to drive of the broad-band EOM of this control loop.

Figure 5.9 shows the noise curves for two different gain settings in the frequency stabilization feedback control loop. As reference level (0 dB) serves the standard gain setting of the control loop, prior to

<sup>5</sup>The presented measurements were performed using  $PD_{PR,refl}$ . However, measurements with  $PD_{OAC}$  showed exactly the same excess noise.

<sup>6</sup>The standard PRC-gain setting in the digital control interface for 0 dB is 200

## 5 Optical AC coupling for gravitational wave detectors



**Figure 5.9:** Excess relative power noise measured in reflection of the locked GEO 600 detector for different MC1 gains. The excess power noise increases for a gain reduction of 3.2 dB. Due to the improvements of the standard gain setting (0 dB), could be increased by up to 6 dB resulting into a reduces excess power noise. The excess power noise in reflection of the PRC is significantly above the OOL power noise, which is injected into the PRC

the upgrades of the electronics<sup>7</sup>. Two measurements are shown for each gain setting to reflect the fluctuating nature of the excess noise. The cause of this fluctuation could be attributed to different frequency noise levels for the different measurement times.

Note that the excess power noise is not equally influenced by the gain of the MC1-loop for all frequencies. At frequencies below 100 Hz another noise source seems to be dominating and will also require further investigation.

It can be stated that a reduction of the loop gain by 6 dB let to a significant increase of excess power noise in reflection of the power recycling cavity, while an increase of the gain resulted in a reduction of excess noise.

<sup>7</sup>The standard MC1-gain setting in the digital control interface for 0 dB is 110

### 5.2.5 Discussion

The initial design for the Optical AC coupling based power stabilization feedback control loop implementation at GEO 600 will require a reduction of the excess power noise in reflection of the PRC by at least a factor of 40 at a frequency of 400 Hz.

Therefore, a thorough investigation of the noise sources in reflection of the PRC has to be performed, which also needs to distinguish these noise sources into conventional sensor noise and OAC sensor noise. A crucial part of this investigation will be the understanding and reduction of the frequency noise dependent excess noise, which was found to be the limiting noise contribution for frequencies above 100 Hz.

At the current stage the exact coupling mechanism is not fully explained. However, coherence measurements between the reflected power noise and the error point of the PRC-loop suggest a non-linear down-conversion process, which converts frequency noise between 50 kHz and 150 kHz to lower frequencies and thereby produces the white noise spectrum observed in reflection of the PRC [123]. Triggered by the excess noise observed in the presented measurements, the intra-cavity power noise was found to also be affected by excess power noise for a reduced PRC gain. A numerical time domain model, which used the calibrated frequency noise spectra from the error point of the PRC-control loop, could already reproduce the shape of the excess intra-cavity noise. However, the exact size of the excess noise could not be projected yet[123].

While the work on better estimates and understanding of the conversion process continues, a further reduction of the frequency noise conversion could potentially be achieved by further optimization of the MC1-loop open loop gain shape. Potentially a further increase in the bandwidth of this control loop could be achieved with an upgrade of the high voltage electronics driving the broadband EOM. This would lead to a better noise suppression at high frequencies and a reduction of the down-conversion process described above.

It should be noted that remaining frequency noise could also be further suppressed by mode cleaner resonators with higher Finesse and therefore better frequency noise filtering. However, due to the high complexity involved in changing the input optics, and the drawbacks, which triggered the implementation of the new input optics in 2012 (see Section 5.2.1), other measures appear better suited as initial measures to deal with the conversion.

The further reduction of this excess noise contribution will then al-

low for the investigation of other potential sensor noise sources, with possible candidates being stray-light effects, beam pointing conversion or higher order spatial mode excitations (see also Section 3.5 and [22]).

### 5.3 Chapter Summary

Within the scope of this thesis Optical AC coupling has been investigated at large scale gravitational wave detectors for the first time.

The transfer function measurement performed at aLIGO Livingston agrees well with the estimates inferred from numerical simulations. However, some deviations between theory and measurement at low frequencies could not be explained by statistical errors and therefore will need to be further investigated. An OAC gain factor of  $g = 10.47$  dB was measured, which could potentially increase the performance of a shot noise limited power stabilization feedback control loop in the same manner as an increase of the detected photocurrent by a factor of 11.

The transfer function measurements at GEO 600 were used to determine OAC gain factors between  $g = 1.93$  dB and  $g = 8.6$  dB, depending on the input power of the interferometer and the thermal compensation of the beam splitter thermal lens. An increasing OAC gain factor  $g$  for higher input powers, was explained by a better mode matching coefficient  $p$  and increased losses within the interferometer. The estimated impedance matching after the ring heater optimization process indicated increased losses inside the interferometer. However, the estimate errors for the impedance matching could not fully validate this tendency and therefore a closer investigation should be performed.

A new sensor for a potential implementation of an OAC based power stabilization feedback control loop was installed but a beneficial use of an OAC power stabilization feedback control loop was prevented by excess power noise in reflection of the coupled cavity.

This excess noise is believed to be caused by down conversion of frequency noise from the frequency band between 50 kHz and 150 kHz. Further suppression of this excess noise is required to get more insight about additional sensor noise sources for an OAC based power stabilization feedback control loop, which could be masked in the current excess noise.

# 6

## Chapter 6

### Summary

Within the scope of this thesis the Optical AC coupling technique has been investigated at the aLIGO Livingston detector at frequencies between 0.3 Hz and 1 kHz, at GEO 600 for frequencies between 1 Hz and 8 kHz and in a dedicated laboratory experiment for frequencies between 100 Hz and 60 kHz.

The main project of this thesis was the design and construction of a dedicated laboratory experiment, which allows to investigate Optical AC coupling for frequencies below 4 kHz. A major motivation was the investigation of potential low frequency sensor noise sources attributed to the OAC technique, which could not be analyzed in previous experiments.

The core component of the new experiment is a linear optical resonator with a corner frequency of 2 kHz and tunable impedance matching. To decouple the crucial components of the experiment from acoustics, the OAC-resonator and the photodiodes used for stabilization experiments were placed inside a vacuum tank, which can be evacuated to pressure levels below 10 mbar.

Based on the knowledge gathered in earlier experiments, it was possible to avoid major noise sources which limited earlier experiments and to set up an Optical AC coupling based power stabilization feedback control loop with a significantly improved performance at low frequencies. An Optical AC coupling gain of up to 10 dB was reached, which was mainly limited by an imperfect mode matching between laser and resonator. The maximum relative power stability of  $8 \cdot 10^{-9} \text{ Hz}^{-1/2}$  was reached at a frequency of 20 kHz with a detected photocurrent of  $i_D = 1 \text{ mA}$ . Limitations in the out-of-loop performance of the

## 6 Summary

---

new setup was explained with known noise contributions, except for a single, yet not understood noise source at frequencies below 2 kHz. Further investigation into the origin of this noise source is required.

First investigations towards the possible implementations of the OAC technique at large scale gravitational wave detectors were presented. An Optical AC coupling transfer function of the coupled cavity of the aLIGO detector was measured for the first time and compared with numerical simulations of the interferometer. The measurements are in close agreement to the numerical simulations and show an OAC gain of 10.47 dB.

Similar measurements were performed at the GEO 600 detector. The optical AC coupling transfer function was measured for different mode matching coefficients and different settings for the compensations of the thermal lens in the main beam splitter. These measurements demonstrated Optical AC coupling gain factors up to 8.6 dB. An implementation of the Optical AC coupling technique in the power stabilization feedback control loop of GEO 600 was prevented by excess power noise in reflection of the power recycling cavity. This excess noise was attributed to a non-linear coupling process converting frequency noise from the frequency band between 50 kHz and 150 kHz to power noise at frequencies below 8 kHz. Upgrades to the existing frequency stabilization control scheme led to a reduced noise coupling and therefore further upgrades are considered to be beneficial.

In conclusion, the laboratory experiment tested an Optical AC coupling based power stabilization scheme with previously unattained sensitivity at low frequencies. Optical AC coupling transfer functions were measured at large scale gravitational wave detectors for the first time and the first steps towards the implementation of OAC at a GEO 600 were performed. However, further noise analysis of the power noise reflected from the coupled cavity of gravitational wave detectors is essential before such an implementation can become beneficial.



## Bibliography

- [1] P. Yun, F. Tricot, C. E. Calosso, S. Micalizio, B. François, R. Boudot, S. Guérandel and E. de Clercq, *High-Performance Coherent Population Trapping Clock with Polarization Modulation*, Physical Review Applied **7**, (2017). 1
- [2] J. Vanier, *Atomic clocks based on coherent population trapping: a review*, Applied Physics B **81**, 421 (2005). 1
- [3] A. D. Brandt, S. F. Cooper, Z. Burkley and D. C. Yost, *Reduced phase noise in an erbium frequency comb via intensity noise suppression*, Opt. Express **25**, 18175 (2017). 1
- [4] W. Liang, D. Eliyahu, V. S. Ilchenko, A. A. Savchenkov, A. B. Matsko, D. Seidel and L. Maleki, *High spectral purity Kerr frequency comb radio frequency photonic oscillator*, Nature Communications **6**, 7957 (2015). 1
- [5] G. Ranjit, M. Cunningham, K. Casey and A. A. Geraci, *Zep- tonewton force sensing with nanospheres in an optical lattice*, Physical Review A **93**, (2016). 1
- [6] G. Zhao, W. Tan, M. Jia, J. Hou, W. Ma, L. Dong, L. Zhang, X. Feng, X. Wu, W. Yin, L. Xiao, O. Axner and S. Jia, *Intensity-Stabilized Fast-Scanned Direct Absorption Spectroscopy Instrumentation Based on a Distributed Feedback Laser with Detection Sensitivity down to  $4 \times 10^{-6}$* , Sensors **16**, 1544 (2016). 1
- [7] H. Kaufer, *Opto-mechanics in a Michelson-Sagnac Interferometer*, PhD Thesis, QUEST-Leibniz-Forschungsschule der Gottfried Wilhelm Leibniz Universität Hannover, 2104. 1
- [8] A. Einstein, *Die Grundlage der allgemeinen Relativitätstheorie*, Annalen der Physik **354**, 769 (1916). 1
- [9] B. Abbott, the LIGO Scientific Collaboration and the Virgo Collaboration, *GW151226: Observation of Gravitational Waves*

## BIBLIOGRAPHY

---

- from a 22-Solar-Mass Binary Black Hole Coalescence*, Physical Review Letters **116**, (2016). 1, 83
- [10] A. Abramovici, W. E. Althouse, R. W. P. Drever, Y. Gursel, S. Kawamura, F. J. Raab, D. Shoemaker, L. Sievers, R. E. Spero, K. S. Thorne, R. E. Vogt, R. Weiss, S. E. Whitcomb and M. E. Zucker, *LIGO: The Laser Interferometer Gravitational-Wave Observatory*, Science **256**, 325 (1992). 1
- [11] G. M. Harry and the LIGO Scientific Collaboration, *Advanced LIGO: the next generation of gravitational wave detectors*, Classical and Quantum Gravity **27**, 084006 (2010). 1, 59
- [12] T. F. Acernese, *Advanced Virgo Baseline Design*, VIR-0027A-09 (2009). 1
- [13] F. Acernese and the Virgo Collaboration, *Advanced Virgo: a second-generation interferometric gravitational wave detector*, Classical and Quantum Gravity **32**, 024001 (2015). 1
- [14] H. Lueck and The GEO600 project, Classical and Quantum Gravity **14**, 1471 (1997). 1
- [15] B. Willke et al., *The GEO 600 gravitational wave detector*, Classical and Quantum Gravity **19**, 1337 (2002). 1, 94
- [16] B. Willke, P. King, R. Savage and P. Fritschel, Pre-Stabilized Laser Design Requirements, LIGO DCC, 2011. 2, 24
- [17] M. Planck, *Ueber das Gesetz der Energieverteilung im Normalspectrum*, Annalen der Physik **309**, 553 (1901). 2
- [18] P. Kwee, B. Willke and K. Danzmann, *Shot-noise-limited laser power stabilization with a high-power photodiode array*, Opt. Lett. **34**, 2912 (2009). 2, 24
- [19] P. Kwee, B. Willke and K. Danzmann, *Optical ac coupling to overcome limitations in the detection of optical power fluctuations*, Opt. Lett. **33**, 1509 (2008). 2, 27
- [20] P. Kwee, B. Willke and K. Danzmann, *Laser power noise detection at the quantum-noise limit of 32 A photocurrent*, Optics Letters **36**, 3563 (2011). 2

- [21] P. Kwee, B. Willke and K. Danzmann, *Laser power stabilization using optical ac coupling and its quantum and technical limits*, Appl. Opt. **48**, 5423 (2009). 2, 30, 42
- [22] P. Kwee, *Laser Characterization and Stabilization for Precision Interferometry*, PhD Thesis, Leibniz Universitaet Hannover, 2010, <http://www.patrick-kwee.de/thesis/thesis-kwee-diss.pdf>. 3, 7, 11, 12, 29, 30, 32, 39, 42, 44, 47, 51, 108
- [23] Julius S. Bendat and Allan G. Piersol, *Random Data: Analysis and Measurement Procedures* (Wiley, 2000). 6, 7, 8, 88
- [24] A. E. Siegman, *Lasers* (University Science Books, Mill Valley, 1986). 7, 14, 16
- [25] B. E. Saleh and M. C. Teich, *Fundamentals of Photonics* (John Wiley and Sons.Inc., New York, 1991), Vol. 1. 7, 14
- [26] F. Riehle, *Frequency Standards* (Wiley-VCH, 2006). 8
- [27] F. Seifert, *Power Stabilization of High Power Lasers for Second Generation Gravitational Wave Detectors*, Dissertation, Leibniz Universitaet Hannover, 2010. 8, 12, 21, 22, 24
- [28] P. R. Saulson, *Fundamentals of interferometric Gravitational Wave Detectors* (World Scientific Publishing Company, 1994). 8
- [29] R. Blackman and J.W. Tukey, *The Measurement of Power spectral* (Dover Publications, Inc. New York, 1958).
- [30] P. Stoica and R. L. Moses, *Spectral Analysis of Signals* (Pearson Prentice Hall, 2005). 8
- [31] L. N. Binh, *Optical Modulation* (CRC Press, 2017). 8
- [32] R. Paschotta, *Noise in Laser Technology*, Optik & Photonik **4**, 48 (2009). 8
- [33] M. D. Kochanczyk, T. F. Bartsch, K. M. Taute and E.-L. Florin, in *Optical Trapping and Optical Micromanipulation IX*, edited by K. Dholakia and G. C. Spalding (SPIE, 2012). 8
- [34] A. Freise and K. Strain, *Interferometer Techniques for Gravitational-Wave Detection*, Living Reviews in Relativity **13**, 1 (2010). 8, 9, 14, 39

## BIBLIOGRAPHY

---

- [35] S. Chelkowski, H. Vahlbruch, B. Hage, A. Franzen, N. Lastzka, K. Danzmann and R. Schnabel, *Experimental characterization of frequency-dependent squeezed light*, Phys. Rev. A **71**, 013806 (2005). 9, 83
- [36] M. Lawrence, B. Willke, M. E. Husman, E. K. Gustafson and R. L. Byer, *Dynamic response of a Fabry-Perot interferometer*, J Opt Soc Am B **16**, 523 (1999). 8, 64
- [37] T. C. R. Hans-Albert Bachor, *A Guide to Experiments in Quantum Optics* (Wiley VCH Verlag GmbH, 2004). 12
- [38] C. Gerry and P. Knight, *Introductory Quantum Optics* (Cambridge University Press, 2004).
- [39] H. Vahlbruch, *Squeezed light for gravitational wave astronomy*, PhD Thesis, Leibniz Universität Hannover, 2008. 12
- [40] B. Willke, S. Brozek, K. Danzmann, V. Quetschke and S. Gossler, *Frequency stabilization of a monolithic Nd:YAG ring laser by controlling the power of the laser-diode pump source*, Opt. Lett. **25**, 1019 (2000). 12
- [41] M. Heurs, *Gravitational waves in a new light: Novel stabilization schemes for solid-state lasers*, PhD Thesis, Universität Hannover, 2004. 12
- [42] B. W. Barr, K. A. Strain and C. J. Killow, *Laser amplitude stabilization for advanced interferometric gravitational wave detectors*, Classical and Quantum Gravity **22**, 4279 (2005). 12, 24
- [43] C. Bogan, *Stabilized High Power Lasers and Spatial Mode Conversion*, PhD Thesis, Leibniz Universität Hannover, 2013. 13, 84, 94
- [44] J. Rollins, D. Ottaway, M. Zucker, R. Weiss and R. Abbott, *Solid-state laser intensity stabilization at the 10<sup>-8</sup> level*, Opt. Lett. **29**, 1876 (2004). 13, 24
- [45] F. Seifert, P. Kwee, M. Heurs, B. Willke and K. Danzmann, *Laser power stabilization for second-generation gravitational wave detectors*, Opt. Lett. **31**, 2000 (2006). 13, 24

- [46] B. Willke, P.J.King, N.Uehara, E.K.Gustafson, R. Byer, S.U.Seel and J. R.L.Savage, *Spatial and Temporal filtering of a 10-W Nd:YAG laser with a Fabry-Pero ring-cavity premode cleaner*, Optics Letters **23**, (1998). 13
- [47] T. B. Márk Csörnyei and T. Marozsák, *All-optical intensity noise suppression for solid-state and semiconductor lasers*, Journal of Telecommunications and Information Technology **65** (2005). 13
- [48] S. Saraf, K. Urbanek, R. L. Byer and P. J. King, *Quantum noise measurements in a continuous-wave laser-diode-pumped Nd:YAG saturated amplifier*, Opt. Lett. **30**, 1195 (2005). 13
- [49] J. Freeman and J.Conradi, *Gain modulation response of erbium-doped fiber amplifiers*, IEEE Photonics Technology Letters **5**, 224 (1993).
- [50] S. Novak and A. Moesle, *Analytic Model for Gain Modulation in EDFAs*, J. Lightwave Technol. **20**, 975 (2002).
- [51] M. Frede, B. Schulz, R. Wilhelm, P. Kwee, F. Seifert, B. Willke and D. Kracht, *Fundamental mode, single-frequency laser amplifier for gravitational wave detectors*, Opt. Express **15**, 459 (2007). 13, 92
- [52] T. K. Ishii and B. A. Capek, *Transfer function of parallel plate resonators*, Mathematical Modelling **4**, 523 (1983). 14
- [53] T.W.Hänsch and B.Couillaud, *Laser Frequency Stabilization by Polarization Spectroscopy of a Reflecting Reference Cavity*, Optics Communications **35**, (1980). 18
- [54] D.Shaddock, *Advanced Interferometry for Gravitational Wave Detection*, Dissertation, Australian National University, 2000.
- [55] D. Shaddock, M.B.Gray and D.E.Melellad, *Frequency Locking a laser to an optical cavity by use of spatial mode interference*, Optics Letters **24**, (1999). 18
- [56] E. D. Black, *An introduction to Pound–Drever–Hall laser frequency stabilization*, American Journal of Physics **69**, 79 (2001). 18, 59

## BIBLIOGRAPHY

---

- [57] R. W. P. Drever, J. L. Hall, F. V. Kowalski, J. Hough, G. M. Ford, A. J. Munley and H. Ward, *Laser phase and frequency stabilization using an optical resonator*, Applied Physics B **31**, 97 (1983). 18
- [58] S. Kaufer, Optical-AC-Coupling mit einem linearen, schmalbandigen Resonator, Masterthesis, 2013. 19, 47, 50, 51
- [59] P. Kwee, Charakterisierung von Lasersystemen für Gravitationsswellendetektoren, Diploma thesis, 2005. 19
- [60] D. Z. Anderson, *Alignment of resonant optical cavities*, Applied Optics **23**, 2944 (1984). 20
- [61] J. C. Alex Abramovici, *Feedback Control Systems* (Springer Us, 2012). 21
- [62] S. Kaufer, M. Kasprzack, V. Frolov and B. Willke, *Demonstration of the optical AC coupling technique at the advanced LIGO gravitational wave detector*, Classical and Quantum Gravity **34**, 145001 (2017). 28, 84, 85, 88, 89
- [63] P. Kwee, Optical AC Coupling Part I: theory, Technical report available at AEI, 2007, technical report available at AEI. 30
- [64] P. Kwee, Optical AC Coupling Part II: Noise Couplings, Technical report available at AEI, 2008, technical report available at AEI. 30, 39
- [65] G. Heinzel, K. A. Strain, J. Mizuno, K. D. Skeldon, B. Willke, W. Winkler, R. Schilling, A. Rüdiger and K. Danzmann, *Experimental Demonstration of a Suspended Dual Recycling Interferometer for Gravitational Wave Detection*, Phys. Rev. Lett. **81**, 5493 (1998). 39, 95
- [66] T. Klaassen, J. de Jong, M. van Exter and J. P. Woerdman, *Transverse mode coupling in an optical resonator*, Optics Letters **30**, 1959 (2005). 44
- [67] P. Belland and J. P. Crenn, *Changes in the characteristics of a Gaussian beam weakly diffracted by a circular aperture*, Applied Optics **21**, 522 (1982). 53
- [68] H.Kogelnik, *Laser Beams and Resonators*, Proceedings of the IEEE **54**, (1966). 53

- [69] V. Leonhardt, *Displacement measurements on suspended mirrors for off-resonant thermal noise detection*, PhD Thesis, Universität at Hannover, 2003. 54
- [70] D. Sigg and P. Schwinberg, Third Generation Table-Top Frequency Stabilization Servo, LIGO DCC. 59
- [71] B. Willke, K. Danzmann, M. Frede, P. King, D. Kracht, P. Kwee, O. Puncken, R. L. S. (Jr), B. Schulz, F. Seifert, C. Veltkamp, S. Wagner, P. Wessels and L. Winkelmann, *Stabilized lasers for advanced gravitational wave detectors*, Classical and Quantum Gravity **25**, 114040 (2008). 59
- [72] S. Goßler, A. Bertolini, M. Born, Y. Chen, K. Dahl, D. Gering, C. Gräf, G. Heinzl, S. Hild, F. Kawazoe, O. Kranz, G. Kühn, H. Lück, K. Mossavi, R. Schnabel, K. Somiya, K. A. Strain, J. R. Taylor, A. Wanner, T. Westphal, B. Willke and K. Danzmann, *The AEI 10 m prototype interferometer*, Classical and Quantum Gravity **27**, 084023 (2010). 59
- [73] T. Westphal, G. Bergmann, A. Bertolini, M. Born, Y. Chen, A. V. Cumming, L. Cunningham, K. Dahl, C. Gräf, G. Hammond, G. Heinzl, S. Hild, S. Huttner, R. Jones, F. Kawazoe, S. Köhlenbeck, G. Kühn, H. Lück, K. Mossavi, J. H. Pödl, K. Somiya, A. M. van Veggel, A. Wanner, B. Willke, K. A. Strain, S. Goßler and K. Danzmann, *Design of the 10 m AEI prototype facility for interferometry studies*, Applied Physics B **106**, 551 (2012). 59
- [74] R.W.P.Drever, J.L.Hall, F.V.Kowalski, J.Hough, G.M.Ford, A.J.Munley and H.Ward, *Laser Phase and Frequency Stabilization Using an Optical Resonator*, Applied Physics B **31**, 97 (1983). 59
- [75] R. Mancini, *Op Amps for Everyone* (Newnes/Elsevier, 2003). 59
- [76] D. Wilken, *Laser Power Stabilization Beyond the Shot Noise Limit Using Nonclassical Light*, Diploma thesis, Leibniz Universität Hannover, 2017. 60
- [77] E. A. Whittaker, M. Gehrtz and G. C. Bjorklund, *Residual amplitude modulation in laser electro-optic phase modulation*, J. Opt. Soc. Am. B **2**, 1320 (1985). 62

## BIBLIOGRAPHY

---

- [78] L. Li, F. Liu, C. Wang and L. Chen, *Measurement and control of residual amplitude modulation in optical phase modulation*, Review of Scientific Instruments **83**, 043111 (2012). 62
- [79] J. Sathian and E. Jaatinen, *Intensity dependent residual amplitude modulation in electro-optic phase modulators*, Appl. Opt. **51**, 3684 (2012). 62
- [80] T. Isogai, J. Miller, P. Kwee, L. Barsotti and M. Evans, *Loss in long-storage-time optical cavities*, Opt. Express **21**, 30114 (2013). 64
- [81] B. Brandstätter, A. McClung, K. Schüppert, B. Casabone, K. Friebe, A. Stute, P. O. Schmidt, C. Deutsch, J. Reichel, R. Blatt and T. E. Northup, *Integrated fiber-mirror ion trap for strong ion-cavity coupling*, Review of Scientific Instruments **84**, 123104 (2013). 68
- [82] J. L. Hall, J. Ye and L.-S. Ma, *Measurement of mirror birefringence at the sub-ppm level: Proposed application to a test of QED*, Phys. Rev. A **62**, 013815 (2000). 68
- [83] D. H. Foster, A. K. Cook and J. U. Nöckel, *Degenerate perturbation theory describing the mixing of orbital angular momentum modes in Fabry-Perot cavity resonators*, Phys. Rev. A **79**, 011803 (2009). 68
- [84] M. Zeppenfeld and P. Pinkse, *Calculating the fine structure of a Fabry-Perot resonator using spheroidal wave functions*, Opt. Express **18**, 9580 (2010).
- [85] C. Bond, P. Fulda, L. Carbone, K. Kokeyama and A. Freise, *The effect of mirror surface distortions on higher order Laguerre-Gauss modes*, Journal of Physics: Conference Series **363**, 012005 (2012).
- [86] B. Sorazu, P. J. Fulda, B. W. Barr, A. S. Bell, C. Bond, L. Carbone, A. Freise, S. Hild, S. H. Huttner, J. Macarthur and K. A. Strain, *Experimental test of higher-order Laguerre-Gauss modes in the 10 m Glasgow prototype interferometer*, Classical and Quantum Gravity **30**, 035004 (2013).
- [87] A. Noack, C. Bogan and B. Willke, *Higher-order Laguerre Gauss modes in (non-) planar four-mirror cavities for future gravitational wave detectors*, Opt. Lett. **42**, 751 (2017). 68



- [88] P. K. Yu and K. M. Luk, *High-order azimuthal modes in the open resonator*, Electronics Letters **19**, 539 (1983). 68
- [89] K.-M. Luk and P.-K. Yu, *Generation of Hermite–Gaussian beam modes by multipoles with complex source points*, J. Opt. Soc. Am. A **2**, 1818 (1985). 68
- [90] M. Uphoff, M. Brekenfeld, G. Rempe and S. Ritter, *Frequency splitting of polarization eigenmodes in microscopic Fabry–Perot cavities*, New Journal of Physics **17**, 013053 (2015). 68
- [91] B. Abbott, the LIGO Scientific Collaboration and the Virgo Collaboration, *GW170814: A Three-Detector Observation of Gravitational Waves from a Binary Black Hole Coalescence*, Physical Review Letters **119**, (2017). 83
- [92] B. Abbott, the LIGO Scientific Collaboration and the Virgo Collaboration, *GW170104: Observation of a 50-Solar-Mass Binary Black Hole Coalescence at Redshift 0.2*, Physical Review Letters **118**, (2017). 83
- [93] B. Abbott, the LIGO Scientific Collaboration and the Virgo Collaboration, *GW170817: Observation of Gravitational Waves from a Binary Neutron Star Inspiral*, Physical Review Letters **119**, (2017). 83
- [94] B. Abbott, the LIGO Scientific Collaboration and the Virgo Collaboration, *Gravitational Waves and Gamma-Rays from a Binary Neutron Star Merger: GW170817 and GRB 170817A*, The Astrophysical Journal **848**, L13 (2017). 83
- [95] L. S. Collaboration, Instrument Science White Paper, LIGO DCC, 2015. 83
- [96] M. Evans, Technical report, LIGO Document T070260-v1 (unpublished). 83, 90
- [97] P. Kwee, J. Miller, T. Isogai, L. Barsotti and M. Evans, *Decoherence and degradation of squeezed states in quantum filter cavities*, Phys. Rev. D **90**, 062006 (2014). 83
- [98] The ET science team, 2011. 83

## BIBLIOGRAPHY

---

- [99] R. W. P. Drever, J. Hought, A. J. Munley, S.-A. Lee, R. Spero, S. E. Whitcomb, H. Ward, G. M. Ford, M. Hereld, N. A. Robertson, I. Kerr, J. R. Pugh, G. P. Newton, B. Meers, E. D. Brooks and Y. Gursel, in *Quantum Optics, Experimental Gravity, and Measurement Theory*, edited by P. Meystre and M. O. Scully (Springer US, Boston, MA, 1983), pp. 503–514. 84
- [100] D. Schnier, J. Mizuno, G. Heinzel, H. Lück, A. Rüdiger, R. Schilling, M. Schrepel, W. Winkler and K. Danzmann, *Power recycling in the Garching 30 m prototype interferometer for gravitational-wave detection*, *Physics Letters A* **225**, 210 (1997).
- [101] B. J. Meers, *Recycling in laser-interferometric gravitational-wave detectors*, *Physical Review D* **38**, 2317 (1988). 84
- [102] S. Hild, *Beyond the second generation of laser-interferometric gravitational wave observatories*, *Classical and Quantum Gravity* **29**, 124006 (2012). 84
- [103] L. Winkelmann, O. Puncken, R. Kluzik, C. Veltkamp, P. Kwee, J. Poeld, C. Bogan, B. Willke, M. Frede, J. Neumann, P. Wessels and D. Kracht, *Injection-locked single-frequency laser with an output power of 220 W*, *Applied Physics B* **102**, 529 (2011). 84
- [104] L. Winkelmann, *Injection-locked high power oscillator for Advanced gravitational wave observatories*, PhD Thesis, Leibniz Universitaet Hannover, 2012.
- [105] O. Puncken, *Pumpkopfdesign für den Advanced LIGO Laser*, PhD Thesis, Leibniz Universitaet Hannover, 2011. 84
- [106] J. Poeld, *Design, Implementation and Characterization of the Advanced LIGO 200W System*, PhD Thesis, Gottfried Wilhelm Leibniz Universität Hannover, 2014. 84
- [107] C. L. Mueller, M. A. Arain, G. Ciani, R. T. DeRosa, A. Effler, D. Feldbaum, V. V. Frolov, P. Fulda, J. Gleason, M. Heintze, K. Kawabe, E. J. King, K. Kokeyama, W. Z. Korth, R. M. Martin, A. Mullavey, J. Peold, V. Quetschke, D. H. Reitze, D. B. Tanner, C. Vorvick, L. F. Williams and G. Mueller, *The advanced LIGO input optics*, *Review of Scientific Instruments* **87**, 014502 (2016). 85

- [108] A. L. Team, Technical report, (unpublished), <https://dcc.ligo.org/LIGO-M060056-x0/public>. 85
- [109] J. R. Peter Fritschel, List of ISC Photodetectors in Advanced LIGO, DCC T1000264-v7, 2014. 86
- [110] D. Martynov, *Lock Acquisition and Sensitivity Analysis of Advanced LIGO Interferometers*, PhD Thesis, California Institute of Technology, 2015, dCC: P1500087-v1. 90
- [111] C. Affeldt, *Laser power increase for GEO 600 Commissioning aspects towards an operation of GEO 600 at high laser power*, PhD Thesis, QUEST-Leibniz-Forschungsschule der Gottfried Wilhelm Leibniz Universität Hannover, 2014. 92, 94, 99
- [112] A. Freise, *The next Generation of Interferometry: Multi-Frequency Optical Modelling, Control Concepts and Implementation*, PhD Thesis, Max-Planck-Institut für Gravitationsphysik, 2003. 94
- [113] G. Heinzl, A. Freise, H. Grote, K. Strain and K. Danzmann, *Dual recycling for GEO 600*, Classical and Quantum Gravity **19**, 1547 (2002). 94
- [114] H. Lueck, A. Freise, S. Goßler, S. Hild, K. Kawabe and K. Danzmann, *Thermal correction of the radii of curvature of mirrors for GEO 600*, Classical and Quantum Gravity **21**, S985 (2004). 94
- [115] H. Wittel, H. Lueck, C. Affeldt, K. L. Dooley, H. Grote, J. R. Leong, M. Prijatelj, E. Schreiber, J. Slutsky, K. Strain, M. Was, B. Willke and K. Danzmann, *Thermal correction of astigmatism in the gravitational wave observatory GEO 600*, Classical and Quantum Gravity **31**, 065008 (2014).
- [116] H. Wittel, *Active and passive reduction of high order modes in the gravitational wave detector GEO600*, PhD Thesis, Quest-Leibniz-Forschungsschule der Gottfried Wilhelm Leibniz Universität Hannover, 2015. 94, 98
- [117] H. Grote, *Making it Work: Second Generation Interferometry in GEO600!*, PhD Thesis, Leibniz Universität Hannover, 2003. 95

## BIBLIOGRAPHY

---

- [118] L. Schnupp, contribution to the European Collaboration Meeting on Interferometric Detection of Gravitational Waves in Sorrento (unpublished). 95
- [119] M. B. Gray, A. J. Stevenson, H.-A. Bachor and D. E. McClelland, *Broadband and tuned signal recycling with a simple Michelson interferometer*, *Appl. Opt.* **37**, 5886 (1998). 95
- [120] J. Degallaix, H. Grote, M. Prijatelj, M. Hewitson, S. Hild, C. Affeldt, A. Freise, J. Leong, H. Lück, K. A. Strain, H. Wittel, B. Willke and K. Danzmann, *Commissioning of the tuned DC readout at GEO 600*, *Journal of Physics: Conference Series* **228**, 012013 (2010). 99
- [121] S. Hild, H. Grote, J. Degallaix, S. Chelkowski, K. Danzmann, A. Freise, M. Hewitson, J. Hough, H. Lück, M. Prijatelj, K. A. Strain, J. R. Smith and B. Willke, *DC-readout of a signal-recycled gravitational wave detector*, *Classical and Quantum Gravity* **26**, 055012 (2009). 99
- [122] *Datasheet Keysight Technologies 35670A Dynamic Signal Analyzer*. 102
- [123] J. Lough, Poster at LVC meeting 2015, <https://dcc.ligo.org/LIGO-G1500301>, Presentation. 107

# Acknowledgements

The decision to become a doctoral student at the AEI led to many things that I am grateful for. Most probably the best thing about it are the new people I met and that made this time unforgettable.

I would like to thank Prof. Dr. Karsten Danzmann for bringing my attention to the field of gravitational physics: Without him and his enthusiastic lectures, I may not have gotten into this exciting field exactly at the right time. It was a pleasure to work in the scientific environment that you have created.

My advisor apl. Prof. Dr. Benno Willke, I want to thank you for leading me through the last years. You were always available if advice was needed, encouraged me to never give up in difficult times and reliably helped me in focusing my thoughts and make the right decisions.

I want to thank all the colleagues from the laser group, Christina, Dennis S., Dennis W., Fabian, Kanioar, Li-Wei, Jan and Robin for the good atmosphere, Harz trips, coffee breaks and interesting discussion within the last years. Marina and Nina I would like to thank you for assisting me in setting up of the experiment within the vacuum tank. Special thanks for constant support in the laboratory and the never ending cookie supply go to Patrick.

Without the help of Christoph and James, working at GEO 600 would not have been possible, thank you for your support.

The 12 o'clock mensa group changed so much within the last years, Thomas, Katharina, Germán, Oliver, Daniel, Victor, Lea, Julie, Joscha, Jasper, Heather, Stefan, Melanie, Lisa, Amrit, Vaishali, Ramon and Axel, you all contributed in making even the mensa food enjoyable. I also want to thank the AEI soccer team, I will miss this event a lot.

For proof-reading I want to thank Evan, Christoph, Colin, Daniel, Holger, Ramon and Tobin and especially Heather, Henning and Oliver. Of course, all the remaining errors are entirely my fault.

I want to thank my brother Henning for his constant encouragement and support. I could not wish for a better brother than you and I am glad to have you in my life.

I am also blessed with wonderful parents that have been supporting me throughout my whole life, in good and in bad times. It is very precious to have someone you can always rely on.

Franzi, thank you for your love, your encouragement and your patience. It was also because of you that I arrived where I am today.



# Curriculum vitae

Steffen Kaufer  
Perlstr. 7  
30161 Hannover  
Steffen.Kaufer@gmx.de

Born on July 25th, 1986 in Lehrte, Niedersachsen

---

## University studies

- |                  |  |
|------------------|--|
| 3/2013 - present | Doctoral studies<br>Leibniz Universität Hannover   |
| 1/2012 - 3/2013  | Master thesis, <i>Optical-AC-Coupling mit einem linearen, schmalbandigen Resonator</i>             |
| 3/2010 - 9/2010  | Bachelor thesis, <i>Untersuchung von Gold-Aluminiumoxid-Proben und Phthalocyaninen auf Ag(100)</i> |
| 10/2007 - 3/2013 | Physics studies,<br>Leibniz Universität Hannover   |

---

## Civilian service

- |                 |                          |
|-----------------|--------------------------|
| 7/2006 - 4/2007 | Diakoniestation Burgdorf |
|-----------------|--------------------------|

---

## Education

- |                 |                                    |
|-----------------|------------------------------------|
| 8/1999 - 7/2006 | Gymnasium Lehrte, Abschluss Abitur |
| 8/1997 - 7/1999 | Orientierungsstufe Lehrte-Süd      |
| 8/1993 - 7/1997 | Grundschule Ahlten                 |